Stockholm
University

Inference on Dark Matter in Effective Field Theories

From XENON1T towards XENONnT: Chiral effective field theory analysis of nuclear recoils, single electrons and uncommon background modelling

Vasile Cristian Antochi

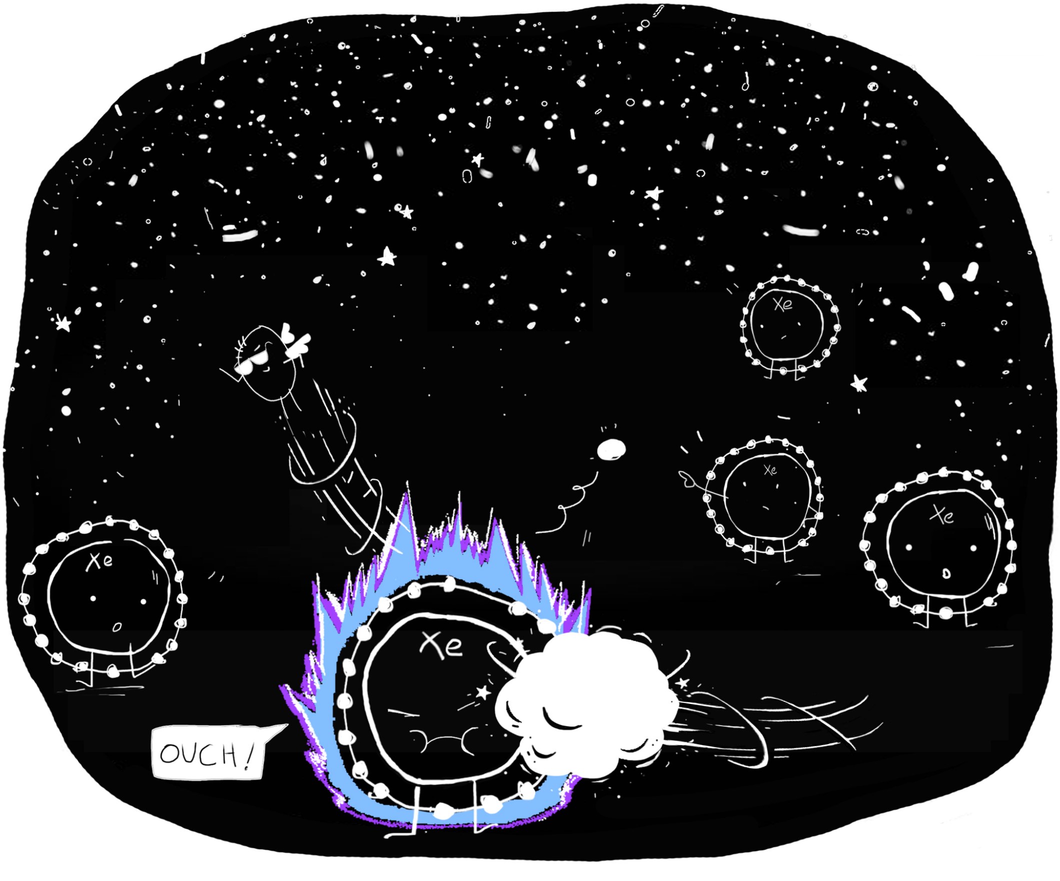

Doctoral Thesis in Physics at Stockholm University, Sweden 2022

Inference on Dark Matter in Effective Field Theories

From XENON1T towards XENONnT: Chiral effective field theory analysis of nuclear recoils, single electrons and uncommon background modelling

Vasile Cristian Antochi

Academic dissertation for the Degree of Doctor of Philosophy in Physics at Stockholm University to be publicly defended on Tuesday 31 May 2022 at 14.00 in sal FB42 AlbaNova universitetscentrum, Roslagstullsbacken 21, and online via Zoom, public link is available at the department website.

Abstract

Cosmological and astronomical observations show that most of the matter in the Universe is dark. This dissertation provides an overview of the dark matter evidence, and focuses on the particle dark matter hypothesis, describing possible particle candidates, concentrating on the Weakly Interactive Massive Particles (WIMPs). It describes the main WIMP detection strategies and addresses the subject of WIMP scattering in direct detection experiments. This work analyses the data from the XENON1T experiment, investigating within a Chiral Effective Field Theory (ChEFT) framework the nuclear recoils from possible WIMP interactions. It presents the XENON1T detector, the main backgrounds, the xenon signal emission model and the background studies, and describes the statistical inference adopted in the analysis.

The XENON1T detector was a dual-phase Time Projection Chamber (TPC) using a ~2 tonne liquid xenon target to detect scattering particles. WIMPs with masses above ~10GeV/c^2 scattering against the xenon nuclei would deposit enough energy to create an observable event.

The ChEFT analysis is performed on the XENON1T data from 278.8 days of operation for a total exposure of 1 tonne×year, with a combined likelihood of two science runs. The region of interest for this analysis was extended from [4.9, 40.9] keV$_{nr}$, in the Spin Independent analysis, to [4.9, 54.4] keV$_{nr}$, to increase the acceptance of possible models with rates peaking at higher energies (>0keV$_{nr}$). The analysis shows that the data is consistent with a background only hypothesis and provides constraints on the interaction coefficients and the physics scale for 25 different operators. The analysis is complemented by limits on three benchmark models of interaction using ChEFT. For these models we investigate the effect of isospin breaking interactions, reporting cancellation regions where the limit worsens up to 6 orders of magnitude with respect to the isospin conserving case.

The dissertation is complemented with the dark matter-electron scattering study within an EFT framework, analysing the single or few electron emission signals in XENON1T. The analysis provides the first experimental limits on the dark matter-electron effective operators for the magnetic and electric dipole, and anapole interactions.

Lastly, the dissertation describes an example of introducing a data-driven background model in an inference framework based on explicit multidimensional likelihood computation. The background modelling is done using calibration data from the XENONnT detector, the next iteration of a dual-phase xenon TPC in the XENON detector family, which is currently in operation.

Keywords: *Dark Matter, Direct Detection, Effective Field Theory, Chiral Effective Field Theory.*

Stockholm 2022
http://urn.kb.se/resolve?urn=urn:nbn:se:su:diva-203809

ISBN 978-91-7911-864-8
ISBN 978-91-7911-865-5

Stockholm University

Department of Physics

Stockholm University, 106 91 Stockholm

INFERENCE ON DARK MATTER IN EFFECTIVE FIELD THEORIES

Vasile Cristian Antochi

Stockholm
University

Inference on Dark Matter in Effective Field Theories

From XENON1T towards XENONnT: Chiral effective field theory analysis of nuclear recoils, single electrons and uncommon background modelling

Vasile Cristian Antochi

ISBN print 978-91-7911-864-8
ISBN PDF 978-91-7911-865-5

Printed in Sweden by Universitetsservice US-AB, Stockholm 2022
Front cover: Illustration by Yiqi Lin
Distributor: Department of Physics, Stockholm University

It all started with ABC...

List of Papers

The following papers, referred to in the text by their Roman numerals, are included in this thesis.

PAPER I: **Effective Field Theory and Inelastic Dark Matter Results from XENON1T**
Aprile E., et al. (XENON Collaboration), *In internal review*,
DOI: Manuscript

PAPER II: **Emission of Single and Few Electrons in XENON1T and Limits on Light Dark Matter**
Aprile E., et al. (XENON Collaboration), *arXiv preprint*, **2112**, 12116 (2021), *Submitted*.
DOI: https://doi.org/10.48550/arXiv.2112.12116

PAPER III: **Finding dark matter faster with explicit profile likelihoods**
Aalbers J., Pelssers B., Antochi V.C., Tan P.L., Conrad J., *Phys. Rev. D*, **102**, 072010 (2020).
DOI: https://doi.org/10.1103/PhysRevD.102.072010

Reprints were made with permission from the publishers.

Author's contribution

- Paper I: I have thoroughly researched the topic, produced the recoil rate spectra using tools obtained after lengthy discussions with effective field theory (EFT) experts and theorists, I have used the instruments of the XENON collaboration to obtain the signal templates in the XENON analysis coordinates (cS1-cS2) including the detector characteristics, I have studied and modified the inference framework Blueice, used in the XENON collaboration to include the new signal models, and I performed a full study towards the validation of the inference and produced the final results for the EFT analysis. Large part of the paper was written by me.

- Paper II: I have proposed the addition to the paper of the Light Dark Matter-electron EFT interactions, and I computed the rate spectra of single or few electrons emission for the relevant xenon orbitals for the EFT channels considered, that went into the signal model production. I contributed to the editing of Paper II.

- Paper III: I have been involved in the development and testing of the software described in Paper III. I have tested the performance of the software and contributed to the writing of portions of the paper. Further more I developed the first ER and NR models describing the XENON1T emission model in the software, I have developed a first effective surface background model for XENON1T sources, and worked towards developing a XENONnT surface background model using the FLAMEDISX software, as described in the dissertation.

Consistent parts of Chapter 1, Chapter 2 and Chapter 3 were adapted from the Licentiate thesis.

Contributions not included

- **Improved quality tests of R11410-21 photomultiplier tubes for the XENONnT experiment**
  Antochi V.C., et al. *JINST*, **16**, 08, P08033 (2021).
  DOI: https://doi.org/10.1088/1748-0221/16/08/P08033

The main contributions to this paper were the work towards the PMT testing procedure, improvements in the raw waveform processing, single electron gain measurements, and after-pulse studies.

Contents

Abbreviations

ΛCDM	Λ-Cold-Dark-Matter
AA	Axial-vector$\otimes$Axial-vector
AC	Accidental Coincidence
AKDE	Adaptive Kernel Density Estimation
ALP	Axion-like Particle
AV	Axial-vector$\otimes$Vector
BBF	Bayesian Band fitting Framework
BSM	Beyond Standard Model
CDF	Cumulative Density Function
CEνNS	Coherently Enhanced neutrino-Nucleus Scattering
ChEFT	Chiral Effective Field Theory
CL	Confidence Level
CMB	Cosmic Microwave Background
CP	Charge-Parity
cS1	Corrected S1 signal (see S1)
cS2	Corrected S2 signal (see S2)
DAQ	Data Aquisition
DM	Dark Matter
DPE	Double Photo-Electron Emission
EFT	Effective Field Theory
ER	Electronic Recoil
FLAMEDISX	Fast Likelihood Analysis in MorE DImensionS for Xenon TPCs
GOF	Goodness of Fit

GPU	Graphical Processing Unit
KDE	Kernel Density Estimation
LDM	Light Dark Matter
LNGS	Laboratori Nazionali del Gran Sasso
LXe	Liquid xenon
MC	Monte Carlo
MSSN	Minimal Supersymmetric Standard Model
NEST	Noble Element Simulation Technique
NR	Nuclear Recoil
NREFT	Non-Relativistic Effective Field Theory
PCL	Power-constrained Limit
PDF	Probability Density Function
PE	Photo-Electron
PMT	Photo-multiplier Tube
PS	Pseudo-scalar⊗Scalar
PTFE	Polytetrafluoroethylene
QCD	Quantum Chromodynamics
ROI	Region of Interest
S1	Prompt scintillation signal in a dual-phase TPC
S2	Delayed charge signal in a dual-phase TPC
SD	Spin Dependent
SHM	Standard Halo Model
SI	Spin Independent
SM	Standard Model
SR0	Science Run 0
SR1	Science Run 1
SS	Scalar⊗Scalar
TPC	Time Projection Chamber
TT	Tensor⊗Tensor
VV	Vector⊗Vector
WIMP	Weakly Interacting Massive Particle

List of Figures

List of Tables

1. Dark Matter

Since the astronomical observations in galaxy dynamics of Fritz Zwicky in the early 1930s [1] the Dark Matter question has continuously puzzled physicists. Ever since, physicists have gathered more and more evidence that some manifestation of matter that does not emit any light nor seems to interact with baryonic matter but exerts gravitational force on the structures in the universe exists. This chapter aims to summarize evidence of dark matter coming from astrophysical and cosmological observations as well as provide some theoretical background of possible particle candidates for dark matter.

1.1 Dark Matter evidence

The first evidence of dark matter comes from the galaxy dynamics in the Coma cluster, where galaxies were observed orbiting each other with much higher velocity than expected from the gravitational potential of the luminous matter in the cluster. However one of the main evidence that most of the matter in the universe is dark comes from cosmological evidence. According to the latest studies of the Cosmic Microwave Background (CMB) of all the matter in our universe 16% is accounted for and well described by the Standard Model (SM) of particle physics while the remaining 84% of the matter density is still a mystery [2].

The most striking observation of dark matter presence comes though from the gravitational lensing analysis of the galaxy cluster merger 1E 0657–57, also known as the Bullet cluster. This cluster merger, shown in Figure 1.1, is an example of dynamical separation of dark matter and baryonic matter. By observing the distribution and the distortion of the galaxies around the merger from an optical image, it is possible to infer the mass distribution in the cluster through gravitational lensing. All matter contribute to the lensing effect, however the dark matter contribution will dominate. Observing the same object in X-ray however will show the distribution of most of the baryonic mater, present in the form of hot ionised gas. In the case of merger 1E 0657–57 it is possible to observe an almost complete separation of the dark matter mass distribution profiles of the subclusters, that proceeded through each other undisturbed, and the observation in X-ray of the baryonic matter, which interacted and was

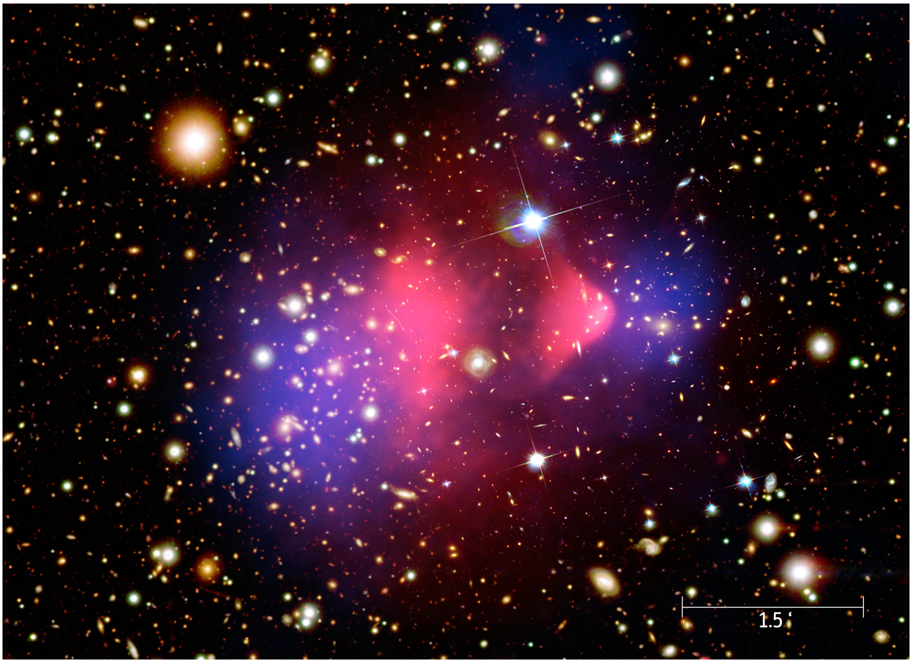

Figure 1.1: Composite image of the cluster 1E 0657–57 from optical and x-ray observation. The mass distribution profile is coloured in blue as observed through gravitational lensing, while the x-ray plasma emission of excited gas (ordinary matter) is shown in pink. Image credit: X-ray: NASA/CXC/CfA/M.Markevitch et al.; Optical: NASA/STScI; Magellan/U.Arizona/D.Clowe et al.; Lensing Map: NASA/STScI; ESO WFI; Magellan/U.Arizona/D.Clowe et al.

slowed down in the collision [3, 4]. In the absence of dark matter the mass profile and the X-ray image of the hot plasma cloud should have coincided, but since this is not the case, and given the big mass-to-light ratio in the sub-clusters, this suggests that the mass in this object is dominated by collisionless dark matter.

Another very important indication of the presence of dark matter surrounding galaxies comes from the astronomical observation of rotation curves of stars and gas clouds. By measuring the rotation curve of the peripheral galactic objects through Doppler shift it is possible to trace the rotation velocity curves as a function of the distance from the galactic centre.

In the case of a disk galaxy objects at a distance greater than the disk radius, should have a velocity that scales as $v(R) \propto \frac{1}{\sqrt{R}}$ in the hypothesis that all the mass is contained in the galactic disk and central bulge. However astronomical measurements of the rotation curves do not match this falling velocity trend, but they seem to remain roughly constant to large to very large radii suggesting

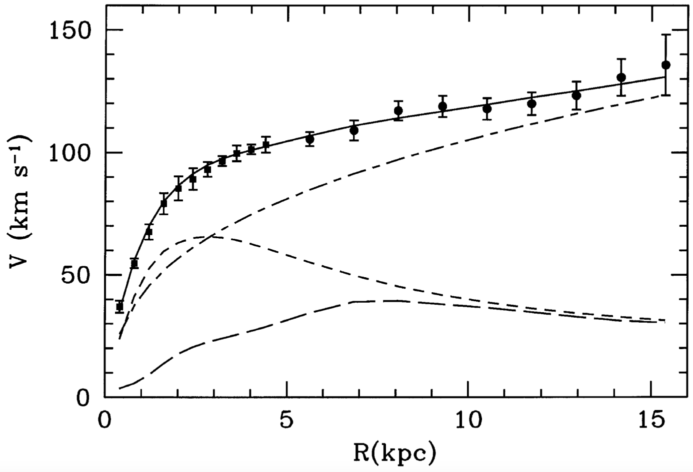

Figure 1.2: Fit of the rotation curve of M33 as reported in [5]. The short dashed line is the contribution of the galactic bulge and disk, the long dashed line is the contribution of gas clouds and the long-and-short dashed line is the dark matter component.

a mass distribution that extends much further than the galactic disk, surrounding the entire galaxy [5]. Figure 1.2 shows the measurements of the rotation velocity of galactic objects in the M33 galaxy and the contribution to the velocity from the observed mass. In this model the measured contribution from the galactic gas and galactic disk have a falling trend for high distances that do not match the data: in order for it to fit the data a third, dark component, is needed in a form of a dark matter halo around the galaxy extending to farther distances than the galactic disc.

While for the dynamical properties of the Bullet Cluster and for the rotation curves there might exist explanations that do not require the presence of Dark Matter [6, 7], one thing that cannot possibly be explained without it is the structure formation in the Universe. Originally the Universe was extremely uniform, with temperature fluctuations of the order of 1 in 100000 [8] as measured from the CMB, however, as it expanded, big structures began to form. N-body simulations have shown that for such structures to form, particle dark matter is necessary [9, 10].

1.2 Dark Matter distribution

From the observations, it is possible to model the dark matter distribution in our galaxy by assuming that the dark matter halo consists in a pressureless gas

Parameter	Value at $r = R_0$
ρ_0	0.3 GeVcm^{-3}
v_c	220 kms^{-1}
v_{esc}	544 kms^{-1}

Table 1.1: Parameters of the Standard Halo Model at $r = R_0 \simeq$ 8kpc, which is the distance of the Solar System from the centre of the Milky Way. ρ_0 is the local dark matter density, v_c is the Solar System's orbital velocity and v_{esc} the particle escape velocity. Table adapted from [12].

of particles that interact only gravitationally. Other valid assumptions are that the halo is isotropic, virialized and in hydrostatic equilibrium with a density profile $\rho(r) \propto r^{-2}$, where r is the distance from the centre of the galaxy. In this model, called Standard Halo Model (SHM), the velocity distribution would follow a Maxwell distribution [11]

$$f(v) = \frac{N}{2\pi\sigma_v^2} \exp\left(-\frac{v^2}{2\sigma_v^2}\right) \tag{1.1}$$

where N is a normalisation constant and the σ_v parameter is the velocity dispersion which is related to the orbital circular velocity of the Solar System in the galaxy as $\sigma_v = v_c/\sqrt{2}$. This distribution however has to be truncated at the galactic escape velocity v_{esc} since particles with higher velocities would not be gravitationally bound to the system and would break free from the dark matter halo.

In Table 1.1 are reported the parameters of the SHM of our galaxy commonly used in the dark matter direct detection community and used in the scope of this dissertation.

The SHM provides a good hypothesis for the distribution of dark matter in the galaxy, however it relies heavily on the assumption that the halo is isotropic and in thermal equilibrium. Numerical simulations of dark matter halos have shown that secondary components that do not follow these assumptions can be present [13] and could influence the current dark matter limits. Higher dark matter density would mean tighter constraints on the interaction strength and the cross section, while different velocity distributions would have a strong effect on the detection threshold.

1.3 Candidates for dark matter

Most of the evidence for dark matter seems to point towards a particle nature of it. There are however theories of modified gravity that could describe some of the properties observed [14], as the mentioned example of the rotation curves, they fail however to describe dynamical properties such as the Bullet Cluster, or the structure formation in the universe.

If the particle nature of dark matter is assumed, the hypothetical particle (or particles) cannot be fully explained by candidates within the standard model (SM) and a detection of dark matter would be evidence for beyond standard model (BSM) physics.

Categories of dark matter candidates can be defined by dividing them by their assumed mass and velocity. Very light particles, akin to neutrinos, would likely be relativistic at the cosmological time of decoupling from baryonic matter, if they are assumed to be created during the early time of the Universe, and would remain relativistic (or *hot*) until late times. Heavier particles would decouple much earlier and be much slower (*cold*). From numerical simulations of large scale structure formation in the universe, cold dark matte is preferred over its hot counterpart [15]. While hot dark matter cannot fully explain the dark matter problem, it could account for a fraction of it [16].

The current cosmological paradigm is the Λ-Cold-Dark-Matter (Λ-CDM), which describes the composition of the Universe through the cosmological constant Λ, associated with dark energy, a cold dark matter component and the baryonic matter component [2].

Many particle candidates for dark matter have been proposed and investigated [17], however for a particle to fit the Λ-CDM paradigm it should have some specific properties: they should be *cold* ($v \ll c$), stable and neutral and have a production mechanism that would lead to the dark matter density observable today. Relatively short lived or charged dark matter would either produce detectable signals through electromagnetic interactions or would decay away without a complex continuous replenishment mechanism.

A first possible candidate for particle dark matter that could in principle solve the dark matter conundrum could be the sterile neutrino [18], a massive right-handed neutrino which does not interact with standard model particles through the electroweak force. The existence of such a particle could explain also the neutrino oscillations [19]. One of the problems with most of the sterile neutrino models is that they would be too *warm* to fit in the Λ-CDM paradigm and might not account for all the observable dark matter density.

Another valid candidate for dark matter is the axion. The axion is a low mass particle first proposed to solve the strong-CP problem in quantum chromodynamics (QCD) [20, 21] and later was considered as a possible cold dark matter candidate as well [22].

Axions and axion-like particles (ALP), given their low mass, in order to make up the dark matter bulk observable today, would need to have a non thermal production mechanism in the early universe. Thermal production can also be possible but in order for thermally produced axions to account for the dark matter density they would need to have a too large mass ($\sim$ 8eV) that would result into a lifetime shorter than the age of the Universe [23]. There are many production mechanisms proposed that could give rise to axions in different mass ranges and with very small velocity dispersion, making them good cold dark matter candidates.

1.4 Weakly Interacting Massive Particles

One of the most intriguing possible candidates for dark matter is the class of particles known as Weakly Interacting Massive Particles (WIMPs). As the name suggests, WIMPs are a proposed class of non baryonic particles with masses of the order of $\gtrsim$ 10 GeV/c^2 that could interact with standard model particles through the (electro-) weak force and would satisfy all the criteria for the ΛCDM paradigm [23]. The most striking feature of these kind of particles is that if WIMPs and standard model particles were in thermal equilibrium before nucleosynthesis started in the early Universe, they would correctly account for the present dark matter density if the WIMP annihilation cross section is of the order of the weak scale. This is commonly regarded as the *WIMP miracle*.

In the early Universe, assuming thermal equilibrium between WIMPs and standard model particles, WIMP production would occur through SM pair particle annihilation and SM particles would be produced by WIMP annihilation in equilibrium with an interaction rate of

$$\Gamma = n_\chi^{eq} \langle \sigma v \rangle \tag{1.2}$$

with n_χ^{eq} the number density of WIMPs in thermal equilibrium, at this time $n_\chi^{eq} \propto T^3$ with the temperature $T \gg m_\chi$, and $\langle \sigma v \rangle$ being the thermally averaged annihilation cross section times the particle velocity v.

As the Universe expanded, the temperature T dropped below the WIMP mass m_χ and thermal equilibrium could not be maintained. At this point the number density of WIMPs drops according to the Boltzmann equation for time evolution of the number density

$$\frac{\mathrm{d}n_\chi}{\mathrm{d}t} + 3Hn_\chi = -\langle \sigma v \rangle [n_\chi^2 - (n_\chi^{eq})^2] \tag{1.3}$$

where H is the Hubble constant. Eq. 1.3 results in a number density exponentially suppressed $n_\chi \propto e^{-m_\chi/T}$ and the annihilation rate drops proportionally to n_χ. When the annihilation rate reaches $\Gamma < H$, which means that the expansion rate of the Universe is faster than the annihilation rate, the process stops, causing the density of WIMPs to *freeze out*, as a *thermal relic*.

The dependence of Eq. 1.3 on the cross section leads to an inverse relation between the cosmological density Ω_χ and the cross section itself of $\Omega_\chi h^2 \propto \frac{1}{\langle \sigma v \rangle}$. In order for the cosmological relic density to match the observed dark mater density, for a $100\,\mathrm{GeV}/c^2$ WIMP, a cross section of $10^{-9}\mathrm{GeV}^{-2}$ is required, which is the same order of magnitude as an electroweak process. This argument has lead to many experimental searches for WIMPs, including this work. Theoretically the WIMP could be explained with extensions of the standard model. A popular such extension is the theory of Supersymmetry (SUSY), a theory that includes gravity and would address many SM issues. In the theory that minimally extends the SM, the Minimal Supersymmetric Standard Model (MSSN), the WIMPs could be explained by the lightest stable, electrically and strongly neutral particles in the model, the neutralino or the gravitino fermions. However the neutralino is preferred since from cosmological calculations under supersymmetric hypotheses, its relic density might match the observed energy density of the Universe [24].

1.4.1 WIMP detection

There are multiple channels of detection that can be used for experimental WIMP searches. In Figure 1.3 are illustrated the channels through which WIMPs can interact with SM particles with an unknown coupling.

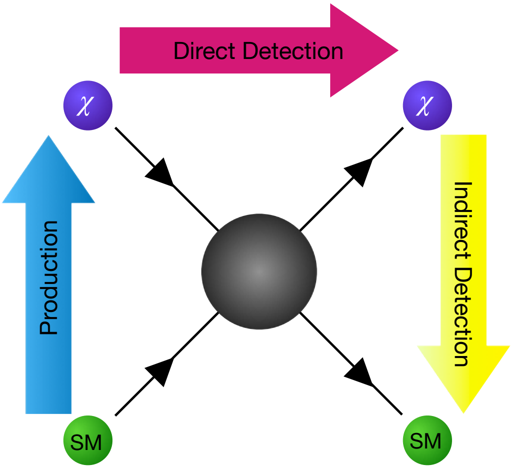

Figure 1.3: Diagram of the three possible channels of investigating dark matter. The yellow arrow shows the indirect detection channel through dark matter annihilation into SM matter, the red arrow shows the direct detection channel of dark matter scattering on SM matter, and the blue arrow shows the production of DM particles from SM particles at colliders.

Indirect searches rely on WIMP annihilation in overdense regions of the universe as would be galaxy centres or regions of space dominated by dark matter density, as dwarf galaxies. The annihilations would produce high energy standard model particles which can create gamma ray photons. Searches for excesses of gamma ray photons coming from high dark matter density regions are carried out through gamma ray telescopes in space, such as Fermi-LAT [25], or high energy gamma-ray Cherenkov telescope arrays on the ground, such as HESS[26] and CTA [27]. Dark matter annihilation can be also probed with charged cosmic rays. One possible signature of cosmic rays from dark matter would be an excess of the flux of antimatter in primary cosmic rays [28]. Space experiments such as PAMELA [29], FERMI-LAT and AMS [30] have measured the primary cosmic ray flux and observed an excess in the positron spectrum, however this observation could be explained by other astrophysical production processes such as pulsars [31].

Dark matter annihilation in overdense regions, such as the Sun or the galactic centre, can produce high energy neutrinos. Earth based neutrino telescopes such as ANTARES [32] and IceCube [33, 34] can probe this channel and constrain dark matter interactions.

Accelerator based experiments, such as the ones at the Large Hadron Collider, can probe the production channel of WIMPs. By accelerating standard model particles to high energies and making them collide, there might be a chance to create dark matter particles in the process. Since the WIMPs are expected to be neutral stable particles, they would pass through the detectors undetected and their signature would be missing energy and momentum in the interaction products.

Finally, direct detection searches look for scattering signatures of dark matter particles off normal matter. When a WIMP passes through normal matter with a given amount of kinetic energy there is a possibility that it interacts and scatters off, transferring some of its kinetic energy to the standard model particles. The tiny amount of energy lost by the WIMP in principle could be detected through a variety of different ways since it could cause a heat increase, ionisation or produce scintillation light.

2. WIMP direct detection and the Effective Field Theory approach

This chapter discusses the principles of direct detection of WIMPs and goes into the detail of the Effective Field Theory (EFT) approach in direct detection. First the WIMP scattering and the computation of the expected number of events in a direct detection experiment are treated. Then the EFT approach is introduced, first in a non-relativistic EFT (NREFT) framework, as first proposed for direct detection experiments, then introducing the chiral EFT expansion (ChEFT). Lastly the ChEFT cross section and the nuclear response computation in direct detection experiments are discussed.

Experiments that aim to detect directly the dark matter interactions are designed to look for the scattering of dark matter particles in the detector volume. This can be achieved by measuring the very small energy of $\mathcal{O}(1\text{keV})$ that the target particles of the active volume acquire after the scattering. Three physical processes are possible to exploit for measuring the deposited energy: thermalization, excitation and ionization. In the thermalization process, recoiling particles off the active volume of the detector, after a scattering event happens, interact with other particles at rest and lose energy in the form of heat or vibrational states (phonons) if the detector medium is in a lattice configuration, as it is the case for solid state detectors. Excitation of the detector medium can also happen. In this case the following deexcitation can result in the production of scintillation photons. Finally particle recoils can cause the ionization of the medium in the detector which results in the liberation of free charges that can be extracted before recombination, by applying an external electric field, and read out as a charge signal.

In a detector, dark matter particles could scatter off either the nuclei or the electrons of the atoms of the active volume, producing nuclear recoils (NR) and electronic recoils (ER) respectively. In NR, the recoiling nucleus loses a large fraction of its energy by thermalization. In ER, electrons most likely will detach from the atomic shell becoming free, and in their path possibly scattering against other atoms with enough energy to free other electrons, causing an ionisation signal. The different signatures of ER and NR allow the discrimination of the two types of signal, crucial for many direct detection experiments.

2.1 WIMP elastic scattering

The simplest and most effective assumption for the detection of WIMPs is the elastic scattering against the nuclei of the detector medium. In fact NRs offer high sensitivity for dark matter particles of mass $m_\chi \simeq m_N$, where m_N is the mass of the scattering nucleus.

Considering a WIMP of mass m_χ and a detector medium with atomic nuclei of mass m_N, it is possible to compute the recoil energy of the nucleus in an elastic scattering as:

$$E_R = \frac{\mu_N^2 v^2 (1-\cos(\theta))}{m_N} \tag{2.1}$$

where μ_N is the reduced mass $\mu_N = m_\chi m_N/(m_\chi + m_N)$, v is the velocity of the dark matter particle and θ the angle of recoil. The minimum velocity at which a recoil would produce enough energy to be detectable in the detector is given from equation 2.1 as:

$$v_{min} = \sqrt{\frac{m_N E_{th}}{2\mu_N^2}} \tag{2.2}$$

where the energy threshold of the detector, E_{th}, is taken into account. This velocity is then used in the computation of the interaction rate in the detector. To compute the total interaction rate one has to integrate the WIMP-nucleus differential cross section over the velocity and the energy as in [35]:

$$R = \int_{E_{th}}^{\infty} \mathrm{d}E_R \frac{\rho_0}{m_N m_\chi} \int_{v_{min}}^{v_{max}} v f(v) \frac{\mathrm{d}\sigma_{\chi N}}{\mathrm{d}E_R}(v, E_R)\mathrm{d}v \tag{2.3}$$

where ρ_0 is the local dark matter density, v_{max} is the particle escape velocity v_{esc}, $f(v)$ is the velocity distribution of particles in Eq. 1.1 and $\frac{\mathrm{d}\sigma_{\chi N}}{\mathrm{d}E_R}(v, E_R)$ is the WIMP-nucleus differential cross section.

Due to the Earth orbiting the Sun, the velocity distribution in the Earth frame shows also a time dependence which can be written as a Galilean boost from the velocity distribution at rest in the galactic frame as

$$f(v,t) = f_{rest}(v_{obs}(t) + v). \tag{2.4}$$

Within the observed velocity v_{obs} the only relevant time dependent components are the Earth's orbital velocity and rotation [36], with the orbital velocity being the main component that could contribute consistently to a possible rate variation in a detector. This rate variation could be expressed in terms of differential rate approximately as

$$\frac{\mathrm{d}R}{\mathrm{d}E_R} \approx \left\langle \frac{\mathrm{d}R}{\mathrm{d}E_R} \right\rangle [1 + \Delta(E_r) cos\omega(t-t_0)] \tag{2.5}$$

where $\left\langle \frac{\mathrm{d}R}{\mathrm{d}E_R} \right\rangle$ is the mean differential rate, $\Delta(E_r)$ is the modulation amplitude, $\omega = 2\pi/\mathrm{yr}$ and t_0 is the time of the year when the Earth moves fastest with respect to the dark matter rest frame.

2.2 Non-relativistic Effective Field Theory (NREFT)

2.2.1 Spin Independent and Spin Dependent interactions

Classical treatment of elastic scattering however may not be the only way to study WIMP interactions with the detector medium. The classical elastic scattering treatment of the interaction corresponds to one of the two leading-order terms in a WIMP-nucleon effective field theories, the so called "spin independent" (SI) scattering, and the other one being the "spin dependent" (SD) scattering.

The SI and SD differential cross sections in terms of low momentum transfer q can be written as [37, 38]

$$\frac{\mathrm{d}\sigma_{SI(SD)}}{\mathrm{d}q} = \frac{8G_F^2}{(2J_i+1)v^2} S_{S(A)}(q) \tag{2.6}$$

where G_F is the Fermi constant, J_i is the initial angular momentum of the nucleus, v the WIMP velocity, while $S_S(q)$ and $S_A(q)$ are respectively the scalar and axial-vector structure factors which depend on the momentum transfer. In the SI cross section the structure factor leads to a coherence enhancement of $S_S \propto A^2$, where A is the number of nucleons in the isotopes of the detector. In the SD case the structure factor depends on the spin of the nucleons and can be written as

$$S_A(q) = a_0^2 S_{00}(q) + a_0 a_1 S_{01}(q) + a_1^2 S_{11}(q) \tag{2.7}$$

where the nuclear structure information is contained in the S_{ij} terms and the a_0 and a_1 are the coupling constants. The Eq. 2.7 for the limit of $q = 0$ becomes

$$S_A(0) = \frac{(2J+1)(J+1)}{4\pi J} \times |(a_0 + a_1')\langle \mathbf{S_p} \rangle + (a_0 - a_1')\langle \mathbf{S_n} \rangle|^2. \tag{2.8}$$

In this case a_1' contains possible corrections deriving from two-body currents contributions and $\langle \mathbf{S}_p \rangle$ and $\langle \mathbf{S}_n \rangle$ are the expectation values of the proton and neutron spin operators respectively. Classically, the SD searches use the cases of $a_0 = a_1 = 1$ and $a_0 = -a_1 = 1$, which correspond respectively to proton-only and neutron-only couplings, to constrain the theory. Since this response is heavily influenced by the spin of the nuclei, only isotopes with odd number of protons or odd number of neutrons are expected to be sensitive to the SD interaction.

2.2.2 Non-Relativistic Effective Field Theory framework

In some theoretical frameworks the SI and the SD interactions might be suppressed and other types of momentum dependent interactions could become dominant [39]. A possible way of approaching this problem is through a non-relativistic Effective Field Theory framework [40], since the WIMPs that are expected to interact in the detector have low enough velocity to be considered non-relativistic.

In the NREFT framework the effective Lagrangian of the WIMP-nucleus interaction is constructed by taking into account all the Galilean-invariant operators up to the second order in momentum transfer, taking the form of

$$\mathcal{L}_{NR} = \sum_{i,N} c_i^N \mathcal{O}_i^N \tag{2.9}$$

which is a sum over all the operators and the nucleons $N = n, p$, with the c_i^N being the coupling coefficients and $\mathcal{O}_i$ the operators. This framework includes 14 different operators, including the SI and SD ones, assumed to have independent couplings to protons and neutrons:

$$\begin{aligned}
\mathcal{O}_1 &= \mathbf{1}_\chi \mathbf{1}_N, & \mathcal{O}_9 &= i\mathbf{S}_\chi \cdot \left(\mathbf{S}_N \times \frac{\mathbf{q}}{m_N}\right), \\
\mathcal{O}_3 &= i\mathbf{S}_N \cdot \left(\frac{\mathbf{q}}{m_N} \times \mathbf{v}^\perp\right), & \mathcal{O}_{10} &= i\mathbf{S}_N \cdot \left(\frac{\mathbf{q}}{m_N}\right), \\
\mathcal{O}_4 &= \mathbf{S}_\chi \cdot \mathbf{S}_N, & \mathcal{O}_{11} &= i\mathbf{S}_\chi \cdot \left(\frac{\mathbf{q}}{m_N}\right), \\
\mathcal{O}_5 &= i\mathbf{S}_\chi \cdot \left(\frac{\mathbf{q}}{m_N} \times \mathbf{v}^\perp\right), & \mathcal{O}_{12} &= \mathbf{S}_\chi \cdot (\mathbf{S}_N \times \mathbf{v}^\perp), \\
\mathcal{O}_6 &= \left(\mathbf{S}_\chi \cdot \frac{\mathbf{q}}{m_N}\right)\left(\mathbf{S}_N \cdot \frac{\mathbf{q}}{m_N}\right), & \mathcal{O}_{13} &= i(\mathbf{S}_\chi \cdot \mathbf{v}^\perp)\left(\mathbf{S}_N \cdot \frac{\mathbf{q}}{m_N}\right), \\
\mathcal{O}_7 &= \mathbf{S}_N \cdot \mathbf{v}^\perp, & \mathcal{O}_{14} &= i\left(\mathbf{S}_\chi \cdot \frac{\mathbf{q}}{m_N}\right)(\mathbf{S}_N \cdot \mathbf{v}^\perp), \\
\mathcal{O}_8 &= \mathbf{S}_\chi \cdot \mathbf{v}^\perp, & \mathcal{O}_{15} &= -\left(\mathbf{S}_\chi \cdot \frac{\mathbf{q}}{m_N}\right)\left[(\mathbf{S}_N \times \mathbf{v}^\perp) \cdot \frac{\mathbf{q}}{m_N}\right].
\end{aligned} \tag{2.10}$$

In Eq. 2.10 it is possible to observe that the operators depend on four linearly independent quantities, which are the relative perpendicular velocity of the WIMP with respect to the nucleus $\mathbf{v}^\perp \equiv \mathbf{v} + \frac{\mathbf{q}}{2\mu_N}$, the momentum transfer $\mathbf{q}$ and the spins of the WIMP and the nucleus, respectively $\mathbf{S}_\chi$ and $\mathbf{S}_N$, with operators $\mathcal{O}_1$ and $\mathcal{O}_4$ corresponding respectively to the SI and the SD interactions. The direct dependence on the momentum transfer $\mathbf{q}$ of many of the operators, make the scattering rate for these interactions to go to zero at low energy creating a peak in the rate at non-zero recoil energy, thus creating different signatures in the detector from the SI and SD interactions.

Given that the operators can couple to protons and neutrons independently i.e. with different coupling coefficients for each nucleon, the analysis space for the NREFT is quite vast. For simplicity most of the EFT analyses of direct detection experiments' data is done in the isoscalar case, assuming $c_i^p = c_i^n$ [41], or studying the couplings to the nucleons individually assuming only proton or only neutron couplings [42]. The single operators are also treated independently and the response is studied by turning on one operator at the time.

While this approach is justified by the assumption that WIMPs should be non-relativistic particles, it renders difficult connections to high energy physics searches. In particular this method effectively integrates out the physics scales related to QCD spontaneous breaking of chiral symmetry including these effects into the coefficients [43]. To study the WIMP parameter space in QCD given experimental limits on NREFT operators further steps are required.

2.3 Chiral EFT

A possible alternative to the NREFT basis is to start from chiral EFT (ChEFT) and include QCD constraints on the nuclear responses using chiral symmetry. This approach starts from an EFT of dark matter that couples to quarks, gluons and photons at low energies, preserving QCD symmetries, and capturing the importance of pions in low energy interactions within nuclei [44–46].

The first step to describe the dark matter interactions by a ChEFT is to consider the interactions generated by mediators much heavier than $\mathcal{O}(1\mathrm{GeV})$ and write the Lagrangian of interaction between WIMPs and SM particles as a sum of higher order operators [47]

$$\mathcal{L}_\chi = \sum_{a,i,d} \frac{C_{a,i}^{(d)}}{\Lambda^{d-4}} \mathcal{Q}_{a,i}^{(d)} . \tag{2.11}$$

In Eq. 2.11 the sum runs over the operator type and dimension, i and d, as well as to what SM particle it couples to, a, which can be quarks, gluons or photons, the C_as indicate the dimensionless Wilson coefficients while Λ is the scale that can be identified as the mediator mass and $\mathcal{Q}$ the fundamental interaction operators.

At this point the ChEFT can be mapped to the single nucleon couplings of NREFT. The matching onto the NREFT operators shows how these operators are not independent in the ChEFT scheme.

For this dissertation, the preferred ChEFT approach is the study of generalised

SI scattering with the inclusion of all coherent contributions up to dimension-eight, which considers WIMP couplings to one and two nucleons proposed in Ref. [45].

2.3.1 ChEFT generalised SI interaction

The generalised SI interaction considered is a decomposition of the WIMP-nucleus cross section $\sigma^{SI}_{\chi\mathcal{N}}$ based on whether coherence enhancement of fundamental ChEFT operators' effects is possible, and it includes isoscalar and isovector standard SI WIMP-nucleon interactions as well as two-body current WIMP interactions. The WIMP-nucleus differential cross section can be expressed as

$$\begin{aligned}\frac{\mathrm{d}\sigma^{SI}_{\chi\mathcal{N}}}{\mathrm{d}q^2} = \frac{1}{4\pi v^2}\Bigg| \sum_{I=\pm}\left(c_I^M - \frac{q^2}{m_N^2}\dot{c}_I^M\right)\mathcal{F}_I^M(q^2) + c_\pi\mathcal{F}_\pi(q^2) + c_b\mathcal{F}_b(q^2) + \\ \frac{q^2}{2m_N^2}\sum_{I=\pm} c_I^{\Phi''}\mathcal{F}_I^{\Phi''}(q^2)\Bigg|^2 + \frac{1}{4\pi v^2}\sum_{i=5,8,11}\left|\sum_{I=\pm}\xi_i(q,v^\perp)c_I^{M,i}\mathcal{F}_I^M(q^2)\right|^2,\end{aligned} \tag{2.12}$$

which contains the structure factors $\mathcal{F}$, containing the nuclear information of the scattering, and the couplings c, containing information about the Wilson coefficients that describe the fundamental WIMP interactions with quarks and gluons, convolved with the hadronic matrix elements, and depend on the BSM scenario considered, e.g. WIMP spin or interaction type with the SM particles. The last term of Eq. 2.12 contains the kinematic factors $\xi_5 = \frac{\mu_N q v^\perp}{2m_\chi m_N}$, $\xi_8 = v^\perp$ and $\xi_{11} = -\frac{q}{2m_\chi}$ which come in from the contribution of the previously defined (Eq.2.10) NREFT operators $\mathcal{O}_{5,8,11}$.

This kind of decomposition can already give information about BSM physics by studying the individual couplings. One such example is analysis of the WIMP-pion coupling performed by the XENON Collaboration [48], where by considering only the term $c_\pi\mathcal{F}(q^2)$ in Eq.2.12 that arises from the WIMP interaction with virtual pions exchanged in the nucleus, it was possible to place constraints on the scalar WIMP-pion interaction cross section.

Eq.2.12 is constructed though directly from ChEFT. Considering a spin-1/2

WIMP, the ChEFT Lagrangian with terms up to dimension-8 is:

$$
\begin{aligned}
\mathcal{L}_\chi &= \mathcal{L}_\chi^{(5)} + \mathcal{L}_\chi^{(6)} + \mathcal{L}_\chi^{(7)} + \mathcal{L}_\chi^{(8)} \\
\mathcal{L}_\chi^{(5)} &= \frac{C_F}{\Lambda}\bar{\chi}\sigma^{\mu\nu}\chi F_{\mu\nu} + \frac{\tilde{C}_F}{\Lambda}\bar{\chi}\sigma^{\mu\nu}\chi\tilde{F}_{\mu\nu} \\
\mathcal{L}_\chi^{(6)} &= \frac{1}{\Lambda^2}\sum_q \Bigg[C_q^{VV}\bar{\chi}\gamma^\mu\chi\bar{q}\gamma_\mu q + C_q^{AA}\bar{\chi}\gamma^\mu\gamma_5\chi\bar{q}\gamma_\mu\gamma_5 q + C_q^{AV}\bar{\chi}\gamma^\mu\gamma_5\chi\bar{q}\gamma_\mu q \\
&\quad + C_q^{TT}\bar{\chi}\sigma^{\mu\nu}\chi\bar{q}\sigma_{\mu\nu}q + \tilde{C}_q^{TT}\bar{\chi}\sigma^{\mu\nu}i\gamma_5\chi\bar{q}\sigma_{\mu\nu}q \Bigg], \\
\mathcal{L}_\chi^{(7)} &= \frac{1}{\Lambda^3}\Bigg[\sum_q \left(C_q^{SS} + \frac{8\pi}{9}C_g^{\prime S} \right)\bar{\chi}\chi m_q\bar{q}q + \sum_q \left(C_q^{PS} + \frac{8\pi}{9}\tilde{C}_g^{\prime S} \right)\bar{\chi}i\gamma_5\chi m_q\bar{q}q \\
&\quad - \frac{8\pi}{9}C_g^{\prime S}\bar{\chi}\chi\theta_\mu^\mu - \frac{8\pi}{9}\tilde{C}_g^{\prime S}\bar{\chi}i\gamma_5\chi\theta_\mu^\mu \Bigg] \\
\mathcal{L}_\chi^{(8)} &= \frac{1}{\Lambda^4}\left[\sum_q C_q^{(2)}\bar{\chi}\gamma_\mu i\partial_\nu\chi\bar{\theta}_q^{\mu\nu} + C_g^{(2)}\bar{\chi}\gamma_\mu i\partial_\nu\chi\bar{\theta}_g^{\mu\nu} \right]
\end{aligned}
\tag{2.13}
$$

where the listed operators have all an effect towards coherently enhanced responses, with the exception of the Axial-vector⊗Axial-vector (AA) interaction, with the Wilson coefficient C_q^{AA}, which is shown because it is one of the contributions to the standard SD interaction discussed in Section 2.2.1. In this Lagrangian, in principle, the sums run over all the quark flavours q, with the exception of the correction in dimension-7 gluon couplings, where $C_g^{\prime S} = C_g^S - \frac{1}{12\pi}\sum_{Q=c,b,t}C_Q^{SS}$ and $\tilde{C}_g^{\prime S} = \tilde{C}_g^S - \frac{1}{12\pi}\sum_{Q=c,b,t}C_Q^{PS}$, where the heavy quark contributions are integrated inside. The gluon operators have also the term θ_μ^μ which is the trace of the energy-momentum tensor

$$
\theta_\mu^\mu = \sum_q m_q\bar{q}q - \frac{9}{8\pi}\alpha_s G_{\mu\nu}^a G_a^{\mu\nu} + \mathcal{O}(\alpha_s^2), \tag{2.14}
$$

where $\bar{\chi}\chi\alpha_s G_{\mu\nu}^a G_a^{\mu\nu}$ and $\bar{\chi}i\gamma_5\chi\alpha_s G_{\mu\nu}^a G_a^{\mu\nu}$ in the Lagrangian form the gluon operators with coefficients C_g^S and $\tilde{C}_g^S$ respectively. In the dimension-8 Lagrangian the spin-2 contribution is introduced where the $\bar{\theta}_{q,g}^{\mu\nu}$ are the traceless components of the energy-momentum tensor:

$$
\begin{aligned}
\bar{\theta}_q^{\mu\nu} &= \frac{1}{2}\bar{q}\left(\gamma^{\{}iD_-^{\nu\}} - \frac{m_q}{2}g^{\mu\nu} \right)q, \\
\bar{\theta}_g^{\mu\nu} &= \frac{g^{\mu\nu}}{4}G_{\lambda\sigma}^a G_a^{\lambda\sigma} - G_a^{\mu\lambda}G_{a\lambda}^\nu
\end{aligned}
\tag{2.15}
$$

where D_-^μ is the covariant derivative $D_-^\mu = \overrightarrow{D}^\mu - \overleftarrow{D}^\mu$ and $\gamma^{\{}iD_-^{\nu\}}$ is a symmetrizer $\gamma^{\{}iD_-^{\nu\}} = (\gamma^\mu iD_-^\nu - \gamma^\nu iD_-^\mu)/2$.

The only part that stands out with respect to the rest in Eq. 2.13 is the dimension-5 Lagrangian which describes long-range interactions through photon exchange and mostly concern dark matter candidates that posses a non-vanishing dipole moment [49].
In Eq. 2.12 the coefficients c are directly related to the Wilson coefficients of Eq. 2.13, in particular they are a combination of Wilson coefficients and nucleon matrix elements. We give in this case the example of the pion coupling coefficient c_π, which can be written as:

$$c_\pi = \zeta(f_\pi + 2f_\pi^\theta - \frac{1}{2}f_\pi^{(2)}) \tag{2.16}$$

where $\zeta = 1$ for a Dirac particle and the f-terms are the specific couplings

$$\begin{aligned} f_\pi &= \frac{M_\pi}{\Lambda^3}\sum_{q=u,d}\left(C_q^{SS} + \frac{8\pi}{9}C_g^{\prime S}\right)\mathrm{f}_q^\pi \\ f_\pi^\theta &= -\frac{M_\pi}{\Lambda^3}\frac{8\pi}{9}C_g^{\prime S} \\ f_\pi^{(2)} &= \frac{m_\chi M_\pi}{\Lambda^4}\left(\sum_q C_q^{(2)}\mathrm{f}_{q,\pi}^{(2)} + C_g^{(2)}\mathrm{f}_{g,\pi}^{(2)}\right), \end{aligned} \tag{2.17}$$

in which the Wilson coefficients appear as well as the nucleon matrix elements f. The coefficients of Eq. 2.12 are constructed in a similar way.

2.3.2 Structure factors and matching to NREFT

In order to fully describe the WIMP-nucleus interactions the possible nuclear responses have to be analysed. These responses of the WIMP-nucleon couplings are described by the structure factors [45, 50], which play an important role in the connection between NREFT and ChEFT.
Eq. 2.12 depends on six independent structure factors $\mathcal{F}$, four describing WIMP couplings to a single nucleon, $\mathcal{F}_\pm^M$ and $\mathcal{F}_\pm^{\Phi''}$, and two two-body structure factors, $\mathcal{F}_b$ and $\mathcal{F}_\pi$.
The structure factors differ according to the nuclear structure of the elements in the detector medium where the scattering occurs and they are computed with the evaluation of nuclear matrix elements with multipole operators. To compute them the many-body approach of the large scale nuclear shell model is used in the case of nuclear ground states and low energy excited states.
In particular, the process starts from the computation of the amplitudes of the various couplings that can be calculated by evaluating the currents of the couplings with the non-relativistic spinors of the WIMP and of the nucleons [51]. Taking the example of the scalar-scalar coupling it is

$$\mathcal{M}^{SS} = \chi_{\chi'}^\dagger \chi_\chi \chi_{n'}^\dagger f_N(t)\chi_n \tag{2.18}$$

Multipole operator	NREFT operators	ChEFT amplitudes
M	$\mathcal{O}_1$, $\mathcal{O}_5$, $\mathcal{O}_8$, $\mathcal{O}_{11}$	$\mathcal{M}^{VV}$, $\mathcal{M}^{SS}$, $\mathcal{M}^{AV}$, $\mathcal{M}^{PS}$, $\mathcal{M}^{TT}$, $\mathcal{M}^{\tilde{T}T}$
Σ'	$\mathcal{O}_3$, $\mathcal{O}_4$, $\mathcal{O}_7$, $\mathcal{O}_9$	$\mathcal{M}^{AA}$, $\mathcal{M}^{AV}$, $\mathcal{M}^{VV}$
Σ"	$\mathcal{O}_4$, $\mathcal{O}_6$, $\mathcal{O}_{10}$	$\mathcal{M}^{AA}$, $\mathcal{M}^{SP}$, $\mathcal{M}^{VV}$, $\mathcal{M}^{PP}$
Δ	$\mathcal{O}_5$, $\mathcal{O}_8$	$\mathcal{M}^{AV}$
Φ"	$\mathcal{O}_3$	$\mathcal{M}^{VV}$, $\mathcal{M}^{TT}$

Table 2.1: Matching of NREFT operators and one-body ChEFT amplitudes to the nuclear multipole operators. Here are reported for completeness also ChEFT amplitudes ($\mathcal{M}^{AA}$, $\mathcal{M}^{SP}$, $\mathcal{M}^{PP}$) that contribute to the SD response that do not show coherent enhancement.

where $\chi_{\chi,n}$ are the non-relativistic spinors of the WIMP and the nucleon and $f_N(t)$ is the momentum transfer dependent WIMP-nucleon coupling that depends on the Wilson coefficients in eq. 2.13, with $t = -q^2$.
For the one-body currents an alternative approach is possible and that is the matching to the NREFT framework described in Sec.2.2.2. Considering the operators in 2.10, the amplitudes of the various channels can be written as a combination of one or more NREFT operators and and the momentum transfer dependent couplings $f(t)$ [47]. This type of matching, besides of providing a link to the NREFT framework shows as well that due to QCD effects the NREFT operators are not independent and should not be treated as such in analyses such as Ref. [41, 42].
At this point, given that the NREFT operators have been mapped to five nuclear multipole operators [50], it is possible to obtain a direct matching of the chiral amplitudes to the multipole operators as reported in Table 2.1.
The two-body current couplings cannot be mapped to the NREFT basis because the NREFT operators describe only one-body couplings. This means that the three two-body amplitudes, $\mathcal{M}_2^{SS}$, $\mathcal{M}_2^{\theta}$ and $\mathcal{M}_2^{(2)}$, which in turn can be translated in only two, $\mathcal{M}_2^{SS}$ and $\mathcal{M}_b$, are constructed directly with use of pion poles and nucleon spin and isospin operators and evaluated in the shell model to obtain the two structure factors $\mathcal{F}_\pi(q^2)$ and $\mathcal{F}_b(q^2)$ [45].

While the generalised SI ChEFT framework may not provide as a full study of the ChEFT decomposition as in Ref. [46, 47], or DirectDM framework for simplicity, from a particle physics point of view, it provides a more complete study of the nuclear response, including the two-body amplitudes, thus the two frameworks can be considered complementary. One important missing contribution in the generalised SI framework is the Axial-vector⊗Axial-vector interaction channel, which we will not include in the analysis of the single operator contributions. For completeness however we will provide constraints also on

a set of operators with the DirectDM tools [52] that are compatible with the generalised SI framework, specifically the dimension-5 dipole operators, corresponding to $\mathcal{Q}_{1,2}^{(5)}$ in [47], the dimension-6 Vector$\otimes$Vector (VV) and Axial-vector$\otimes$Vector (AV) operators, $\mathcal{Q}_{1,q}^{(6)}$ and $\mathcal{Q}_{2,q}^{(6)}$ respectively, and dimension-7 Scalar-gluon, $\mathcal{Q}_{1,2}^{(7)}$ (S_g and $\tilde{S}_g$), Scalar$\otimes$Scalar (SS), $\mathcal{Q}_{5,q}^{(7)}$, and Pseudo-scalar$\otimes$Scalar (PS) operators, $\mathcal{Q}_{6,q}^{(7)}$.
Even if these operators are comparable by definition, there are some fundamental differences in some cases:

- the dimension-5 magnetic dipole operator $\frac{C_F}{\Lambda}\bar{\chi}\sigma^{\mu\nu}\chi F_{\mu\nu}$, according to the general philosophy of the generalised SI framework matches only to the coherently enhanced contributions of the NREFT operators $\mathcal{O}_1$ and $\mathcal{O}_5$, while in the DirectDM framework it matches also onto the operators $\mathcal{O}_4$ and $\mathcal{O}_6$;

- The dimension-7 Scalar-gluon, S_g, ($\mathcal{Q}_1^{(7)}$), and SS$_q$ ($\mathcal{Q}_{5,q}^{(7)}$) operators, in the generalised SI framework contribute to the pion matrix elements within the coefficients c_π and c_b in Eq. 2.12, which cannot be mapped to the single-nucleon NREFT operators, which are necessary for the DirectDM framework to compute the nuclear response.

3. ChEFT analysis of XENON1T data

This chapter presents the use of the ChEFT framework shown in Sec.2.3 for an analysis of XENON1T data. In this work we present the XENON1T detector, the background modelling, the inference, and the final results of the ChEFT analysis, including the study of three benchmark models to assess the effect of possible isospin-breaking interactions in the leading contributions for Dirac Dark Matter, Majorana Dark Matter and scalar-mediated fermion Dark Matter. This chapter refers to the work presented in [PAPER I].

3.1 XENON1T

The XENON1T experiment is a dual-phase Time Projection Chamber (TPC), detecting the scintillation light coming from the energy deposition of a recoil inside the active volume and the electrons released in the ionisation of the medium due to the recoiling particles. The detector is situated at Laboratori Nazionali del Gran Sasso (LNGS), in Italy and has recently been decommissioned in 2019 after more than 2 years of operation and data taking.
The analysis presented in this work is based on the two dark matter search runs used to report also the main SI result [53]. The first data-set, labelled as science run 0 (SR0), accounts for 32.1 d of exposure time, while the second data-set, labelled as science run 1 (SR1) accounts for an exposure of 246.7 d.

3.1.1 Dual phase TPC

In Figure 3.1 the operating principle of a dual-phase TPC is shown. When a particle interacts in the volume of liquid xenon and produces an energy deposition, the process generates UV scintillation light, ionisation of the atoms in the area of interaction and heat. The scintillation light is a short prompt emission of photons that can be observed by the two photomultiplier tube (PMT) arrays, on the top and on the bottom of the detector. This first prompt signal is labelled as S1. The electrons liberated from the ionisation of xenon atoms drift towards the top of the TPC due to an applied electric field of 120 V cm^{-1} in SR0, later reduced to 81 V cm^{-1} in SR1, between the cathode and the gate

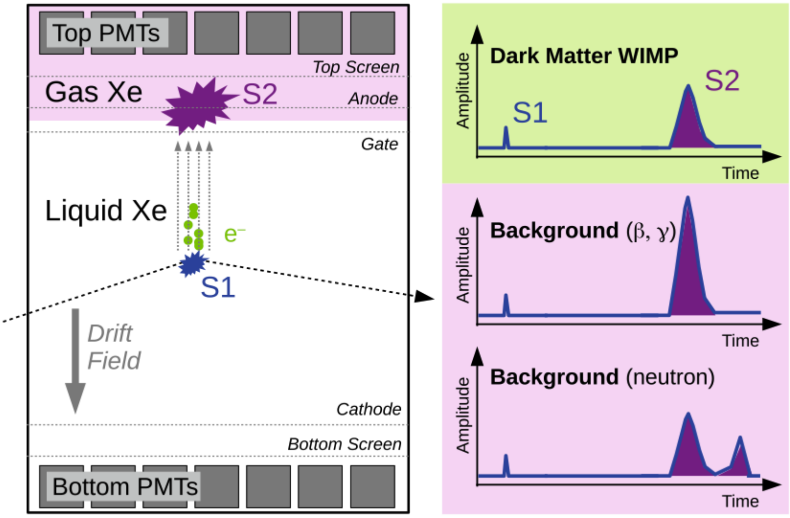

Figure 3.1: Schematic explanation of the dual-phase TPC operating principle from Ref.[54]. In the left panel is shown the simplified scheme of a signal generation due to a WIMP scattering (dashed arrow) in a dual-phase TPC. On the right there are three examples of signals recorded in the PMT arrays, showing the small and narrow S1 followed by a larger and broader S2 signal. Background signals (purple plots on the right) show the different ratio between S1 and S2 for ER with respect to the WIMP NR signal and the possible multiple scatters of background neutrons (lowest panel).

wire grids. When they reach the gas phase at the top of the detector, due to the stronger ($\sim$10kV cm^{-1}) field between the gate and the anode grids, they are accelerated causing a second stronger emission of scintillation light proportional to the number of electrons extracted, that is detected by the PMT arrays and labelled as S2. The S2 signature is generally broader in time and larger than the S1, due to diffusion of the drifting electrons in the liquid and the higher number of recoils generating light in the gas. The time delay between the S1 and the S2, gives information about the depth, Z, of the interaction site, while the x,y coordinates can be estimated from the pattern of the S2 signal in the top PMT array.

3.1.2 The XENON1T experiment

The XENON1T TPC is located inside a suspended cryostat filled with 3.2t of ultra pure liquid xenon. The active volume of the TPC i.e. where signals can arise and be recorded, contains around 2t of liquid xenon. The TPC is cylindrical, 97cm high and with a radius of 47.9cm. It consists of a field cage with copper field shaping electrodes in order to create a constant electric field inside. The anode and the cathode of the TPC consist of wire grids, with the addition of a gate grid, just below the surface of the liquid xenon to create a higher electric field in the gaseous phase, as illustrated in Figure 3.1. To protect the top and the bottom PMT arrays from possible electrical discharges two more wire grids are placed above the bottom array and under the top array. The two PMT arrays consist of a total of 248 3-inch Hamamatsu R11410-21 PMTs, divided in 127 PMTs in the top array, distributed in concentric rings to maximise the radial resolution in reconstructing the position of the events, and 121 PMTs in the bottom array, packed in a hexagonal pattern for the maximisation of the light collection. Furthermore, the inner walls of the TPC consist of 24 panels of PTFE, a highly reflective material for the xenon scintillation light wavelength.

The experiment is situated in the underground laboratory under the Gran Sasso mountain, with roughly 3.6 km of water equivalent shielding against the cosmic rays provided by the mountain rock. In addition to the location, the cryostat is suspended in a 740m^3 water tank, shielding from environment radiation, instrumented with 84 PMTs to measure Cherenkov radiation from muons (or their by-products) that make it through to the underground lab and to the detector and veto the events (muon veto system).

The experiment also employs a cryogenic system to keep the xenon in liquid phase around -100°C, coupled to a purification and re-circulation system that allows constantly circulate the xenon in the detector to eliminate impurities to very high levels. A krypton distillation column is also used, that allowed to reduce the krypton-to-xenon ratio to $(0.66 \pm 0.11) \times 10^{-12}$.

3.1.3 Signal emission model in XENON1T

When it comes to the choice of target material for a WIMP detector, xenon offers some very interesting advantages. In liquid phase it has a high density of 3.06 g/cm^3 and a radiation length X_0 of 2.77 cm [55] which means that it allows the construction of a moderate dimension detector with a high target mass and at the same time provides self-shielding of the inner volume against external radiation. Xenon is also a good scintillator emitting light at a wavelength of 178 nm and its high atomic number is well suited for rare interactions whose rates are coherently enhanced as $\propto A$ or A^2.

The modelling of the detector response to a signal production in the active volume is a crucial step. To do so we start from the distribution of the energy deposition into the three channels, ionisation, excitation and heat, and model how it impacts the observable light of the scintillation process, S1, and the extracted electrons, S2. An interaction of an incoming particle in the liquid xenon might involve either an electron of the electron cloud of the xenon atoms, causing an electron recoil (ER), or a xenon nucleus, causing a nuclear recoil (NR). As illustrated in Figure 3.1, the signal size differs according to which is the recoiling particle. The model used in XENON1T for the signal generation is based on the Noble Element Simulation Technique (NEST) model of liquid xenon response [56, 57]. In this section we will briefly discuss the signal emission model of XENON1T and the microphysics involved.

When a recoil involving a xenon atom happens, the atom will lose energy through excitation and ionisation of other atoms along its track, and kinetic energy transfer which resolves in heat. The excited atoms cannot de-excite alone, but to do so they form temporary bounds with non-excited atoms in the form of excited two-atom molecules (excitons), which then de-excite with the emission of scintillation light at 178 nm wavelength. The ions produced from the ionisation, without an applied electric field recombine, producing further excitons and scintillation light, however the applied electric field separates the electrons from the positive ions, reducing the recombination rate and permitting the extraction of electrons towards the top of the TPC and the production of the second proportional light signal, S2.

Electronic recoils are produced by β and γ radiation and almost all the energy deposition happens through scintillation and ionisation, thus the measured energy of the signals correspond closely to the true recoil energy [58]. Nuclear recoils however lose energy also to atomic motion (heat), losing around 80% of the recoil energy this way for recoils in the range of 1keV-100keV [59]. The fraction of the energy lost to heat is expressed through the Lindhard factor L [58].

For a recoil happening in the liquid xenon of true energy ε, the measurable energy is divided between number of excitons, N_{ex}, and number of electron-ion pairs, N_i, produced, according to

$$\varepsilon \cdot L = \langle N_{ex} + N_i \rangle \cdot W, \tag{3.1}$$

where L is the Lindhard factor and $W = (13.7 \pm 0.2)\mathrm{eV}$, which is the average energy required to create an exciton or an electron-ion pair, while $\langle N_{ex} + N_i \rangle$ are the average number of such detectable quanta. To reconstruct the energy deposition ε in terms of number of detectable quanta, $N_q = N_{ex} + N_i$, we model the distribution of N_q with a Binomial fluctuation

$$N_q \sim \mathrm{Binom}(\varepsilon / W, L), \tag{3.2}$$

since some of the energy could be lost to thermalization.

For ER, the energy loss to heat is minimal and the exciton-to-ion ratio thus is assumed constant and it is given a uniform prior distribution between 0.06 and 0.20 in the fit of calibration data [60]. For NR, N_q is parametrized as

$$\left\langle \frac{N_{ex}}{N_i} \right\rangle = \alpha |\mathbf{E}|^{-\zeta} (1 - e^{-\beta\varepsilon}) \tag{3.3}$$

with α, β and ζ as fittable free parameters and $\mathbf{E}$ being the electric field. The fluctuations of both N_{ex} and N_i are assumed binomial, with the additional probability, r, for N_i that some electrons are lost due to recombination, and create new excitons. The mean recombination fraction $\langle r \rangle$ is described by the Thomas-Imel model [61] and depends on the deposited energy and the electric field as

$$\langle r \rangle = 1 - \frac{\ln(1 + N_i\varsigma/4)}{N_i\varsigma/4}, \tag{3.4}$$

where ς is the field- and energy-dependent parameter of the model. The recombination fraction fluctuations for each event due to detector effects are modelled with a Gaussian distribution as $r \sim \text{Gaus}(\langle r \rangle, \Delta r)$.

While for the NR, the Thomas-Imel model works well, for the ER the Eq.3.4 does not fully describe the recombination processes [62] and a slightly modified model is used:

$$\langle r \rangle_{er} = \frac{1 - \frac{\ln(1+N_i\varsigma_{er}/4)}{N_i\varsigma_{er}/4}}{1 + e^{-(\varepsilon - q_0)/q_1}} \tag{3.5}$$

where $\varsigma_{er} = \gamma_{er} e^{-\varepsilon/\omega_{er}} |\mathbf{E}|^{-\delta_{er}}$. The parameters q_0, q_1, γ_{er}, ω_{er} and δ_{er} are all free parameters obtained in the fit of the signal emission model to the calibration data of XENON1T. The recombination fluctuation is modelled according to an empirical function as

$$\Delta r = q_2 (1 - \exp(-\varepsilon/q_3)), \tag{3.6}$$

where q_2 and q_3 are free parameters. Finally, the mean photon yield, $\langle N_\gamma \rangle / \varepsilon$, from the scintillation process, and the mean electron yield $\langle N_e \rangle / \varepsilon$ are obtained as

$$\langle N_\gamma \rangle / \varepsilon = \frac{1}{W} \frac{\langle r \rangle + \langle N_{ex}/N_i \rangle}{1 + \langle N_{ex}/N_i \rangle}, \tag{3.7}$$

$$\langle N_e \rangle / \varepsilon = \frac{1}{W} \frac{1 - \langle r \rangle}{1 + \langle N_{ex}/N_i \rangle}, \tag{3.8}$$

and the detectable quanta for each event being $N_e \sim \text{Binom}(N_i, 1 - r)$ and $N_\gamma = N_q - N_e$. By convolving the detectable electrons and photons with the detector response, we obtain the model for the recoil distributions in the analysis variables, corrected S1 (cS1) and corrected S2 (cS2), which account for corrections for the inhomogeneities of the detector response.

3.1.4 Event reconstruction

Given a signal in the detector, the reconstruction of the event is the step when the scintillation light and the ionization are identified and the three-dimensional location of the interaction is reconstructed.

In the XENON1T experiment the events are identified by a data acquisition (DAQ) system which records the signals from the PMTs. A trigger looks for clusterings of individual PMT waveforms and stores the data for the maximum drift time in the TPC i.e. the time an electron would take to drift up from the bottom of the TPC, before and after the identified cluster [63]. In the stored waveforms the reconstruction software PAX [64] will identify the clusters as either S1-s or S2-s according to rise-time of the signal and the number of PMTs involved, and construct the event by pairing the largest S1 with the largest S2 that comes after it.

The depth of the event will be reconstructed from the time difference between S1 and S2.

For the x, y position reconstruction and the energy reconstruction all the hits per PMT are summed up to obtain a hit pattern for the top and bottom arrays. The S1 signal will have a higher amount of energy seen in the bottom array due to the internal reflection at the liquid-gas interface. The S2 signal is seen with both arrays, however the top array, due to the high amount of light produced close to the PMTs will have in general a certain quantity of PMTs saturating, thus for the energy reconstruction of the S2 only the bottom array is used.

The x, y position is reconstructed using the top array that detects the S2 proportional scintillation light produced in close proximity to it. To estimate the position, an optical Monte Carlo, tuned on ^{83m}Kr calibration data, is used to generate hit patterns from true S2 positions, then they are averaged and used in a maximum likelihood fit that reconstructs the position with a resolution of $\sigma_r \sim 2\,\mathrm{cm}$ [12, 65]; the method is called *Top pattern fit*. Another reconstruction method that is used is the neural network position reconstruction algorithm, which uses a neural network trained on the simulated hit patterns and has similar performances to the *top pattern fit* [63].

The electrical field in the TPC in the ideal case should be uniform, however in the XENON1T case, due to edges' effects, it shows also a slight outwards component in the outer regions of the TPC and at low Z. Electrons drifting from areas close to the detector's edge will have a curved path and are reconstructed at a lower radius, while events happening deep in the TPC show a radius misreconstruction due to the accumulation of charge on the TPC walls. To correct for these effects ^{83m}Kr calibration data is used. ^{83m}Kr events are assumed to be distributed uniformly in the detector since the calibration source is diffused in the liquid xenon. The observed distribution of these calibration events shows

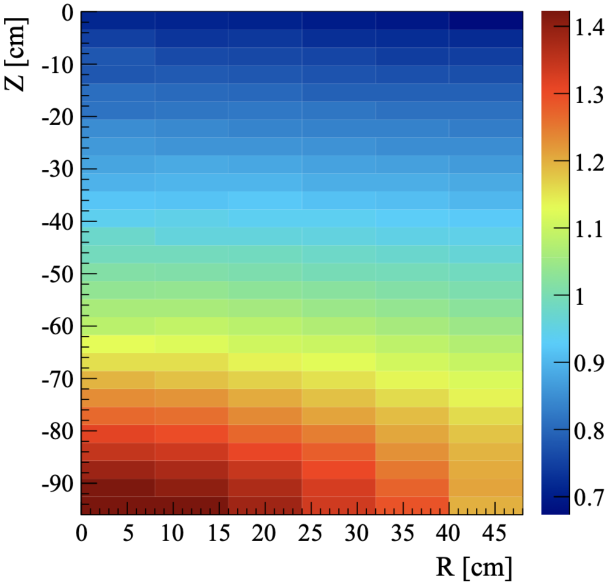

Figure 3.2: Map of the relative light collection efficiency in the XENON1T detector, in depth (Z) versus radius (R), from [54].

the distortion effects in the TPC and allow to correct for it and also construct light collection efficiency maps as illustrated in Figure 3.2. These maps enter in the correction of the S1 and S2 signals together with the maps of light detection efficiency that describe the inhomogeneity of the response of the PMT arrays shown in Figure 3.3.

3.1.5 Backgrounds

Sources that can create ER or NR signals in the detector besides the WIMP interactions are diverse and are related either to intrinsic radioactivity from the detector materials or diffused contaminants in liquid xenon, or to physical processes outside the detector.

The main background rate in the detector comes from ER sources. The ER events can be discriminated to a fair degree from NR events due to their different signature in the S1-S2 spectrum, however the lower tail of the ER distribution is the dominant component of the background for NR searches in the central volume of the TPC.

The main contribution to the ER background comes from ^{222}Rn decay chain spectrum. ^{222}Rn is a contaminant that is emanated into the liquid xenon coming from the ^{238}U present in traces in the stainless steel of the cryostat, pipes and other detector parts. Another important contribution comes from the β-

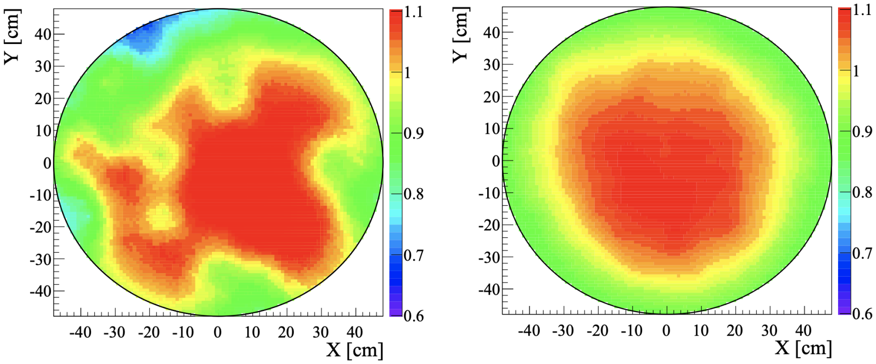

Figure 3.3: Maps of the relative light detection efficiency of S2 signals in the top (left panel) and bottom (right panel) arrays for the XENON1T detector. Figure from [54].

Source	$\frac{\text{rate}}{t\times y}$	Type	Spatial Distribution
^{222}Rn	620	ER	Intrinsic
^{85}Kr (0.36 ppt)	56	ER	Intrinsic
pp- and ^{7}Be-ν	36	ER	Intrinsic
Material radioactivity	30	ER	From edges
^{136}Xe 2-β decay	9	ER	Intrinsic
CEνES	0.55	NR	Intrinsic
Radiogenic neutrons	0.55	NR	From edges
μ-generated neutrons	<0.01	NR	From outside detetector, through muon veto

Table 3.1: Table summarising the XENON1T background sources with their expectation values, estimated through material radiation measurements and Monte Carlo simulation, from [54].

decay of ^{85}Kr, diffused in the liquid xenon naturally. During SR0 a krypton distillation campaign was carried out, reducing the ^{85}Kr concentration relative to xenon from 60×10^{-12} to $(0.66 \pm 0.11) \times 10^{-12}$ [63].

Material radioactivity from the walls of the detector produce ER events as well, however the self-shielding property of liquid xenon allows to select a central volume where this background is strongly attenuated. Other ER sources are the irreducible neutrino interactions, in particular solar proton-proton ($pp - \nu$) and ^{7}Be neutrinos. Recently, a $\sim 3\sigma$ excess has been observed in the low energy ER band, which for NR analyses could signify a new background source. This unexpected excess could mean either a BSM signal or possible tritium traces in the liquid xenon [66].

NR events can be caused by either neutrons or neutrinos that interact coherently with the nucleus. Coherently enhanced neutrino scattering (CEνNS) is an irreducible and indistinguishable signal from low mass WIMPs, possibly being uniformly distributed in the detector volume and with identical signature in the S1-S2 space. Neutrons however usually cause multiple scatters in the detector and originate mostly from the radioactive decays in the detector materials. With data quality cuts and fiducial volume selection, their contribution can be reduced.

In Table 3.1 the various background sources for XENON1T and their expected rate from Monte Carlo simulations and material radioactivity measurements are shown [54].

3.2 Xenon recoil energy spectra for ChEFT

Using the ChEFT framework and the tools provided in Ref.[45], it is possible to compute the nuclear response of xenon isotopes in nuclear recoil searches in experiments such as XENON1T [67].

One interesting possibility is that of choosing the Wilson coefficients and study the contributions of the single channels of interaction to the nuclear recoil. More specifically, it is possible to turn on one Wilson coefficient at a time that describes the quark/gluon couplings, generate the corresponding nucleon and pion matrix elements and obtain the response that includes all channels to which the chosen coefficient contributes to.

For this work we choose to study the coupling to light quarks i.e. *up*, *down* and *strange*, and gluons by isolating the individual contribution of the Wilson coefficients in Eq. 2.13, with the exclusion of the Axial-vector−Axial-vector channel, which does not have a coherently enhanced response as previously stated. In this analysis we include the dimension-five Dipole couplings, the dimension-six Vector-Vector ($VV_{u,d,s}$), Axial-vector−Vector ($AV_{u,d}$) and Tensor ($TT_{u,d,s}$ and $\tilde{T}T_{u,d,s}$) couplings, the dimension-seven Scalar-Scalar

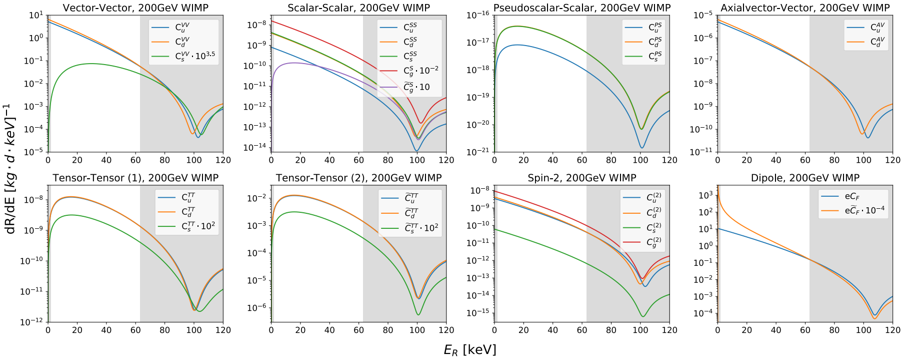

Figure 3.4: Differential rate versus recoil energy spectra of a 200 GeV/c^2 WIMP arising from the isolated contributions of the Wilson coefficients in Eq.2.13. From left to right in the top row we show the spectra for the Vector-Vector, $VV_{u,d,s}$, Scalar-Scalar, $SS_{u,d,s}$, ,S_g and $\tilde{S}_g$, Pseudoscalar-Scalar, $PS_{u,d,s}$, Axial-vector−Vector, $AV_{u,d}$ couplings, and on the bottom row, the Tensor $TT_{u,d,s}$ and $\tilde{TT}_{u,d,s}$, Spin-2$_{u,d,s,g}$ and magnetic (eC_F) and electric ($e\tilde{C}_F$) dipole couplings. Some of the spectra are scaled by a constant, indicated in the legend of the plots, for esthetical reasons. The non-shaded area of the plots shows the energy region with acceptance above 10%.

($SS_{u,d,s}$, S_g and $\tilde{S}_g$) and Pseudoscalar-Scalar ($PS_{u,d,s}$) couplings, and the dimension-eight Spin-2 ($_{u,d,s,g}$) couplings, for a total of 25 different Wilson coefficients.
In order to produce the differential recoil rate spectra in the XENON1T detector we combine the nuclear response of the natural xenon isotopes arising from each channel with the astrophysical parameters discussed in Sec.1.2 and mediate the rate over the xenon isotope abundance. In Figure 3.4 we show the 25 different recoil spectra expected from a 200 GeV/c^2 WIMP grouped by the type of interaction they arise from.
The spectra were produced by setting for each coupling the specific Wilson coefficient $C^i = 1$ and the scale $\Lambda = 1000$ GeV.

3.3 Signal and Background modelling

The background and the signal of XENON1T are modelled as probability density functions (PDFs) in cS1, cS2 and r^2 analysis space. Since some background components and expected NR signals arise from energy deposition in the liquid xenon according to well known processes, the detector response model for them is constructed by fitting data from ER and NR calibration sources in dedicated calibration campaigns, throughout the data taking of the detector. Other backgrounds, such as accidental coincidence (AC) or surface events, are modelled through data-driven methods using sidebands in energy or position.

The detector response in the case of ER or NR is modelled according to the xenon emission model described in Sec.3.1.3, in combination with the detector efficiencies and the event reconstruction uncertainties [63].

All the parameters of the microphysics of the emission model are used in a Bayesian binned likelihood fit to ER and NR calibration data obtained respectively with ^{220}Rn and with a ^{241}AmBe neutron generator. The Bayesian binned likelihood fit is performed using a band fitting framework (BBF) developed within the XENON collaboration for simulation-based modelling of the signal response in the detector and includes all the detector characteristics, the microphysics involved in the processes, and their respective uncertainties. The result of this fit is used to create the event distribution given a recoil energy spectrum and the background templates used in the analysis.

3.3.1 Analysis region and background models

For this analysis we extend the region of interest (ROI) with respect to the SI [53] and SD [68] searches up to 100 PE in cS1, while we keep the same FV of 1.3t and analysis choices. This increase in analysis space directly translates into an energy range increase of around 25%. In terms of signal acceptance, for the "bumpy" interaction channels, such as Pseudoscalar-Scalar (PS), Tensor (TT and $\tilde{T}T$) and Vector-Vector$_s$ (VV_s), in the case of high mass WIMPs ($\geq$ 100GeV/c^2) it gives an increase up to 30%. In Figure 3.5 we show the efficiency curve in the nuclear recoil energy space over the recoil spectra of the VV_d and VV$_s$ channels, showing the increased acceptance for the "bumpy" VV$_s$ spectrum.

For the background this extension does not add new background components and the well studied models for the main SI analysis can be used without additional modelling efforts.

In the new region the energy dependent backgrounds such as surface events and radiogenic neutrons contribute less and the ER band separates more from the NR band. In Table 3.2 the background best fit expectation numbers are shown and compared to the standard SI analysis, while in Figure 3.6 we show the nominal background templates used in the analysis.

ER background

The ER background consists of electronic recoils (ER) events induced from radioactive contaminants in the detector. This is the main background for NR searches in terms of event rate in the central active volume of the detector. The background can be discriminated from NR in the S1-S2 space, however due

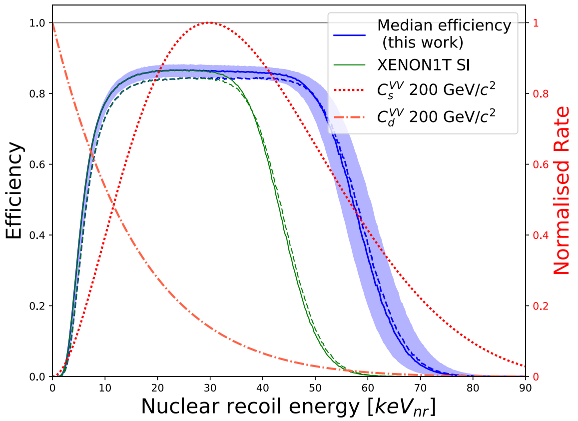

Figure 3.5: Median XENON1T detector efficiency in nuclear recoil energy for the ChEFT analysis (blue) for SR0 (dashed blue line) and SR1 (solid blue line) with the 1σ uncertainty band (blue band). The dashed and solid green lines indicate the median efficiency for the XENON1T SI analysis for SR0 and SR1 respectively. In red we illustrate for reference the spectra for the EFT VV$_d$ (dash-dotted line) and the VV$_s$ (dotted line) channels for a 200 GeV/c^2 WIMP. Figure adapted from [PAPER I].

Background	Model	Expectation SI $[(t \times y)^{-1}]$	Expectation C.A. $[(t \times y)^{-1}]$
ER	ER detector response	627 ± 18	891 ± 22
Neutron	NR + GEANT-4	1.43 ± 0.66	1.55 ± 0.71
CEνNS	NR model	0.05 ± 0.01	0.05 ± 0.02
AC	Data-driven	$0.47^{+0.27}_{-0.00}$	$0.51^{+0.28}_{-0.00}$
Surface	Data-driven	106 ± 8	133 ± 12

Table 3.2: The XENON1T background model components in the science data with the best fit expectation for the SI region and the extended region for the ChEFT analysis.

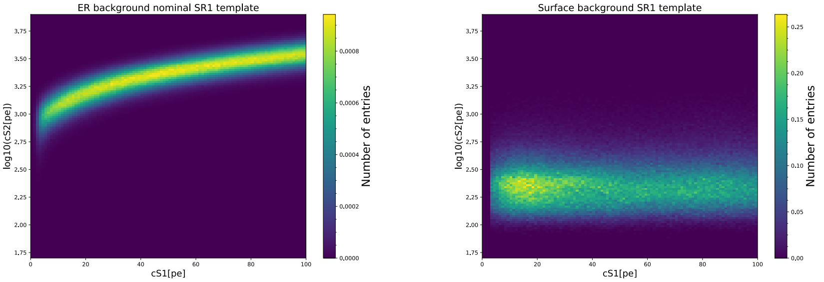

(a) ER **(b)** Surface

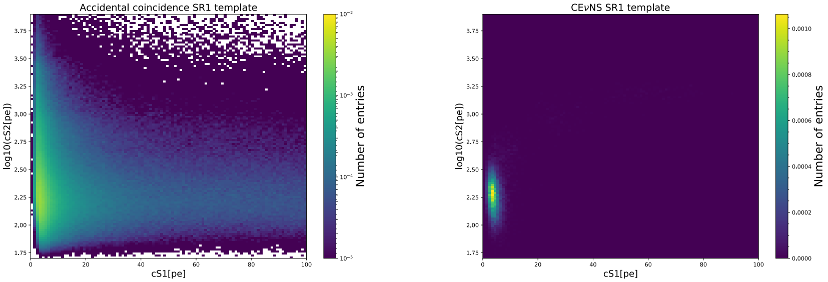

(c) AC **(d)** CEνNS

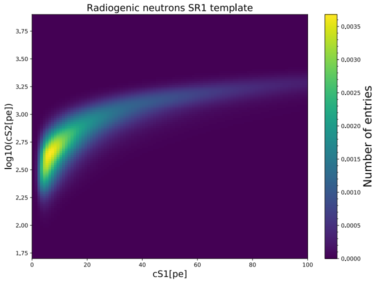

(e) Radiogenic neutrons

Figure 3.6: Two-dimensional histograms of the background models used in the analysis of the science run 1 (SR1) science data in $\log_{10}$(cS2) versus cS1. Panel (a) shows the ER normalised template, with the nominal values for the photon yield and recombination fluctuation parameters. Panel (b) shows the surface background, with the colour map normalised to the total expected number of events. Panel (c) shows the AC normalised background with the colour map in logarithmic scale. Panel (d) shows the CEνNS background normalised to the total expected number of events. Panel (e) shows the radiogenic neutrons NR background normalised to the total expected number of events.

to the extension of the lower tail in S2, the ER band can overlap with the NR band. Thus an extensive modeling of the ER background is needed. The main contributors to this background are ^{222}Rn and ^{85}Kr [60].

The two main uncertainties of the ER modelled for this search are, as in Ref.[60], the combination of the uncertainties related to the photon yield parameters and those of the recombination fluctuation effects. The photon yield term affects the mean of the ER distribution, possibly shifting it towards higher or lower S2, as illustrated in Figure 3.8, while the recombination fluctuation uncertainty affects the tails of the ER band in S2.

A third shape component is the mismodelling safeguard term, which modifies the NR-like tail of the distribution and depends on the WIMP mass or NR signal shape [69, 70].

Nuclear recoil backgrounds

There are two background components that are expected to produce NR: radiogenic neutrons and coherently enhanced neutrino-nucleus scattering events (CEνNS).

The neutrons that can interact in the active volume of the detector are produced by radioactive decays of heavy element impurities present in the materials of the cryostat and the TPC. An additional component could be muon-induced neutrons however their rate is estimated to be negligible.

The typical neutron induced signals are multiple scatterings, which are easily identifiable in the data and can be rejected. The single scatter rate can be constrained based on the identified double scatter rate and simulations. An additional component is also added to the neutron spectrum, corresponding to so called neutron-X events, in which the multiple scattering neutrons scatter at least once in regions of the detector insensitive to the charge.

The CEνNS for NR searches is an irreducible background. In our case it is conscripted in a very limited region of the S1-S2 space, corresponding to low energy NR. For this search the expected rate of solar neutrino induced CEνNS is 0.05 ± 0.02 events/$(tonne \times year)$.

Surface background

The main data-driven model for a background component is the surface background. As the name suggests, close to the surfaces of the detector radioactive contaminants, such as ^{220}Rn daughters, can accumulate from previous exposure to air. The radiation induced signals are prevalently ER and α radiation, however due to the proximity to the edge of the TPC, the event and position reconstruction are rather challenging. Furthermore charge accumulation along the walls of the TPC can also happen, which modifies the S2 of the events.

Events that originate at high radii in the detector are thus modelled as a separate background based on event samples of sidebands.
As observed in Figure3.6b, the events of the surface background concentrate at low cS2 due to the loss of charge on the TPC walls. Surface events extend up to high cS1, however with a decreasing rate, maintaining a low charge yield and overlapping with the NR signals only at very low energies.

AC background

The AC background is, as the name suggests, an accidental pairing of unrelated lone S1 and lone S2 signals into single events. To estimate the contribution of this background a sampling of the lone S1 and S2 populations was used randomly pairing them. The model distribution was then constructed in the analysis coordinates with a kernel density estimation (KDE) accounting for the expected rate of accidental pairings. While the AC events can happen in most of the cS1-cS2 space, the vast majority of them are expected at low cS1, since low energy interactions might produce an S1 signal but not an S2.

3.3.2 Signal templates

Using the recoil spectra in Sec. 3.2 and the result of the combined fit with BBF, we obtain the expected NR signal distributions in the analysis space.
The distribution of signal events will vary according to both WIMP mass and spectral shape of the operator. Low mass WIMPs will produce events concentrated in the low energy and low cS1 region of the NR band due to the kinetic cutoff of Eq. 2.1, while high mass WIMPs will produce signals distributed in the NR band according to the energy spectrum. High mass WIMPs that interact through a channel with a "bumpy" response are expected to show this feature with a distribution that has a maximum towards the centre of the NR band. In Figure 3.7 we show different signal templates arising from different interaction channels with two different WIMP masses.

3.4 XENON1T likelihood and inference

The goal of this analysis would be to infer if an observable signal-like excess is seen in the data and place confidence intervals on the coupling constants of the different interaction channels considered.
Even if the physics goal is slightly different from that of the main SI analysis, we can use most of the same inference procedure described in detail in Ref.[69].

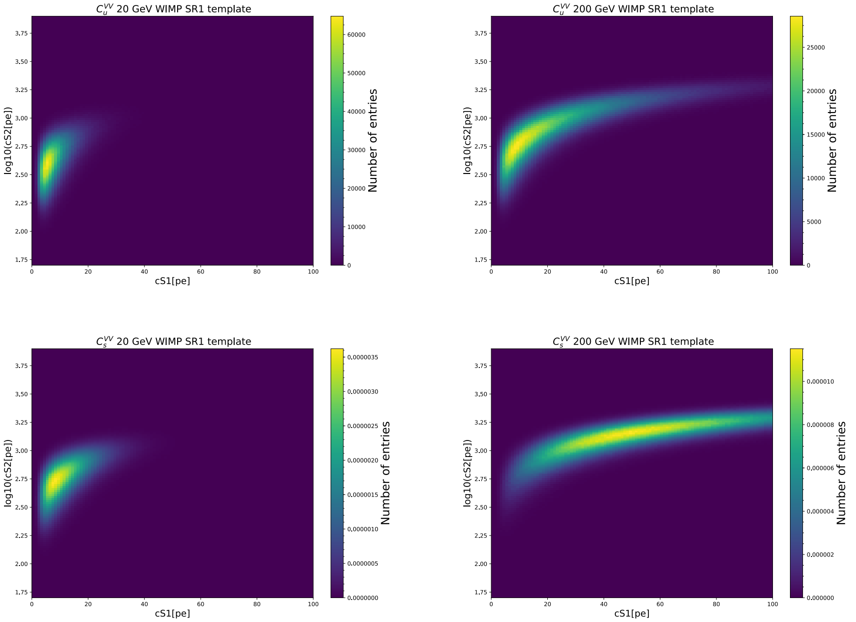

Figure 3.7: Signal model 2D templates in the analysis coordinates of $\log_{10}$(cS2) versus cS1 obtained from the differential rate of the Vector-Vector$_u$ coupling (upper panels) and Vector-Vector$_s$ coupling (lower panels) for a 20 GeV/c^2 WIMP(left side) and a 200 GeV/c^2 WIMP (right side). The colour map is normalised to the reference expected number of events for each respective coupling, with $C_u^{VV} = 1$ and $C_s^{VV} = 1$ and $\Lambda = 1000\,\text{GeV}$.

The reason why we can use most of the tools used in Ref.[53] is that the Wilson coefficients we are trying to constrain enter directly in the response calculation used to compute the cross section with xenon nuclei according to the proportionality

$$\sigma_{\chi n}^{(i)} \propto |c^{(i)}|^2 \propto \left| \frac{C^i}{\Lambda^{d-4}} \right|^2 , \tag{3.9}$$

where $c^{(i)}$ are the coupling coefficients of Eq.2.12 dependent on the Wilson coefficients C^i in Eq. 2.13, with d being the dimension of the ChEFT operator. The inference framework had to be a bit modified to accommodate the large amount of different signal models, and some inference choices that will be described later were different because of the added computational difficulty.

3.4.1 XENON1T likelihood

For this study, we use the same likelihood as in the standard SI analysis. The full likelihood is a combination of two science runs (SR), or data-sets, SR0 and SR1 where the detector was running with slightly different conditions, including also likelihood terms of calibration or ancillary measurements in order to constrain background nuisance parameters.

The XENON1T likelihood is defined as an unbinned log-likelihood function built with backgrounds and signal model defined in the analysis space of cS1, $\log_{10}$(cS2) and r^2. The science likelihood component can be written as

$$\begin{aligned}\mathcal{L}_{SR}(s, M, \boldsymbol{\theta} | \mathbf{x}_{SR}) =& \mathrm{Pois}(N_{SR} | \mu_{tot\,SR}(\boldsymbol{\theta})) \cdot \\ & \prod_{i=1}^{N_{SR}} \left(\sum_{\text{source}} \left[\frac{\mu_{SR\,\text{source}}(\boldsymbol{\theta})}{\mu_{tot\,SR}(\boldsymbol{\theta})} \cdot f_{SR\,\text{source}}(\mathbf{x}_{SR,i} | \boldsymbol{\theta}) \right] \right) .\end{aligned} \tag{3.10}$$

Where:

- the subscript SR stands for the science data-set, SR0 or SR1,
- s is the signal rate multiplier which corresponds to the quantity

  $$\left| \left(\frac{C^i}{\Lambda^{d-4}} \right)_{\text{inferred}} \cdot \Lambda_{\text{ref}}^{d-4} \right|^2$$

  which is effectively the inferred Wilson coefficient divided by the scale Λ, multiplied by the reference $\Lambda_{\text{ref}} = 1000$ GeV,
- M is the WIMP mass in GeV/c^2
- $\boldsymbol{\theta}$ are all the nuisance parameters of the model,

- $\mathbf{x}_{SR}$ are all the event coordinates defined in the analysis space,
- N_{SR} is the number of events in the corresponding data-set,
- the index 'source' runs over all the background and signal models,
- $\mu_{SR\,\text{source}}(\boldsymbol{\theta})$ and $\mu_{tot\,SR}(\boldsymbol{\theta})$ are the expectation values of each source and the total expectation value ($\equiv \sum_{\text{source}} \mu_{SR\,\text{source}}(\boldsymbol{\theta})$) respectively,
- $f_{SR\,\text{source}}(\mathbf{x}_{SR,i}|\boldsymbol{\theta})$ is the probability density function (PDF) of a source for event i at the respective coordinates $\mathbf{x}$, given the nuisance parameters $\boldsymbol{\theta}$.

The calibration likelihood components are written in a similar way:

$$\begin{aligned}\mathcal{L}_{CR}(M,\boldsymbol{\theta}|\mathbf{x}_{CR}) =&\text{Pois}(N_{CR}|\mu_{tot\,CR}(\boldsymbol{\theta}))\cdot \\ &\prod_{i=1}^{N_{CR}}\left(\sum_{\text{source}}\left[\frac{\mu_{CR\,\text{source}}(\boldsymbol{\theta})}{\mu_{tot\,CR}(\boldsymbol{\theta})}\cdot g_{CR\,\text{source}}(\mathbf{x}_{SR,i}|\boldsymbol{\theta})\right]\right),\end{aligned} \tag{3.11}$$

but in this case the CR subscript indicates the specific calibration data-sets used to constrain SR0 or SR1 nuisance parameters. $\mu_{CR\,\text{source}}(\boldsymbol{\theta})$ and $\mu_{tot\,CR}(\boldsymbol{\theta})$ are the specific source expectation value and total expectation value respectively and $g_{CR\,\text{source}}(\mathbf{x}_{SR,i}|\boldsymbol{\theta})$ is analogous to the PDF term in Eq. 3.10. The likelihood, even if it is not depending on the signal rate multiplier, it still depends on the signal shape (and WIMP mass), due to the mismodelling term in the ER model.

Other ancillary measurements also constrain the rates of the CEνNS, radiogenic and AC backgrounds. The CEνNS and radiogenic likelihoods are given by a Gaussian constrained by the measurement of the expectation value and can be written as

$$\mathcal{L}_{\text{source}\,SR}(\boldsymbol{\theta}) = \text{Gaus}(\hat{\mu}_{\text{source}\,SR}|\mu_{\text{source}\,SR},\sigma_{\text{source}\,SR}) \tag{3.12}$$

where $\hat{\mu}_{\text{source}\,SR}$ is the measured expectation value, and $\mu_{\text{source}\,SR}$ and $\sigma_{\text{source}\,SR}$ are respectively the expectation value and measurement uncertainty parameters. The radiogenic likelihood is assumed correlated between runs and thus shared between SR0 and SR1.

The AC likelihood term is built as a uniform distribution between a minimum and a maximum expectation value [53], thus can be written as

$$\mathcal{L}_{AC\,SR} = \text{Uniform}(\mu_{AC\,SR}|\hat{\mu}^{min}_{AC\,SR},\hat{\mu}^{max}_{AC\,SR}). \tag{3.13}$$

This expression describes the constraint of the AC rate multiplier given the AC background template and does not depend on any shape parameter.

The total likelihood is the product, for each science data-set, of all the background likelihood components and the science likelihood and can be written as

$$\mathcal{L}_{\text{total}}(s, M, \boldsymbol{\theta}) = \mathcal{L}_{SR0}(s, M, \boldsymbol{\theta}) \cdot \mathcal{L}_{SR1}(s, M, \boldsymbol{\theta}) \cdot \mathcal{L}_{\text{radiogenic}}(\boldsymbol{\theta}) \tag{3.14}$$

where the radiogenic part is shared between science runs.
This results in 24 different parameters in the likelihood: 13 rate parameters for the background, divided in 6 rate parameters for each science run for each calibration run and background source, plus the radiogenic rate parameter; seven background shape parameters that include the recombination fluctuation, photon yield, mismodelling and the surface shape parameters; two signal efficiency parameters for the two science runs, the WIMP mass, fixed for each fit, and the signal rate multiplier. All the rate parameters are bound to have only non negative values, including the signal rate multiplier.

3.4.2 Inference procedure

As previously anticipated the inference for this analysis is done, for each operator, for a single WIMP mass hypothesis at a time. In an analogous way to the main SI analysis, we use a profile log-likelihood ratio as a test statistic, which means that we set the nuisance parameters to the values that maximise the likelihood given the signal strength and subtract the best-fit obtaining

$$\lambda(s|M) = -\log\left(\frac{\mathcal{L}_{\text{tot}}(s, M, \hat{\hat{\boldsymbol{\theta}}})}{\mathcal{L}_{\text{tot}}(\hat{s}, M, \hat{\boldsymbol{\theta}})}\right), \tag{3.15}$$

where the total likelihood is defined in Eq. 3.14. In Eq. 3.15 the $\hat{\hat{\boldsymbol{\theta}}}$ indicates the parameters that maximise the likelihood at fixed signal, and $\hat{s}$ and $\hat{\boldsymbol{\theta}}$ indicate global best fit parameters of the likelihood.
In order for us to obtain the local significance of possible excesses and build confidence intervals we require the distribution of the test statistic $\lambda(s|M)$ given that s is the true signal. In the main SI analysis a full profile construction was used, estimating through Monte Carlo (MC) simulations the distribution of $\lambda(s|M)$. This was done to overcome the under-coverage observed in the first XENON1T result [71]. The estimation of the $\lambda(s|M)$ distribution however is very computationally expensive, requiring $\mathcal{O}(100000)$ toyMC simulations for a total of $\sim$ 400h of computation time even with parallel jobs on the Midway computing cluster of the University of Chicago Research Computing Center. For this analysis, since we are analysing 25 different signal models, such computation would require up to 25 times the SI computation time to be completed. Thus we settle for an asymptotic treatment of the test statistic

distribution, limiting the search in the low mass WIMP region to a minimum of 10GeV/c^2 , where all operators would give an observable signal, and above which the discrepancy between the full profile construction and the asymptotic distribution of the test statistic becomes smaller. To ensure that no dramatic undercoverage is present we checked the coverage of the results for each mass.

Asymptotic inference and power constraint

According to Wilks' theorem, the distribution of the log-likelihood ratio $2 \cdot \lambda$ will approach a χ^2-distribution in the limit of large number of samples [72, 73]. While it has been shown that for low WIMP masses the XENON1T experiment is not in this regime [69], the approximation holds for WIMP masses above 50-70 GeV/c^2 .

For this analysis we use a two-sided Neyman construction with the addition that we impose a threshold of 3σ, where with σ is intended the equivalent number of standard deviation of the normal distribution as $\sigma(p) = \Phi^{-1}(1-p)$, where Φ^{-1} indicates the inverse cumulative density function (CDF) of a standard Gaussian ($\mu = 0$ and $\sigma = 1$) and p is the p-value inferred, below which we will only report the upper edge of the confidence interval, i.e. only setting an upper limit. The confidence interval is computed as per definition of the Neyman construction according to

$$1 - \alpha = \int_{a(s)}^{b(s)} f(x|s)\mathrm{d}s \tag{3.16}$$

where a and b are boundaries such that the confidence interval $1-\alpha$ for s given a measured value x_0 becomes $[b^{-1}(x_0), a^{-1}(x_0)]$.

Since we are using the asymptotic function of the likelihood ratio distribution, the interval coverage is not assured, thus we have to explicitly verify that the coverage is maintained (see Sec. 3.4.3).

For the limit setting we will also use the power-constrained limit (PCL) method [74], with a threshold on the signal size by setting a minimal discovery power of 15%, as in the main SI result. The limits for the ChEFT results are reported in [PAPER I] and Section 3.5.

Computational framework

The likelihood construction is implemented using *blueice*[1], which is a public inference package that computes and profiles likelihoods. This code was modified with scripts to accommodate the use of different signal models, and to

---

[1] `https://github.com/JelleAalbers/blueice`, by Jelle Aalbers

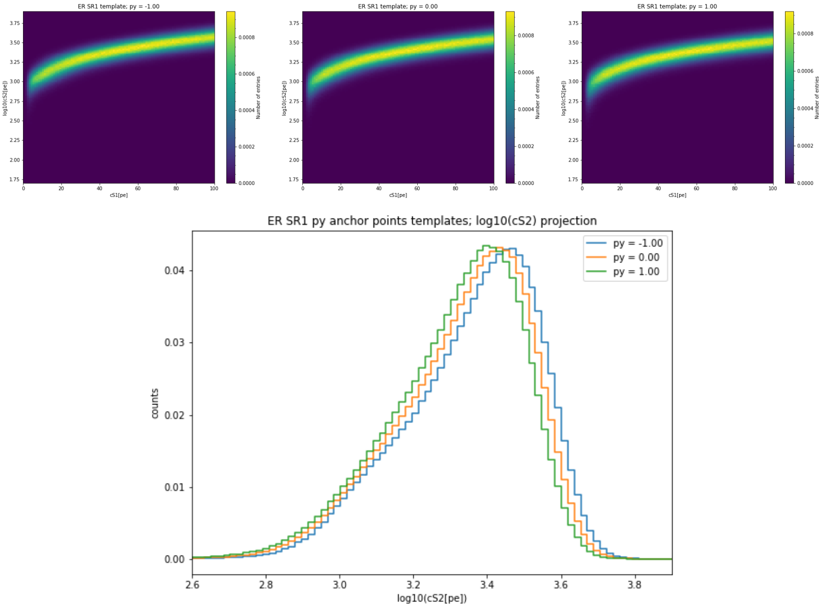

Figure 3.8: The upper panels show the 2D templates in $\log_{10}$(cS2) versus cS1 for three values of the ER photon yield (labeled *py* in the plots) shape parameters for SR1, respectively -1σ, nominal, and $+1\sigma$, while the lower panel shows a projection on the $\log_{10}$(cS2) axis of the templates where the effect of mean-shift of the distribution due to the variation of the *py* parameter is better illustrated. The orange line shows the histogram relative to the nominal value of *py*, while the blue and the green show respectively the $py = -1\sigma$ and $py = +1\sigma$.

add modularity for possible extensions of the total likelihood.

In this *blueice*-based inference the parameters are treated as either rate parameters, where they are just a scale of the expectation value for the single sources, or as shape parameters that influence the shape of the PDFs in the analysis coordinates.

In the case of shape parameters an interpolation of the PDFs is done across 'anchor points' in the nuisance parameters, a method better known as *template morphing*. In Figure 3.8 we show an example of three anchor points templates for the photon yield ER shape parameter.

3.4.3 Validation of the inference

In order to validate the inference results and check the stability of the framework we performed fits to a number of toy Monte Carlo (toy-MC) data-sets. In these tests we validated the best-fits through pull plots and we verified the coverage for each signal model.

Pull-plots

The investigation and validation of the likelihood fits required us to simulate a large number (~ 20000) of toy-MC data-sets where all the nuisance parameters of the likelihood were varied. Each toy data-set was then fitted and the best-fit values and simulation values of the parameters were stored. In figures 3.9 and 3.10 we show the two-dimensional histograms of the distribution of the best-fit parameters for given true i.e set in the simulation of the toy data-set, parameters. On average all the parameters seem to fit the true value.
The distribution of the best-fit parameters for given true parameter serves also to obtain the spread σ_θ at a given true parameter θ_0. This can be used to determine the significance of the best-fit nuisance parameter of the actual science data-sets in respect to the expectation.

Coverage

As previously stated, verifying the coverage for this analysis is crucial to ensure that the reported intervals for the results are solid. In order to do so we performed toy-MC simulations of the science and calibration data-sets together with simulated events from each signal model, for signal expectation values between 0 and 15 events. For each expectation value and each of the signal models we performed 600 toy-MCs, while for one operator, channel VV_s, we performed 2000 toy-MCs to decrease the statistical uncertainty. For these simulations the fraction of confidence intervals containing the true signal rate multiplier corresponding to the expected number of signal events simulated are stored.
In Figure 3.11 we show the coverages for different WIMP mass in the channel VV_s. These plots show that for this analysis the coverage does not seem to be a problem. At low masses for most of the signal models there is some fluctuation in the coverage, however no consistent under-coverage is observed.

Sensitivity studies

In a similar fashion as for the coverage studies, we performed 2000 toy-MC simulations for each signal model with a signal expectation value of 0 events for 14 WIMP masses between $10\text{GeV}/c^2$ and $10000\text{GeV}c^2$ and for each we computed and saved the upper limit of the signal rate multiplier. For each mass we computed then the median and the $\pm 1\sigma$ and $\pm 2\sigma$ percentiles of the upper limit distributions.
To make sure that the sensitivities computed are consistent with the detector performance and the results of the main SI analysis, we can compute instead of the upper limit of the signal rate multiplier, the upper limit of the expectation

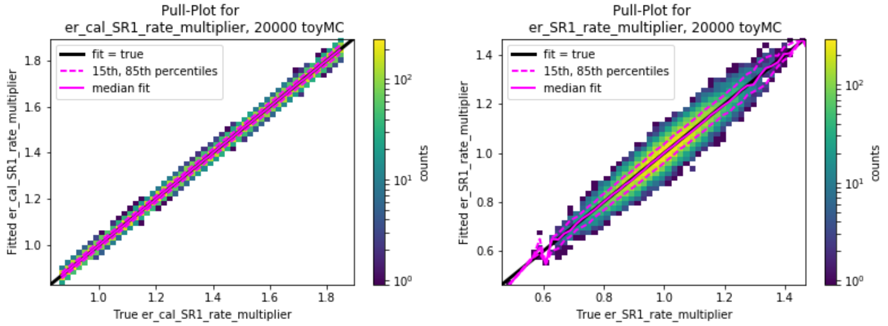

(a) SR1 ER calibration rate **(b)** SR1 ER rate multiplier

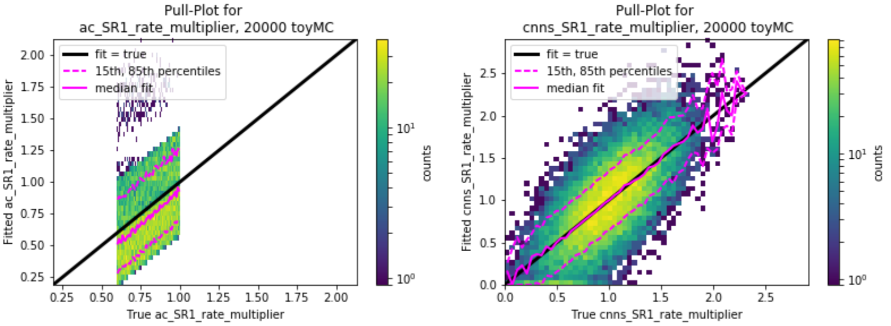

(c) SR1 AC rate multiplier **(d)** SR1 CEνNS rate multiplier

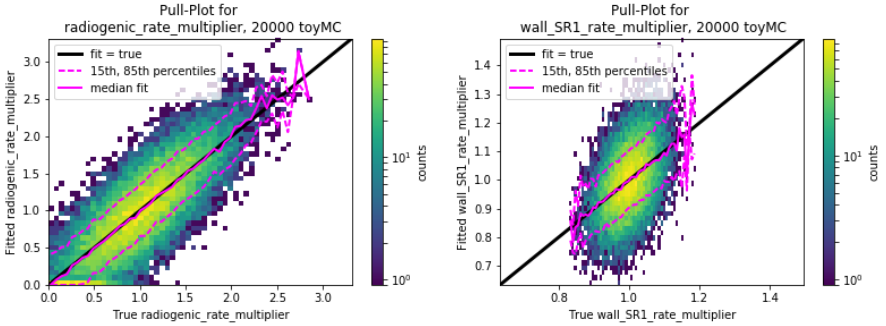

(e) SR1 radiogenic rate multiplier **(f)** SR1 surface rate multiplier

Figure 3.9: Pull plots shown as two-dimensional histograms of the best-fits of SR1 rate parameters and true parameters used in generating the toy-MC data-sets. The plots are the result of the fits of 20000 toy-MC data-sets. The black line indicates the line when the best fit is equals to the true value, the continuous magenta line is the median fit and the dashed magenta lines indicate the 15th and 85th percentiles of the fits.

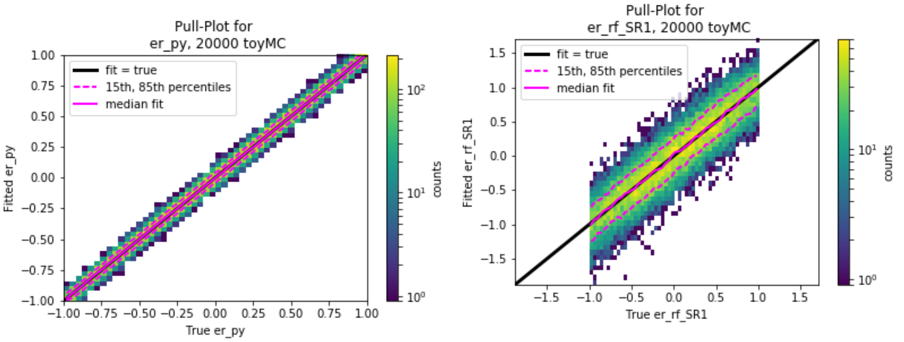

(a) ER photon yield parameter

(b) SR1 ER recombination fluctuation parameter

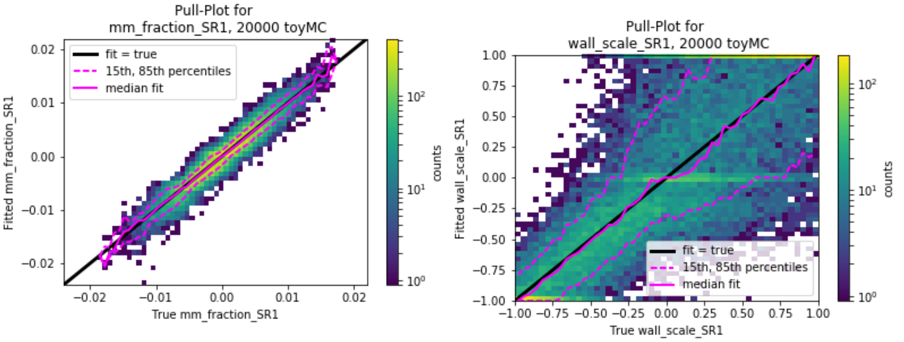

(c) SR1 mismodelling safeguard as a fraction of ER

(d) SR1 surface shape parameter

Figure 3.10: Pull plots shown as two-dimensional histograms of the best-fit SR1 shape parameters and true parameters used in generating the toy-MC data-sets. The plots are the result of the fits of 20000 toy-MC data-sets. The black line indicates the line when the best fit is equals to the true value, the continuous magenta line is the median fit and the dashed magenta lines indicate the 15th and 85th percentiles of the fits.

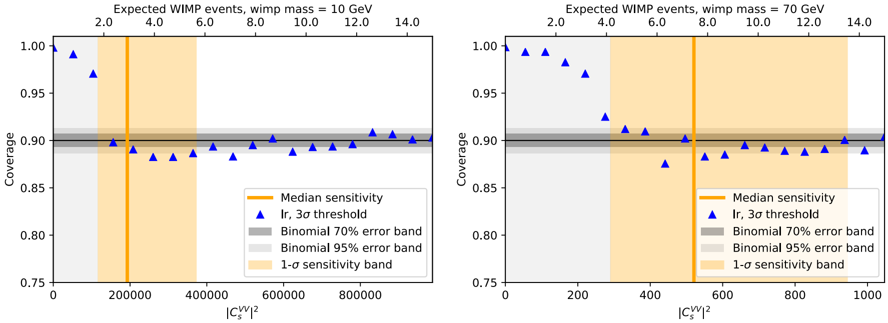

(a) Coverage for 10 GeV/c^2WIMP **(b)** Coverage for 70 GeV/c^2WIMP

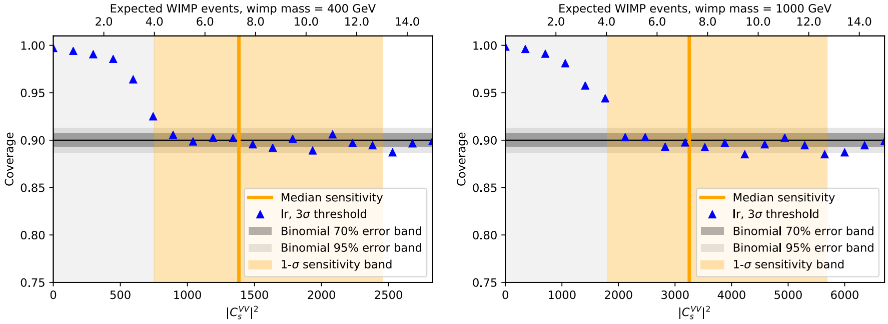

(c) Coverage for 400 GeV/c^2WIMP **(d)** Coverage for 1000 GeV/c^2WIMP

Figure 3.11: Coverage plots for different mass WIMPs in the channel VV_s for different expected WIMP events and corresponding Wilson coefficient. In blue is shown the coverage of the Wilks likelihood ratio with the 3σ threshold, the black line shows the 90% nominal coverage, the grey shaded areas are the 70% and 95% binomial error bands around the nominal coverage. The orange line and the orange shaded area are the median and 1σ band of the sensitivity. The vertical light grey band is the region where the power constraint threshold is applied.

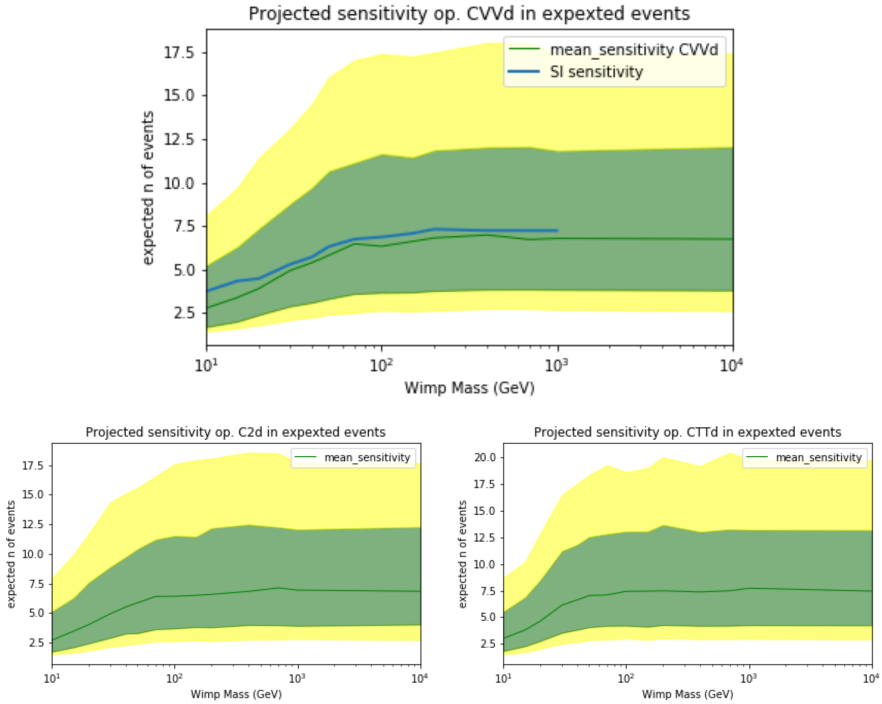
Projected sensitivity op. CVVd in expexted events

Projected sensitivity op. C2d in expexted events

Projected sensitivity op. CTTd in expexted events

Figure 3.12: Plots of the sensitivity in expected number of events versus WIMP mass. The upper panel shows a comparison between the SI sensitivity in expected events (blue line) and mean sensitivity of channel VV_d (green line) of this analysis with the 1σ (green) and 2σ (yellow) bands. Lower panels show the sensitivity in terms of expectation value of the Spin-2_d (left) and TT_d (right).

values for various WIMP masses.

In Figure 3.12 we show the sensitivity of an interaction channel the recoil spectrum of which resembles the shape of the classical SI interaction, VV_d, and we compare the sensitivity in expectation number with the classical SI spectrum explored in the analysis in Ref.[53]. The plot shows some differences for low expectation values explainable with the difference in the way we set the confidence intervals. In Ref.[53] a full profile construction with Feldman-Cousins intervals [75] is used, while we resolve to use asymptotic inference. The sensitivities in expected number of events for other operators also seem in decent agreement with the XENON1T sensitivity potential.

3.4.4 Check of low-ER excess as a background

Given the recent result of the Low ER search with XENON1T [76] which observed an excess of events around $\sim 2.3\,\text{keV}_{er}$, a posteriori, we checked for

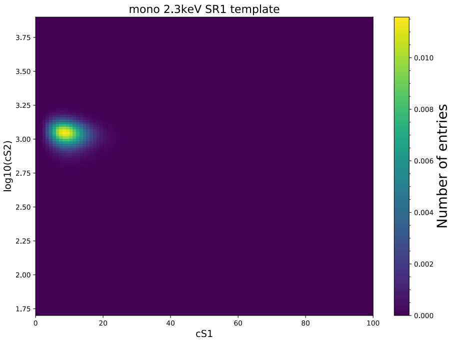

Figure 3.13: 2D histogram of the monoenergetic ER of 2.3 keV_{er} in the cS1-$\log_{10}$(cS2) space for SR1, used to test the effect on the inference of an additional ER background consistent with the Low-ER analysis in [76].

what it could mean for an NR search.

The electron excess was modelled as a monoenergetic ER signal at 2.3 keV_{er} for which we produced a template in the same fashion of the standard ER band background previously discussed. In Figure 3.13 we show the monoenergetic template for SR1 in cS1-cS2 space. This new background component was added in the science likelihood to the constant ER band, as normalised to 1 event/$(tonne \times year)$, without any of the ER shape nuisance parameters and only with a free rate parameter that can scale according to the number of events observed in this region.

The likelihood best fit for the rate parameters of the SR0 and SR1 monoenergetic ER additional background were $R^{SR0}_{2.3keV} = 0.0^{+0.5}_{-0.0}$ and $R^{SR1}_{2.3keV} = 27.0 \pm 5.5$ events respectively. The effect of the new background on the other likelihood nuisance parameters is minimal, with the only difference being the ER band rate multiplier for SR1, which decreases by $\sim 3\%$ from the nominal expectation value. The sensitivities and the limits for the various signal models are also not considerably affected by the additional background, with changes up to a maximum of $\pm 5\%$, varying according to the signal model tested.

Given the uncertain nature of this background we do not include it in the final analysis.

3.5 Results

This section describes the limit setting and the results obtained for the individual ChEFT coefficients and the limits on the scale Λ. We also discuss here the limits on some specific benchmark models where we look for the effect of isospin-breaking interactions for three different DM scenarios.

3.5.1 Data

The analysis was carried on using data from two science runs, SR0 and SR1, of the XENON1T experiment for a total exposure of 1 tonne×year. This analysis reused the data from the main nuclear recoil analysis of XENON1T [53].
In this analysis we extended the energy window, up to 100PE in cS1. After the main SI analysis, the data in the window [80,100]PE in cS1 remained blinded for the nuclear recoil band. Three additional events were observed when the data was finally unblinded. These events are consistent with the estimated acceptance loss of the ER band of 1% due to the original blinding cut.

3.5.2 Limits on individual coefficients

As previously stated, we use the profile likelihood ratio to set limits on the squared Wilson coefficient of the considered interaction channel, value which corresponds to the signal rate multiplier parameter in the likelihood:

$$s = \frac{\mu_{inf}}{\mu_{ref}} = \left|\frac{C^i}{\Lambda^{d-4}}\right|^2_{inf} \cdot \left|\frac{C^i}{\Lambda^{d-4}}\right|^{-2}_{ref} \tag{3.17}$$

where μ_{inf} is the inferred expectation value given the detector response with the respective scaled Wilson coefficient $\left|\frac{C^i}{\Lambda^{d-4}}\right|^2_{inf}$, and μ_{ref} is the signal model reference value from the spectrum obtained with $C^i_{ref} = 1$ and $\Lambda_{ref} = 1000\mathrm{GeV}$.
Another way of presenting the results that is preferred when treating EFT results is to show the limits, on the scale Λ, which is related to the mass of the interaction mediator. To compute the limit in terms of Λ, given Eq. 3.17, if we assume $C^i_{inf} = C^i_{ref} = 1$ and invert the relation, the computed limit will be:

$$\Lambda_{inf} = \frac{\Lambda_{ref}[\mathrm{GeV}]}{(\sqrt{s})^{\frac{1}{d-4}}} \tag{3.18}$$

where d is the dimension of the operator considered.
As anticipated in Chapter 2, for a set of operators we compute the limits using the recoil spectrum obtained within the ChEFT framework provided in Ref.[47] with the DirectDM software [52] and the nuclear response package DMFormFactor [77]. To harmonise the results obtained with DirectDM with the generalised SI framework, the DirectDM limits were scaled considering the different constants in the definition of the operators and their coupling amplitudes. The limits of the dipole operators were scaled by $\left[\frac{e^2}{8\pi^2}\right]^{-2}$ and the

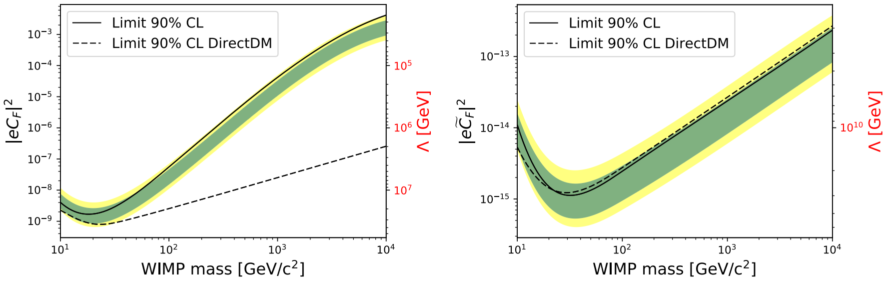

Figure 3.14: 90% confidence level limits on the magnetic (left panel) and electric dipole (right panel) Wilson coefficients of the WIMP-nucleus interactions, using the generalised SI (solid black line) and the DirectDM (dashed black line) frameworks. In green and yellow we show the 1σ and the 2σ sensitivity bands computed for the generalised SI approach. On the right side of the panels we show the corresponding limit on the scale Λ in GeV.

Scalar-gluon operators ($\mathcal{Q}_1^{(7)}$ and $\mathcal{Q}_2^{(7)}$) were scaled by $(12\pi)^{-2}$.
In Figures 3.14, 3.15, 3.16, 3.17, and 3.18 we show the limits for all 25 channels of interaction considered in the generalised SI ChEFT framework. The limits are shown for both the dimensionless Wilson coefficient squared, $(C_i)^2$, and the scale Λ in GeV.

The sensitivity bands reported in Figures 3.14, 3.15, 3.16, 3.17, and 3.18 are computed for the generalised SI framework. The biggest differences between the limits computed with the DirectDM framework (shown in dashed lines) and the generalised SI show up the magnetic dipole interaction and for the scalar channels and they are to be attributed to the different NREFT mapping discussed in Chapter 2. Other small differences can be attributed to the differences in the nuclear response.
For all the channels we computed also the discovery significance, obtaining the biggest discovery significance for the operator VV_s and a WIMP mass of $70\,\mathrm{GeV}/c^2$, with a discovery p-value of 0.044, which is below the self-imposed 3σ threshold for reporting a lower limit. In Figure 3.19 we show the plot of the discovery significance for the VV_s operator for all tested WIMP masses.

3.5.3 Benchmark models

To supplement the individual ChEFT limits, we include three benchmark models to show the effects of isospin-breaking and isospin-conserving interactions and also to address the limitations of switching on one Wilson coefficient at a time. The three benchmark models chosen are:

- the vector mediator for Majorana DM, where the vector current vanishes

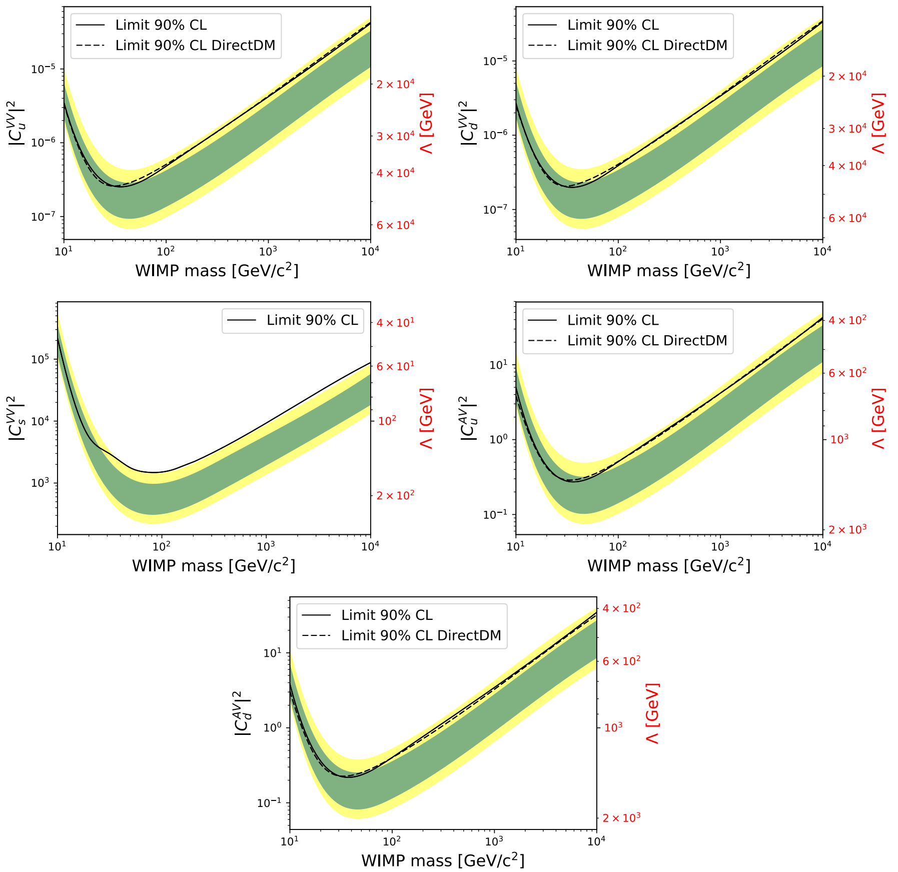

Figure 3.15: 90% confidence level limits on the Wilson coefficients of the VV and AV operators, using the generalised SI (solid black line) and the DirectDM (dashed black line) frameworks. In green and yellow we show the 1σ and the 2σ sensitivity bands computed for the generalised SI approach. On the right side of the panels we show the corresponding limit on the scale Λ in GeV.

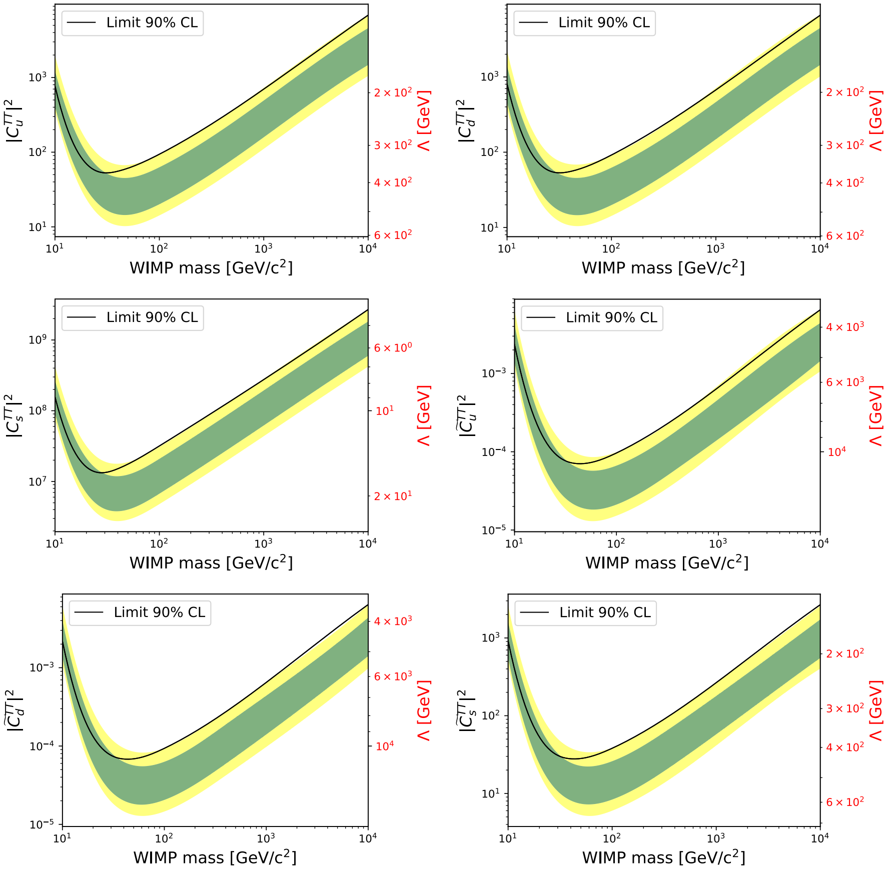

Figure 3.16: 90% confidence level limits on the Wilson coefficients of the tensor (TT and $\tilde{T}T$) operators, using the generalised SI (solid black line) framework. In green and yellow we show the 1σ and the 2σ sensitivity bands computed for the generalised SI approach. On the right side of the panels we show the corresponding limit on the scale Λ in GeV.

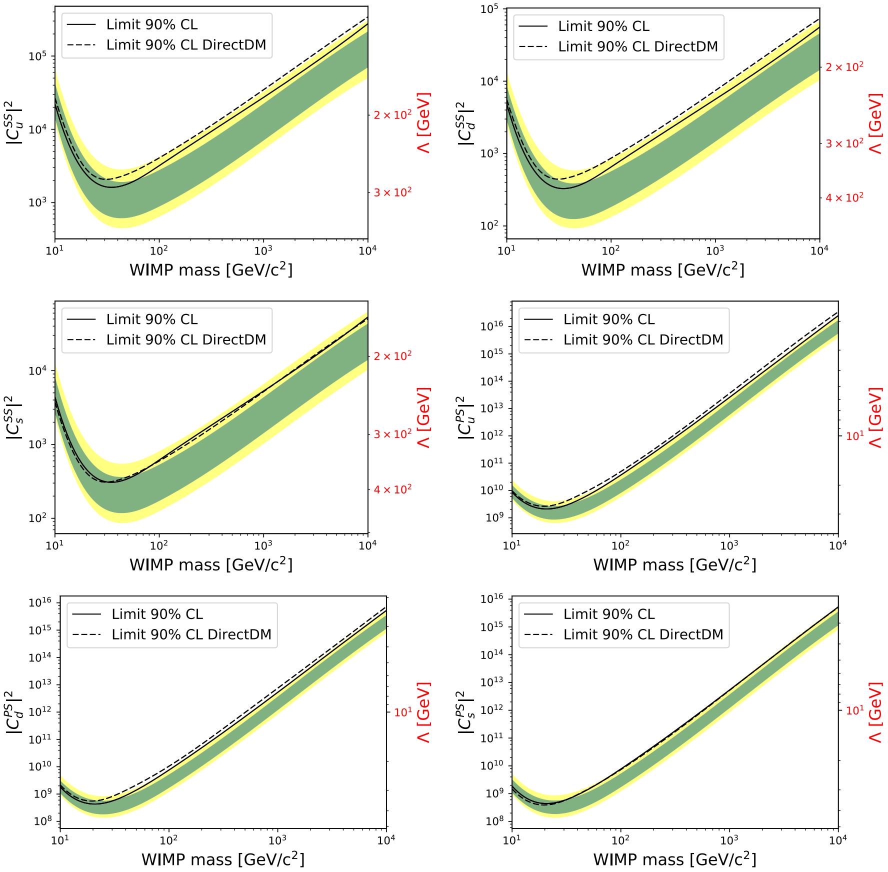

Figure 3.17: 90% confidence level limits on the Wilson coefficients of the SS and PS operators, using the generalised SI (solid black line) and the DirectDM (dashed black line) frameworks. In green and yellow we show the 1σ and the 2σ sensitivity bands computed for the generalised SI approach. On the right side of the panels we show the corresponding limit on the scale Λ in GeV.

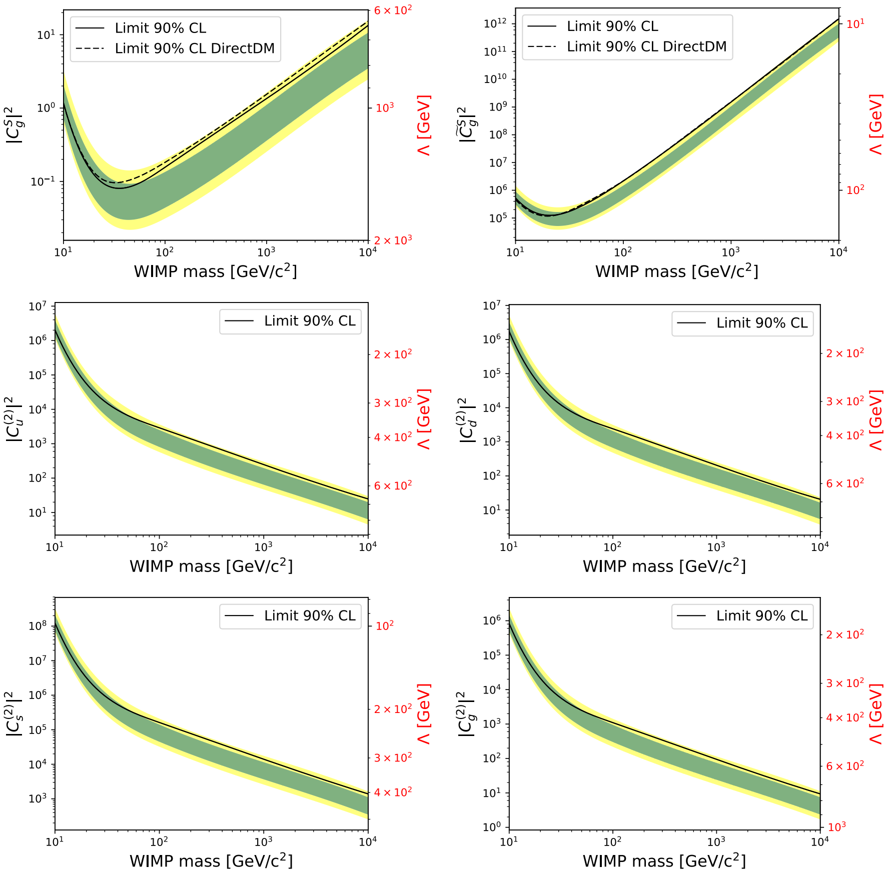

Figure 3.18: 90% confidence level limits on the Wilson coefficients of the scalar-gluon (S_g and $\tilde{S_g}$) operators (top panels), using the generalised SI (solid black line) and the DirectDM (dashed black line) frameworks, and on the dimension-8 spin-2 operators (middle and lower panels), using the generalised SI framework. In green and yellow we show the 1σ and the 2σ sensitivity bands computed for the generalised SI approach. On the right side of the panels we show the corresponding limit on the scale Λ in GeV.

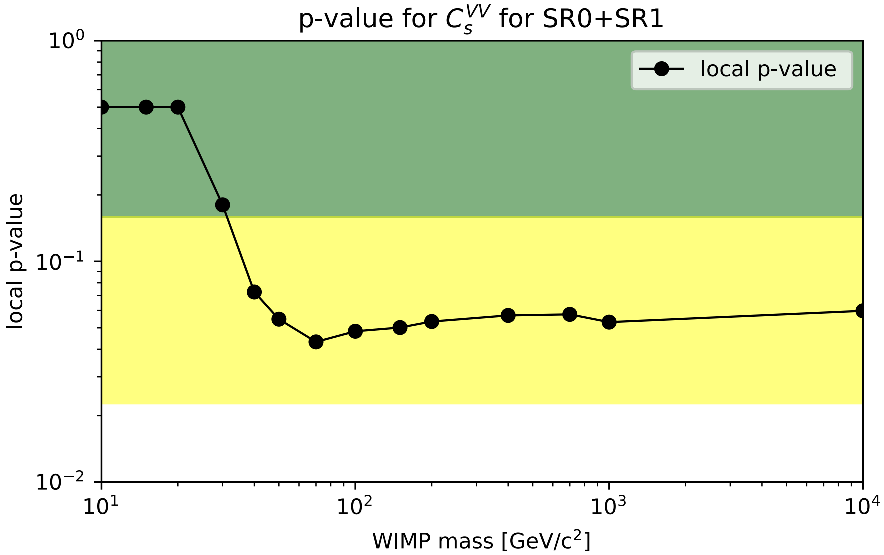

Figure 3.19: Local discovery p-value for operator with the highest obtained discovery significance, the VV_s, for all the probed masses. The lowest p-value obtained is for a $70\,\mathrm{GeV}/c^2$ WIMP, with $p = 0.044$.

and the leading term becomes the AV component, $\mathcal{L}^{AV} = \sum_q \frac{C_q^{AV}}{\Lambda^2} \bar{\chi}\gamma^\mu\gamma_5\chi\bar{q}\gamma_\mu q$,

- the vector mediator for Dirac DM, where the leading operator is VV, $\mathcal{L}^{VV} = \sum_q \frac{C_q^{VV}}{\Lambda^2} \bar{\chi}\gamma^\mu\chi\bar{q}\gamma_\mu q$,
- and the scalar mediator for fermion DM, where the leading term is SS, $\mathcal{L}^{SS} = \sum_q \frac{C_q^{SS}}{\Lambda^3} \bar{\chi}\chi m_q\bar{q}q$.

For these models we turn on the Wilson coefficients for $q = u, d$ at the same time at a set ratio, so that $C_u = rC_d$. This way the inference is still done on only one parameter, with the signal rate multiplier still corresponding to the inferred squared Wilson coefficient, according to Eq. 3.17.
The vector mediator for Majorana DM however needs a careful treatment. The $SU(2) \times U(1)$ invariant operators above the weak scale match on both AV and AA operators at the same time, thus a full treatment would need the contributions of the AA component, $\mathcal{L}^{AA} = \sum_q \frac{C_q^{AA}}{\Lambda^2} \bar{\chi}\gamma^\mu\gamma_5\chi\bar{q}\gamma_\mu\gamma_5 q$, but this addition would add also a new dimension to the problem. One possible way to maintain the inference in one parameter only while allowing isospin breaking interactions without tuning is to use the relations between the above weak scale operators and the lower energy ChEFT operators we are considering, defined

in Ref.[78]:

$$C_u^{AV} = \mathcal{C}_{7,1}^{(6)} + \mathcal{C}_{6,1}^{(6)} \tag{3.19}$$

$$C_d^{AV} = \mathcal{C}_{8,1}^{(6)} + \mathcal{C}_{6,1}^{(6)} \tag{3.20}$$

$$C_u^{AA} = \mathcal{C}_{7,1}^{(6)} - \mathcal{C}_{6,1}^{(6)} \tag{3.21}$$

$$C_d^{AA} = \mathcal{C}_{8,1}^{(6)} - \mathcal{C}_{6,1}^{(6)} \tag{3.22}$$

where C_q are the Wilson coefficients of the low energy ChEFT operators and the $\mathcal{C}^{(6)}$ are the coefficients of the above weak scale operators. These relations show us that by setting $C_u^{AA} = 0$, we obtain that we can set $C_d^{AA} = C_d^{AV} - C_u^{AV}$, and if we keep the relation $C_u^{AV} = rC_d^{AV}$ we have again a direct way to interpret the signal rate multiplier as the squared Wilson coefficient $s = (C_{d(inf)}^{AV})^2$.
We computed the spectra and the signal models for these three cases for three different WIMP masses, 50 GeV/c^2 , 200 GeV/c^2 and 1000 GeV/c^2, for various ratios between the u and d coefficients using both the generalised SI and the DirectDM frameworks. The vector mediator for Majorana DM case however was investigated with the AA contribution only with the DirectDM framework since the AA contribution is not included in the generalised SI nuclear responses.
In Figures 3.20, 3.21 and 3.22 we include the plots of the 90% CL limits on the squared Wilson coefficient against the ratio of the coefficients $r = C_u/C_d$ for the three models and the three different masses for each.

The limits show that in the cases of the vector mediator for Majorana and Dirac DM, for isospin-breaking interactions, there is an interference between the coefficients around $r \simeq -1.1$, with limits becoming up to four orders of magnitude worse. In the scalar mediator case, the cancellation happens around $r \simeq -2.2$, with the limits worsening by up to 6 orders of magnitude.
When the AA contribution is turned on in the vector mediator for Majorana DM, the interference disappears, with the limit on the coefficient becoming roughly constant.
These results show that only in the case of specific isospin-breaking interactions, in a narrow window of coupling choice, the dark matter limits set in direct detection experiments may be a few orders of magnitude worse, specifically in the case of Dirac DM and scalar-mediated fermion DM.

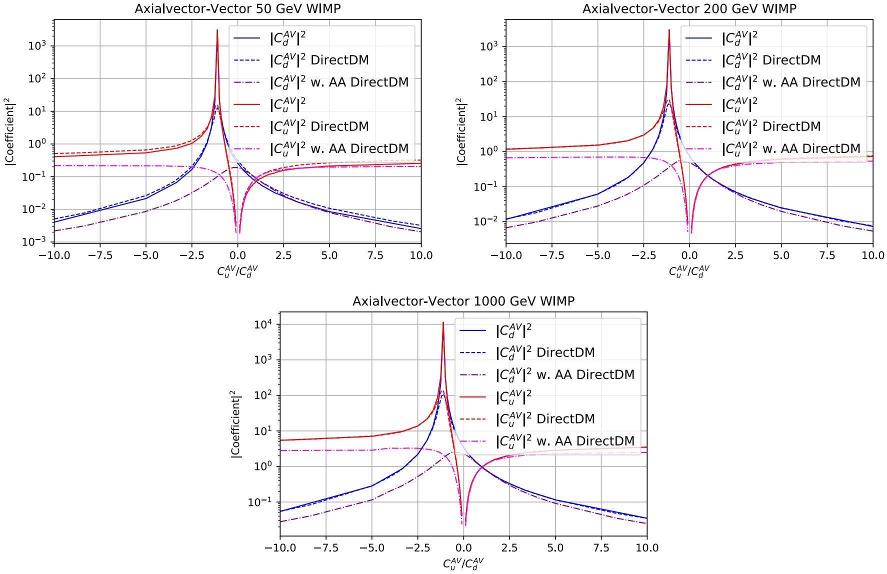

Figure 3.20: 90% confidence level upper limits on the Wilson coefficients of the vector mediated Majorana DM benchmark model of WIMP interactions for three different WIMP masses, 50 GeV/c^2 (top left), 200 GeV/c^2 (top right), and 1000 GeV/c^2 (bottom), against the ratio of the *up* and *down* reference values of the coefficients. The solid lines represent the limits obtained for models in the generalised SI ChEFT framework while the dashed lines are limits obtained from models constructed with the DirectDM framweork. The dotted-dashed lines represent the limits on $|C_u^{AV}|^2$ (magenta) and $|C_d^{AV}|^2$ (purple) with the included AA contribution, computed with the DirectDM framework.

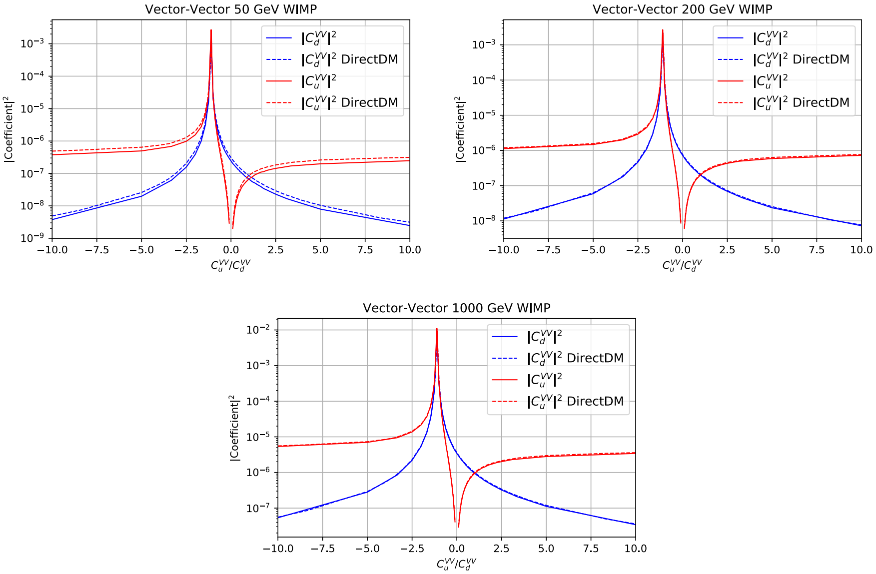

Figure 3.21: 90% confidence level upper limits on the Wilson coefficients of the vector mediated Dirac DM benchmark model of WIMP interactions for three different WIMP masses, 50 GeV/c^2 (top left), 200 GeV/c^2 (top right), and 1000 GeV/c^2 (bottom), against the ratio of the *up* and *down* reference values of the coefficients. The solid lines represent the limits obtained for models in the generalised SI ChEFT framework while the dashed lines are limits obtained from models constructed with the DirectDM framweork.

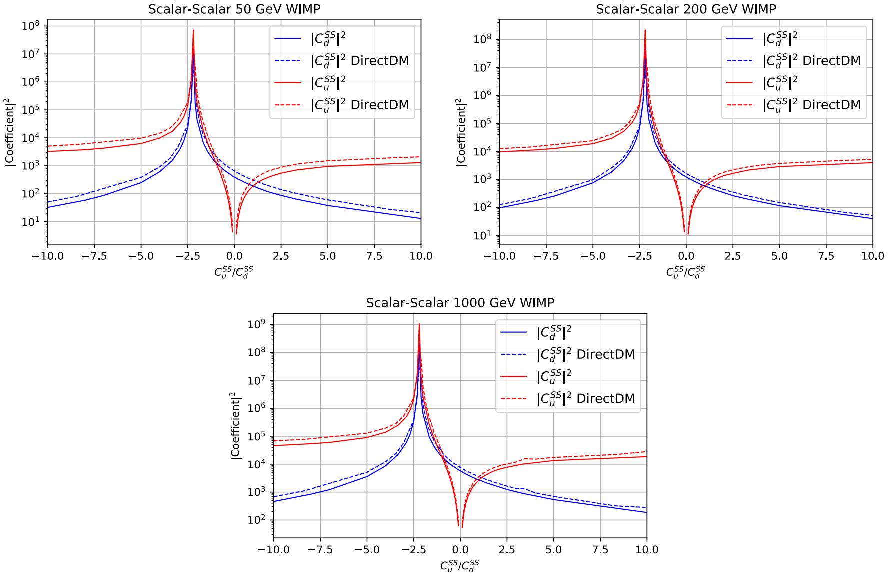

Figure 3.22: 90% confidence level upper limits on the Wilson coefficients of the scalar mediated fermion DM benchmark model of WIMP interactions for three different WIMP masses, 50 GeV/c^2 (top left), 200 GeV/c^2 (top right), and 1000 GeV/c^2 (bottom), against the ratio of the *up* and *down* reference values of the coefficients. The solid lines represent the limits obtained for models in the generalised SI ChEFT framework while the dashed lines are limits obtained from models constructed with the DirectDM framweork.

4. EFT analysis of Dark Matter - electron interactions with XENON1T data

This chapter describes the work related to the results presented in [PAPER II], regarding the EFT DM-electron interactions. Here we describe the theoretical framework and the signal model production as well as the limits obtained by analysing single-electron ionisation signals within the XENON1T detector.

4.1 Dark Matter - electron scattering

As introduced in Chapter 2, DM particles can scatter off electrons in the target material of direct detection experiments causing ERs. This type of interaction however has a fundamental difference in the type of DM particles it is sensitive to: given the current measurements of the DM distribution quoted in Table 1.1, low mass DM particles, with a mass $m_\chi \leq 1\,\mathrm{GeV/c^2}$, would not have enough kinetic energy to produce an observable energy deposition in NR, but the ionization signature from a scattering with an electron could be observed. Thus any study of ER produced by DM would focus on low mass particles, namely in the range 1-1000$\,\mathrm{MeV/c^2}$. Such a DM candidate is called "sub-GeV" or "light DM" (LDM) [79].
To correctly model a DM-electron interaction in a detector we need to describe quantitatively the scattering in terms of the initial and final state of the electron wave functions. Such description will be highly dependent of the detector material since the electrons are bound to the atoms of the target material, and arranged according to the specific chemical structure.
LDM interactions with electrons in the material can give rise to detectable signals in detectors via different channels, such as individual electron ionization, production of individual photons, and individual ions [80]. In this case we focus on the production of individual (or few) electrons through ionization in atomic medium, which corresponds to the conditions within the XENON1T detector.
In the case of single electron interaction, the LDM particle interacts with the

bound electron, giving rise to a final state where the electron is either in a higher energy bound state or it is completely ionised. Following Ref.[81], the LDM induced transition rate from the initial electron state $|\mathbf{e}_1\rangle$ to $|\mathbf{e}_2\rangle$ can be written as

$$\mathcal{R}_{1\to 2} = \frac{n_\chi}{16 m_\chi^2 m_e^2} \times \int \frac{\mathrm{d}^3 q}{(2\pi)^3} \int \mathrm{d}^3 v f_\chi(\mathbf{v}) (2\pi) \delta(E_f - E_i) \overline{|\mathcal{M}_{1\to 2}|^2} \tag{4.1}$$

which resembles the equation 2.3, with the key difference that the "cross section" here is expressed in terms of the squared electron transition amplitude, $\overline{|\mathcal{M}_{1\to 2}|^2}$, which is a function of the initial and final electron wave functions, $\psi_1(\mathbf{k})$ and $\psi_2(\mathbf{k}+\mathbf{q})$, and the scattering amplitude of free electrons, $\mathcal{M}(\mathbf{k},\mathbf{p},\mathbf{q})$, all with direct dependence on the electron and LDM momenta, $\mathbf{k}$ and $\mathbf{p}$ respectively, and the momentum transfer $\mathbf{q}$.
This expression generalises the material responses to DM-electron interactions proposed in Refs.[80, 82, 83] and allows the computation of observable energy depositions in terms of momentum direct momentum transfer dependence, i.e. EFT approaches.

4.1.1 EFT approach for DM-e interactions

Expressing the free scattering amplitude in terms of $\mathbf{k}$, $\mathbf{p}$ and $\mathbf{q}$ makes it easy to reparametrize it as a function only of $\mathbf{q}$ and the elastic transverse velocity,

$$\mathbf{v}_{el}^{\perp} = \frac{\mathbf{p}}{m_\chi} - \frac{\mathbf{q}}{2\mu_{\chi e}} - \frac{\mathbf{k}}{m_e} \tag{4.2}$$

where $\mu_{\chi e}$ is the reduced DM-electron mass. This is possible to do in the non-relativistic scenario of DM because of the invariance under Galileian transformations.
Now $\mathcal{M}(\mathbf{q},\mathbf{v}_{el}^{\perp})$ could also include the dependency on the spin of the LDM particle and the electron, $\mathcal{S}_\chi$ and $\mathcal{S}_e$ respectively. By expanding the free scattering amplitude in terms of $|\mathbf{q}|/m_e$ and $|\mathbf{v}_{el}^{\perp}|$ and keeping only the terms invariant under Galileian transformations we obtain expressions the same set of 14 operators as in the single nucleon NREFT in Eq. 2.10, where we should substitute the subscript N, indicating the nucleon, with e, to indicate the electron.
By introducing also information on the type of mediator of the interaction, specifically the mediator mass, two cases can be arise: when $m_{med}^2 \ll |\mathbf{q}|^2$, namely long range interaction, and $m_{med}^2 \gg |\mathbf{q}|^2$ i.e. contact interaction.
Without loss of generality the free scattering amplitude could be written as a linear combination of long-range and contact interactions, as

$$\mathcal{M}(\mathbf{q},\mathbf{v}_{el}^{\perp}) = \sum_i \left(c_i^s + c_i^l \frac{q_{ref}^2}{|\mathbf{q}|^2} \right) \langle \mathcal{O}_i \rangle \tag{4.3}$$

where the coefficient c_i^s denotes the contact interaction coupling and c_i^l denotes the long-range interaction coupling, $q_{ref}^2 = \alpha m_e$, and $\mathcal{O}_i$ are the NREFT operators considered for the specific scenario.

4.1.2 Specific models as combinations of EFT operators

From combination of NREFT operators some specific models of DM-electron interactions can arise. Three important models that have been studied in the DM community are the anapole coupling, and the magnetic and electric dipole moment couplings [84–86].
While the magnetic and electric dipole arise from an analogous dimension-5 Lagrangian of interaction as the one reported in Eq. 2.13 for which we reported NR coupling limits in Chapter 3, the anapole coupling arises from the dimension-6 Lagrangian

$$\mathcal{L}_{anapole} = \frac{g}{2\Lambda^2}\bar{\chi}\gamma^\mu\chi\partial^\nu F_{\mu\nu} \tag{4.4}$$

with g being a dimensionless coupling constant[1].

The magnetic dipole interaction maps onto an analogous linear combination of NREFT operators in the non relativistic limit, with short-range interactions for operators $\mathcal{O}_1$ and $\mathcal{O}_4$, with effective coefficients

$$c_1^s = 4em_e\frac{g}{\Lambda} \tag{4.5}$$

$$c_4^s = 16em_\chi\frac{g}{\Lambda}, \tag{4.6}$$

and long-range interactions for $\mathcal{O}_5$ and $\mathcal{O}_6$, with effective coefficients

$$c_5^l = \frac{16em_e^2m_\chi}{q_{ref}^2}\frac{g}{\Lambda} \tag{4.7}$$

$$c_6^l = -\frac{16em_e^2m_\chi}{q_{ref}^2}\frac{g}{\Lambda}. \tag{4.8}$$

The electric dipole interaction maps only onto $\mathcal{O}_{11}$ with the long-range coupling constant

$$c_{11}^l = \frac{16em_e^2m_\chi}{q_{ref}^2}\frac{g}{\Lambda}. \tag{4.9}$$

---

[1] The magnetic and electric dipole Lagrangians for the DM-electron case should also show g instead of the couplings C_F and $\tilde{C}_F$ present in Eq. 2.13.

Finally, the anapole interaction maps onto operators $\mathcal{O}_8$ and $\mathcal{O}_9$ with only contact couplings

$$c_8^s = 8em_em_\chi\frac{g}{\Lambda^2} \tag{4.10}$$

$$c_9^s = 8em_em_\chi\frac{g}{\Lambda^2}. \tag{4.11}$$

4.1.3 Xenon recoil spectra for specific EFT models

To use this model of DM-electron interaction in direct DM searches, instead of the rate in Eq. 4.1, we should consider the ionization rate, where the electron completely detaches from the atom. To do that the scattering amplitude $\mathcal{M}$ is derived using information about the occupied atomic orbitals, obtaining a differential rate of ionization of [81]

$$\frac{\mathrm{d}\mathcal{R}_{ion}^{n,l}}{\mathrm{d}\ln E_e} = \frac{n_\chi}{128\pi m_\chi^2 m_e^2} \times \int \mathrm{d}q\, q \int \frac{\mathrm{d}^3 v}{v} f_\chi(\mathbf{v})\Theta(v - v_{min})\overline{|\mathcal{M}_{ion}^{n,l}|^2} \tag{4.12}$$

where $|\mathcal{M}_{ion}^{n,l}|^2$ contains the dependency on $\mathcal{M}(\mathbf{q}, \mathbf{v}_{el}^{\perp})$ and the ionization form factor.

Considering the xenon atom and the DM kinetic energy, only the 5 most outer orbitals can produce a free electron in the final state in a DM-electron interaction. With the help of the computed xenon atom response from Ref.[81], we computed the recoil rate spectra for the anapole, and the magnetic and electric dipole models for the xenon orbitals $4s$, $4p$, $4d$, $5s$ and $5p$. In Figure 4.1 we show the obtained recoil spectra for a 90 MeV/c^2 DM particle for the three models and the individual orbitals.

These computed recoil rates are used in the following single electron analysis with XENON1T data.

4.2 XENON1T single electron results

Paper II describes the extensive work needed to select data from the XENON1T experiment where single or few electrons are emitted, as expected from LDM particles interacting with xenon atoms and shows the resulting limits on various LDM scenarios. Here we will briefly describe the detector response for single or few electron emission and present the signal models and the results for the three selected EFT models for the DM-electron interaction.

4.2.1 Detector response

In the case of LDM interacting with electrons in the xenon atom inside the XENON1T TPC, the atom can become ionised and the free electron might

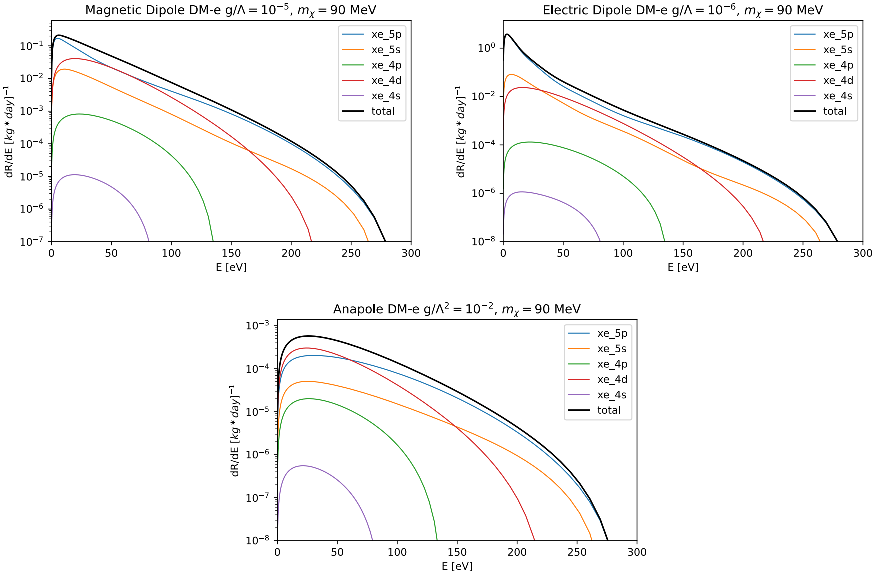

Figure 4.1: Recoil spectra for the magnetic dipole (top left), electric dipole (top right) and anapole (bottom) DM-electron interactions for a DM particle with a 90 MeV/c^2 mass and reference couplings of $g/\Lambda = 10^{-5}$, 10^{-6}, and $g/\Lambda^2 = 10^{-2}$ respectively. In the plots we show the differential rate for each of the xenon orbitals that a DM particle can ionise, as well as the total differential rate (black solid line).

produce secondary ionization while slowing down in the medium. The free electrons will drift towards the top of the TPC where they are extracted in the gaseous xenon and amplified towards the cathode, producing an S2 signal. While the primary DM-electron interaction might be too low energy to produce a prompt light signal (S1), the charge signal can be observed even in the case of single electrons being extracted from the liquid xenon.

The probability of producing an S2 signal is described by the modified Thomas-Imel model illustrated in Section 3.1.3 and Ref.[60] in the case of ER. However in this case given the low energy of the expected recoils, the energy cutoff for the energy-dependent charge yield Q_y (Eq. 3.8) was extrapolated from the calibration best fit down to 20 eV.

The S2 rate given a differential rate spectrum for a model is then computed

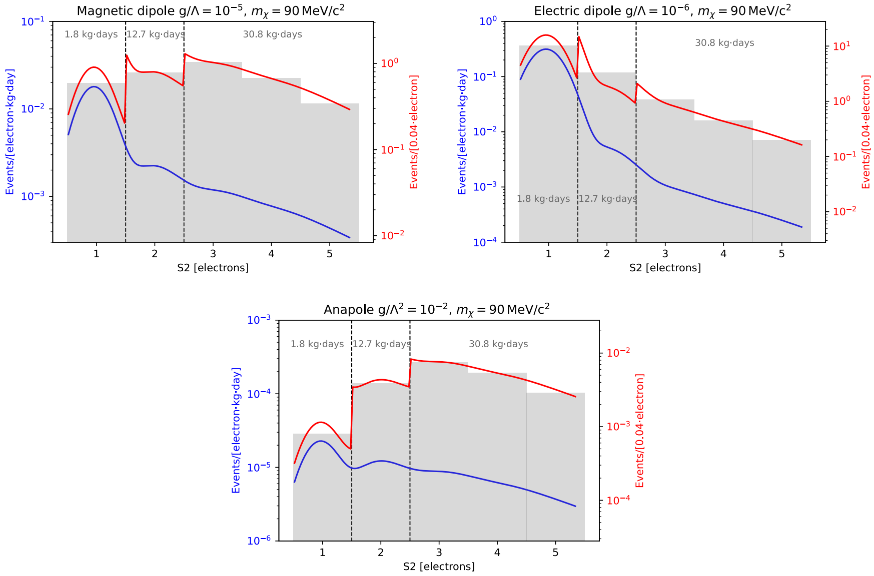

Figure 4.2: Signal models for the magnetic (top left) and electric (top right) dipole, and anapole (bottom) DM-electron interactions. The blue solid line shows the signal model as events per kg·day per electron, while the red solid line shows the signal model multiplied by the correct exposure for each analysis bin, as a result of the analysis data selection. The grey histogram shows the rate expectation in each bin, corrected by the exposure.

with the BBF fitting framework as [Paper II]

$$\begin{aligned} R(S2,z) = \varepsilon(S2) \times \sum_{n_e=1}^{\infty} \sum_{k=0}^{N} \int \mathrm{d}E_r \frac{\mathrm{d}R}{\mathrm{d}E_r} \mathrm{Binom}(k|N;p_e) \\ \times \mathrm{Binom}\left(n_e|k;\varepsilon_{ext} \times \exp\left(-\frac{z}{v_d \tau_e}\right)\right) \\ \times \mathrm{Gaus}(S2|\mu_{S2}^{se}, \sigma_{S2}^{se}) \end{aligned} \quad (4.13)$$

where $\varepsilon(S2)$ is the combined selection efficiency described in Paper II, n_e is the number of extracted electrons to the gaseous xenon, $N = E_r Q_y$ are the number of quanta created in the interaction, p_e is the probability of producing an electron in the DM interaction, $p_e = Q_y W$ (see Eq. 3.8), k are the quanta observed as electrons, $\varepsilon_{ext} \times \exp(-\frac{z}{v_d \tau_e})$ is the electron detection efficiency as a function of the drift time expressed as the depth, z, divided by the drift velocity, v_d, the electron lifetime τ_e, and the mean extraction efficiency ε_{ext}. Finally the Gaussian term contains the mean single electron gain, μ_{S2}^{se}, and its standard deviation, σ_{S2}^{se}.

Using the BBF framework we computed the signal models of the EFT models previously introduced. The spectra had to contain all the information for the individual orbital rates, to correctly compute the rates of ionization and observed electrons while accounting for the additional quanta created in the case of DM particles interacting with the inner shell electrons ($4s$, $4p$ and $4d$) [80]. In Figure 4.2 we show the signal models obtained with BBF for the three EFT models we previously described. The figures show both the number of events per electrons per kg·day and also the rate corrected by the final exposure after the data selection. The final exposure is 1.8 kg·days for the single electron extracted, 12.7 kg·days for two electrons and 30.8 kg·days for 3-5 electrons.

4.2.2 XENON1T limits on EFT anapole, magnetic and electric dipole

Paper II sets limits on a number of LDM models, however here we report the limits on the anapole, and magnetic and electric dipole models of DM-elecron interactions arising from the EFT framework proposed in [81]. The final limits, given the event rate in the XENON1T detector after the event selection, were computed by using the optimum-interval method [87]. The uncertainty on the signal expectation accounts for $\sim 5\%$ uncertainty on the electron lifetime and $\sim 2.5\%$ uncertainty on the S2 gain.

Here we show the limits computed on the couplings g/Λ^2 for the anapole model, and on g/Λ for the magnetic and electric dipole models in Figure 4.3, which are the first limits from experimental results reported on these models.

In conclusion we have discussed the generalisation of the DM-electron scattering that allows an EFT description of the interactions, dependent on the momentum transfer, and how specific DM-electron interaction models can arise or be modelled as combinations of effective operators. We have computed the recoil spectra for the anapole, the magnetic and electric dipole models for DM-electron interactions with xenon atoms, and created the signal models using the XENON1T detector response for single-electron emission. Finally we reported the experimental limits for the three EFT derived models.

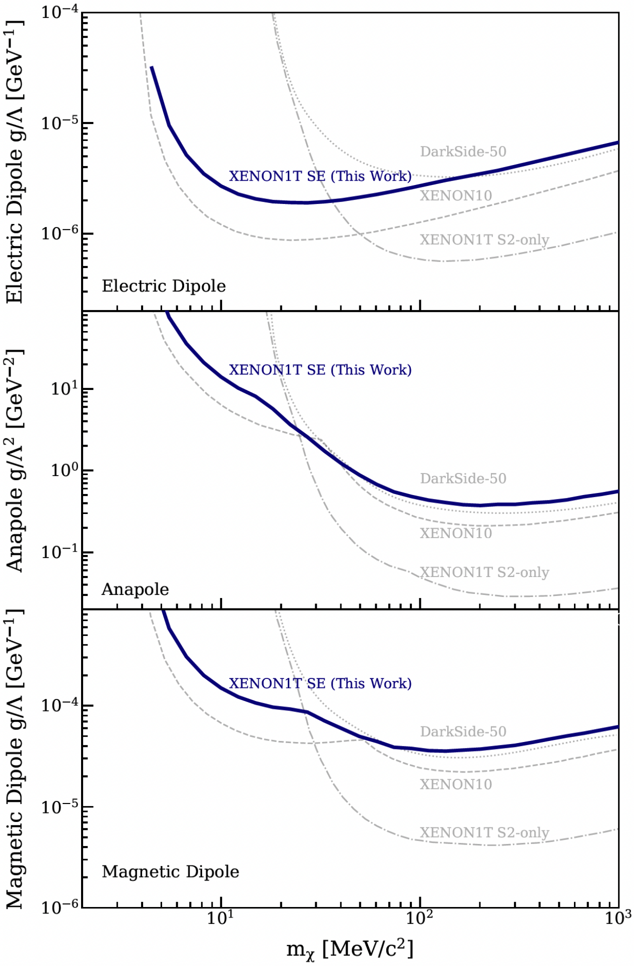

Figure 4.3: Figure from Paper II. Limits on the electric dipole (top), anapole (center), and magnetic dipole (bottom) couplings derived from the XENON1T single-electron data selection. As a reference the limits computed in Ref.[81] using the results from XENON10 [88] (dashed lines), XENON1T S2-only analysis [89] (dotted-dashed lines), and DarkSide-50 [90] (dotted lines), are also shown.

5. FLAMEDISX and application on XENONnT background modelling

This chapter describes the FAMEDISX software package, a modelling and inference package that makes use of matrix multiplication to model the xenon signal emission and to compute event-wise the likelihood of liquid xenon TPCs in DM searches, and shows an application of it in the modelling of the surface background for XENONnT, an important spatial dependent background that is crucial to model in order to maximise the fiducial volume. The FLAMEDISX method and signal emission model, together with sensitivity studies and comparison to traditional template-based inference are described in [PAPER III] and in Ref. [12]. Here we will describe the implementation of the xenon emission model and focus on the differences with the XENON1T modified Thomas-Imel model described in Section 3.1.3 and the parametrization of the charge and photon yields. Then we will briefly recap the likelihood construction and computation, and finally we will introduce a way of modelling the TPC surface model, based on XENONnT data.

5.1 FLAMEDISX

Traditionally the WIMP direct detection analyses are performed by computing likelihood functions based on PDFs constructed through MC methods and template morphing, as is the case for XENON1T and as described in Chapter 3. However an analytical approach is possible by computing the likelihood for each event. This section will describe the method and the implementation of the analytical construction of a xenon TPC likelihood. The software package that implements this method is called FLAMEDISX [91], Fast Likelihood Analysis in MorE DImensionS for Xenon TPCs, and has been developed using Tensorflow [92], which simplifies and optimizes the matrix multiplications required through graph computation, and provides autodifferentiation i.e. the automatic computation of gradients and Hessians with respect to the model parameters, simplifying the likelihood maximization step for inference.

5.1.1 Signal emission model

The emission model implemented in FLAMEDISX is inspired by the modified Thomas-Imel model described in Section 3.1.3, for both ER and NR, with some differences however. The foundation of the model is the computation of the number of quanta produced in a recoil

$$n_q = \lfloor E/W \rfloor \tag{5.1}$$

where E is the true recoil energy and W is the mean energy needed to produce a measurable quantum (electron or photon) in the detector. This is expression is a good estimation for the ER, where we can model the probability of producing n_q quanta as $P(n_q|E)_{ER} = \delta(\lfloor E/W \rfloor)$. For the NR, we have to account for the energy lost to heat, as previously described, using the energy dependent Lindhard factor $L(E)$. Thus we model the distribution of n_q as

$$P(n_q|E)_{NR} = \mathrm{Pois}(nq|\lfloor EL(E)/W \rfloor). \tag{5.2}$$

Given a recoil differential rate $\dfrac{\mathrm{d}R(E,\mathbf{x})}{\mathrm{d}E_r}$ dependent on the recoil energy and the interaction position and time ($\mathbf{x} = (x,y,z,t)$) in the detector in units of $[events/(keV\,tonne\,year)]$, and the spectrum resolution ΔE, we define

$$R_0(E,\mathbf{x}) = \Delta E \frac{\mathrm{d}R(E,\mathbf{x})}{\mathrm{d}E_r}. \tag{5.3}$$

We convolve then R_0 with the probability of creating n_q quanta to obtain a differential rate in terms of n_q as

$$R_1(n_q,\mathbf{x}) = \sum_E P(n_q|E) R_0(E,\mathbf{x}) \tag{5.4}$$

where the sum runs over the energies with the resolution ΔE, which approximates the integral of the convolution. Once the total number of detectable quanta is computed, they can be either photons or electrons, hence we can express the next steps in terms of only the probability a quantum being an electron, p_e. For the NR, the ratio between the number of electrons and number of photons produced is fixed, allowing us to model the number of electrons produced as

$$P(n^{el}_{prod}|n_q)_{NR} = \mathrm{Binom}(n^{el}_{prod}|n_q, p_e). \tag{5.5}$$

For the ER the fraction of electrons and photons fluctuates and this is traditionally modelled by a Gaussian dispersion on top of p_e [60, 93], with mean μ_{pe}

and standard deviation σ_{pe}. In our case however, this description would lead to both unphyisical results, with $P(p_e|n_q) > 0$ for $p_e < 0$ and $p_e > 1$, and a non-analytical form for $P(p_e|n_q)$. Thus, to account for the additional dispersion of p_e we model it as

$$P(p^{el}_{prod}|n_q)_{ER} = \mathrm{BetaBinom}(p^{el}_{prod}|n_q, \alpha, \beta) \tag{5.6}$$

where the parameters of the Beta-Binomial function are

$$\alpha = \mu_{pe}\left(\frac{\mu_{pe}}{\sigma^2_{pe}} - \frac{\mu^2_{pe}}{\sigma^2_{pe}} - 1\right) \qquad \text{and} \qquad \beta = \alpha\left(\frac{1}{\mu_{pe}} - 1\right). \tag{5.7}$$

The parameters μ_{pe} and σ_{pe} are important *model functions* that describe the charge yield and the electron recombination fluctuation for the ER signals, and so is p_e for the NR. *Model functions* are important to accurately describe the different signal *sources* and will be discussed later.
The rate of produced electrons and photons can then be computed, given that $n_q = n^{el}_{prod} + n^{ph}_{prod}$, as

$$R_2(n^{el}_{prod}, n^{ph}_{prod}, \mathbf{x}) = \sum_{n_q} P(p^{el}_{prod}|n_q) R_1(n_q, \mathbf{x}) \delta(n_q = n^{el}_{prod} + n^{ph}_{prod}). \tag{5.8}$$

To compute the rate of detected signals i.e. S1 and S2, we need to now model the detection probability of the produced quanta and the detector response for the light and charge signals.
The detection probabilities for photons and electrons, given the number of produced quanta, n^{el}_{prod} and n^{ph}_{prod}, are modelled as Binomial distributions multiplied by the respective acceptance functions:

$$P(n^{el(ph)}_{det}|n^{el(ph)}_{prod}) = f^{el(ph)}_{acc}(n^{el(ph)}_{det})\mathrm{Binom}(n^{el(ph)}_{det}|n^{el(ph)}_{prod}, \varepsilon_{el(ph)}). \tag{5.9}$$

The probability for the Binomial is given by the *per-quanta* detection efficiency and it is different for photons and electrons. The electron detection efficiency is a function of the electron extraction efficiency and the electron lifetime τ_e and the drift time,

$$\varepsilon_{el} = \varepsilon^{ext}_{el} \exp\left(-\frac{t_{drift}}{\tau_e}\right), \tag{5.10}$$

while the photon detection efficiency is externally give according to estimates of the optical properties of the detector and the efficiency of the PMTs. The acceptance functions, f_{acc}, are *per-event* efficiencies, depending on the number of photons or electrons detected. In particular the electron acceptance is very high, ~ 1, while the photon acceptance depends on the number of photons detected, with a threshold on a minimum number of photons from the raw S1 to avoid accidental coincidences due to PMT dark counts, and the event reconstruction efficiency.

The final observable signals, the S1 and S2, can now be computed. The S1 signal however, being considerably smaller than the S2, needs to account for the non-Gaussian PMT response in the case of single photons [60, 94]. In the PMTs used in XENON1T and XENONnT, the probability of producing more than one single photo-electron for a single photon detected is $p_{DPE} = 0.219$ [60]. In FLAMEDISX we model the number of photo-electrons produced according to a Binomial distribution, as

$$P(n_{det}^{pe}|n_{det}^{ph}) = \text{Binom}(n_{det}^{pe} - n_{det}^{ph}|n_{det}^{ph}, p_{DPE}) \tag{5.11}$$

where n_{det}^{pe} is the number of photo-electrons detected. This factor is set to zero when $n_{det}^{pe} < n_{det}^{ph}$ and it is not applied for the S2 signal, where the signals are relatively much stronger and the non-Gaussian behaviour of the double photo-electron emission (DPE) is negligible.
The final S1 and S2 signal size follow Gaussian distributions, for S1 it is a conditional probability given the number of photo-electrons detected,

$$P(S1|n_{det}^{pe}) = f_{acc}(S1)\text{Gaus}(S1|\mu_{S1}(n_{det}^{pe}), \sigma_{S1}(n_{det}^{pe})), \tag{5.12}$$

and for S2, given the number of electrons extracted,

$$P(S2|n_{det}^{el}) = f_{acc}(S2)\text{Gaus}(S2|\mu_{S2}(n_{det}^{el}), \sigma_{S2}(n_{det}^{el})). \tag{5.13}$$

The S1 and S2 acceptances, $f_{acc}(S1)$ and $f_{acc}(S2)$, are additional detection efficiency functions parametrised in terms of S1 and S2, such as detection thresholds or regions of interest in the S1 or S2 spaces. The Gaussian parameters of Eq. 5.12 and 5.13 are defined in terms of the single photo-electron or electron, assuming a linear detector response, as

$$\begin{aligned}
\mu_{S1}(n_{det}^{pe}) &= \mu_1^{S1} n_{det}^{pe} \\
\sigma_{S1}(n_{det}^{pe}) &= \sigma_1^{S1} \sqrt{n_{det}^{pe}} \\
\mu_{S2}(n_{det}^{el}) &= \mu_1^{S2} n_{det}^{el} \\
\sigma_{S2}(n_{det}^{el}) &= \sigma_1^{S2} \sqrt{n_{det}^{el}},
\end{aligned}$$

where $\mu_1^{S1(S2)}$ and $\sigma_1^{S1(S2)}$ are the mean and standard deviation of the area of S1 (S2) of the single photo-electron (electron) detected.

The final model can be then written as the differential rate of S1 and S2, $R(S1, S2, \mathbf{x})$, by summing over the all the quanta produced and detected the

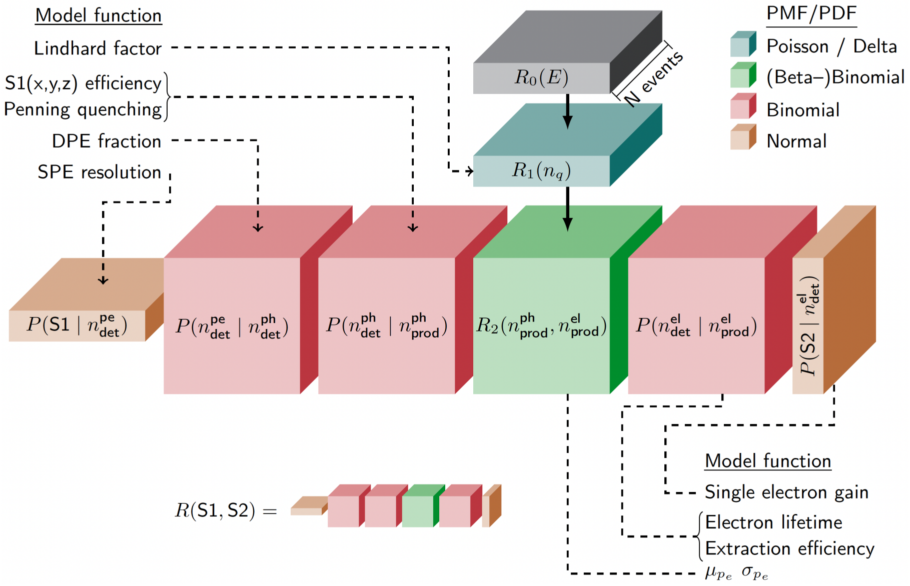

Figure 5.1: Block diagram of the LXe emission model and implemented TPC response in FLAMEDISX. Figure from [Paper III]. The S1-S2 differential rate, $R(S1,S2,\mathbf{x})$, is the sum, from left to right, of the matrix multiplication of the tensors (blocks) of the bottom row. In the figure are also shown some of the model functions that enter the computation at the different steps. The tensors are shown with the depth dimension being the number of events N, since the computation runs on batches of events. This model representation corresponds to the differential rate of a single signal source, either ER or NR. In a complete analysis multiple sources can be computed repeating the same structure, but with different model functions.

matrix multiplication of the quantities obtained as follows:

$$
\begin{aligned}
R(S1,S2,\mathbf{x}) = \sum_{n^{pe}_{det}} \sum_{n^{ph}_{det}} \sum_{n^{ph}_{prod}} \sum_{n^{el}_{prod}} \sum_{n^{el}_{det}} & P(S1|n^{pe}_{det}) P(n^{pe}_{det}|p^{ph}_{det}) P(n^{ph}_{det}|n^{ph}_{prod}) \\
& R_2(n^{ph}_{prod}, n^{el}_{prod}, \mathbf{x}) P(n^{el}_{det}|n^{el}_{prod}) P(S2|n^{el}_{det}).
\end{aligned}
\tag{5.14}
$$

The model can be more easily described through a schematic block structure that separates each step of the computation. The block diagram is shown in Figure 5.1 and the same structure was used in the code implementation of the software using the Python3 [95] programming language and TensorFlow [92].

5.1.2 Signal sources

The parameters of the probability distributions and the efficiencies showing up in the previous section are all *model functions*. Some of the model functions crucial to describe various signal characteristics are also shown in Figure 5.1, with the corresponding sections where they act upon. A *source* is defined as a class of events that produce a signal corresponding to the same differential rate R_0 and the same interaction or recoil type. Events that are produced belonging to a source will share the same emission model in FLAMEDISX. In an analysis multiple sources can be defined, differentiated by either recoil type, differential rate spectra, or model functions. In Flamedisx there are two main sources defined: ER and NR.

The ER source and the NR source are differentiated already in the behaviour of the core blocks and the probability computation, with the first difference being the Lindhard factor in Eq. 5.2, which for ER is $L(E) \simeq 1$.
In Eq. 5.8, the quanta splitting for the ER is described as a Beta-Binomial and two important model functions govern it: μ_{pe}, which governs the probability of producing an electron, p_e, and σ_{pe} which corresponds to its fluctuation. These two functions can be modelled in the same way defined as in the XENON1T charge yield, following the Eq. 3.8 for μ_{pe}, and Eq. 3.6 for σ_{pe} to describe the electron recombination fluctuation. For the NR source p_e can be modelled according to the fit in Ref. [57] to follow the model used by the XENON Collaboration [60].
Other sources can be constructed starting from the base definition of ER and NR sources and they can be differentiated by adding specific spatial dependence of the differential rate for example to describe spatially dependent backgrounds e.g. radiogenic neutrons or surface backgrounds, time dependent recoil rates e.g. WIMP spectra for time modulation searches, or by changing model functions that describe the detector conditions at different times e.g. acceptance functions, time dependent electron lifetime, PMT gain etc.
Some signals, such as accidental coincidences, do not follow the LXe emission model and thus need to be modelled externally. To do that in FLAMEDISX they can be given as templates of recoil differential rate from which to read the contribution for each event.

5.1.3 Likelihood and inference capabilities

The likelihood function can be constructed in FLAMEDISX using one or multiple sources, given data. FLAMEDISX constructs an unbinned likelihood defined as

$$\mathcal{L}(\mu, \boldsymbol{\theta}|\mathbf{D}) = \mathrm{Pois}(n|\mu(\boldsymbol{\theta})) \prod_{i=1}^{n} \sum_{j}^{sources} \frac{R_j(\mathbf{d}_i, \boldsymbol{\theta})}{\mu} \tag{5.15}$$

where $\mathbf{D}$ is the given data set, $\mathbf{d}_i = (S1, S2, x, y, z, t)$ are the single events with all the observables that go into the model, and $\boldsymbol{\theta}$ are the parameters of the model. The sources that are given as templates are summed to the differential rates obtained from the LXe emission model, and possible parameter constraints can be included in the likelihood by multiplying it by a function of the parameters, $f(\boldsymbol{\theta})$. When taking the logarithm the final likelihood function becomes

$$\begin{aligned}\log \mathcal{L}(\mu, \boldsymbol{\theta}|\mathbf{D}) = &- \mu(\boldsymbol{\theta}) + \sum_{i=1}^{n} \log \left(\sum_{j}^{sources} R_j(\mathbf{d}_i, \boldsymbol{\theta}) + T(\mathbf{d}_i) \right) \\ &+ \log(f(\boldsymbol{\theta})) + \text{const}\end{aligned} \tag{5.16}$$

where $T(\mathbf{d}_i)$ is the template computed at the event $\mathbf{d}_i$, and $f(\boldsymbol{\theta})$ are the parameter constraints.

The total rate $\mu(\boldsymbol{\theta})$ is a function of the model parameters however, since changing the model functions will affect the differential S1-S2 rate, and this can be problematic when computing the likelihood. To solve this problem, we compute μ by simulating a large number of events, $\mathcal{O}(\sim 10^5)$, for the model at anchor points in a large range of the parameter space and interpolate the rate between these points in the likelihood construction step.

When computing the likelihood, thanks to TensorFlow's autodifferentiation, we compute and store also the gradient and the second derivative of the likelihood function with respect to all the free parameters of the model. This makes the likelihood function much easier to explore when maximizing it in finding the best fit parameters. The second derivative provides also direct access to the parameter uncertainty when computing the best fit.

The explicit multi-dimensional likelihood in FLAMEDISX and the simple simulation capabilities due to the explicit probabilistic nature of the FLAMEDISX emission model, make the framework relatively easy to use in model building and model validation. This aspect will be further explored later in this Chapter.

Another important aspect of the framework is that it enables inference on a multidimensional likelihood, where the dimensionality of the non trivial parameters of the model do not make the computational time scale exponentially, as is the case with the classical template morphing approach. By using tensor multiplication, the model can be accelerated by using Graphical Processing Units (GPUs), which in this case do not need any special code, since TensorFlow will use GPUs automatically if available and thanks to the graph construction the model does not need to be reconstructed for new data sets. In Figure 5.2 the benchmark of the model construction and the fit of an ER model with polynomial charge yield of various orders for FLAMEDISX, compared to the construction time required for templates (2D and 6D templates) for mod-

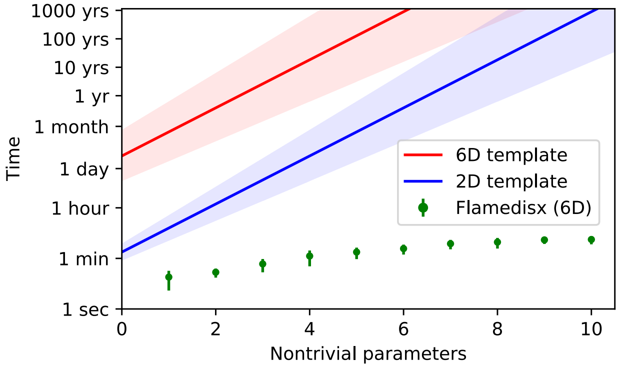

Figure 5.2: Figure from [Paper III]. Benchmark of the FLAMEDISX model building and fitting (green dots) of an ER model with a polynomial charge yield of various order. The error bars correspond to statistical fluctuations from repeating the fits with different toy datasets. The lines represent the estimated time required to construct the necessary templates as a function of the number of parameters that affect the observable distribution, for 6D templates (red) and 2D templates (blue).

els with the same amount of non-trivial parameters, with 5 to 10 templates for each parameter.

Finally, the multidimensional likelihood, since it can use much more information from the event observables directly, could provide a better discrimination power with respect to the traditional template method, resulting in better limits or higher discovery significance with lower exposure times, as shown in [PAPER III].

5.2 XENONnT

The XENONnT experiment is the next iteration of the XENON liquid xenon TPCs, direct successor of XENON1T. The detector is now being operated and taking data at LNGS.

Part of the infrastructure built for XENON1T is being reused for XENONnT, including the water tank shielding with the muon-veto system and the cryostat. The purification and re-circulation systems have been upgraded and the DAQ system was expanded to accommodate a higher number of PMTs.

XENONnT will also have a neutron veto system. The neutron veto will consist of doping the water of the water tank with gadolinium, an element with a very high neutron capture cross section, and observing the light from the conversion of the γ-rays emitted in the process with 120 additional PMTs placed in the

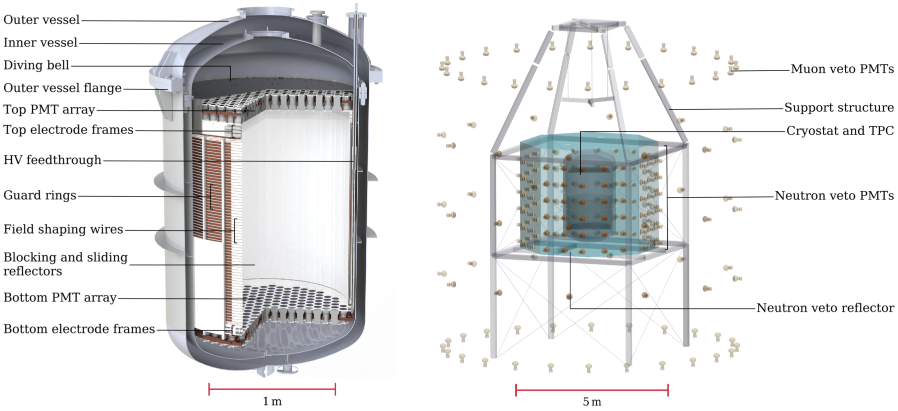

Figure 5.3: CAD rendering of the XENONnT cryostat and TPC (left panel) and of configuration of the detectors in the water tank, with the outer muon veto PMTs, inner neutron veto PMTs and the cryostat at the centre (right panel), from [96]

volume surrounding the cryostat.

The inner TPC is 148.5 cm tall with a radius of 1.3m. The field is achieved in a similar manner to XENON1T, with all the wire grids and field cage scaled up to the new dimensions. The TPC is instrumented with 494 Hamamatsu R11410-21 PMTs, the same type as XENON1T, with 253 PMTs in the top array and 241 in the bottom array [96].

In Figure 5.3 the XENONnT inner detector and the instrumented water tank with the neutron veto system are illustrated.

5.3 XENONnT Wall background: a model building example with FLAMEDISX

Events in the TPC originating from the surfaces of the TPC walls are an intrinsic background of LXe TPCs. These events, as described in Chapter 3, are ER events from the decay of radioactive material, usually ^{222}Rn and daughters like ^{210}Pb and ^{210}Po, that accumulate onto these surfaces while exposed to air. Their signature in the detector observables are events distributed around the maximum radius of the TPC with a seemingly normal S1 but with a smaller S2 than a normal ER event. One possible explanation for the lower S2 is that given the close proximity to the TPC walls, some of the charge is lost on the surfaces, resulting in a lower charge yield.

In this section we will discuss a possible way of effectively modelling such background using the FLAMEDISX LXe emission model and making use of the spatial information.

5.3.1 Emission model

To effectively replicate the wall signal emission we can start from a uniform ER energy spectrum in the range of $[0,80]\,\mathrm{keV}_{er}$. The S1-S2 region where modelling the wall events is important is that corresponding to the WIMP search ROI, with normal ER events up to $20\,\mathrm{keV}_{er}$ and normal NR events up to $80\,\mathrm{keV}_{nr}$, or in the S1 range of $[0,150]$ PE, and S2$< 10^4$ PE. Charge loss due to the proximity of the PTFE walls of the TPC change the S2 signature of this background, making the overall S2 distribution to lose the band-like structure of typical ER events. To model the S2 distribution in FLAMEDISX we can modify some of the model functions in the electron detection block, Eq. 5.9, and in the S2 creation block, Eq. 5.13, namely the electron detection efficiency function and the single-electron gain mean, μ_{S2}, and single-electron gain standard deviation, σ_{S2}, functions.
First, we simplify the charge yield, p_e in Eq. 5.6 and Eq. 5.7, of the ER to be a simple exponentially falling yield,

$$p_e = C_e \exp\left(-\lambda n_q \cdot W\right), \tag{5.17}$$

where C_e and λ are free parameters and $W = 13.7\,\mathrm{eV}$ is the mean energy needed to produce a measurable quantum from Eq. 5.1.
The next step would be either to considerably reduce the extraction efficiency term in Eq. 5.9, or to have an additional efficiency term, f^{el}_{loss} that accounts for the amount of charge lost due to the wall proximity.
In a normal ER band at low energy the S2 grows as the recoil energy goes up. The events close to the TPC surfaces though show a rather uniform mean S2 values for S1 slices in the range $[0,150]$ PE. To model this behaviour the new efficiency term should be a function of the number of produced electrons, n^{el}_{prod}, and in this case we model it as

$$f^{el}_{loss} = l_{max} e^{-a n^{el}_{prod}} + l_{min} \tag{5.18}$$

with l_{max} and l_{min} being constants with the imposed condition of $l_{max} + l_{min} \leq 1$, and together with the exponential scaling parameter a can be free parameters to be determined in a likelihood fit on calibration data.
While this model is not physical in many regards it serves as an example of modelling this detector specific background in the context of explicit likelihood computation of FLAMEDISX and can serve as a stepping stone towards a more physical interpretation.

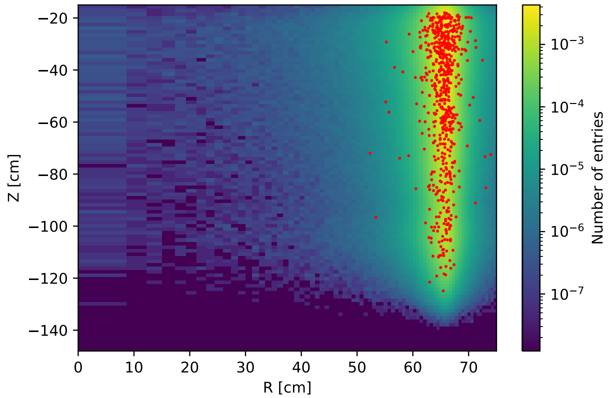

Figure 5.4: 2D Projection of the spatial template in Z-R generated as an input for the spatial dependence of the FLAMEDISX wall model with the ^{220}Rn calibration data (red dots) overlaid.

5.3.2 Spatial template and data selection

To model the surface background we use the ^{220}Rn calibration runs of XENONnT for the first data taking campaign of the experiment. From the entire data set we select only the low-energy events with S1<150 PE. In these events, in the cS1-cS2 space we place a selection cut to exclude the proper ER events, setting a cut below 2σ of the ER distribution. To exclude AC events we set an S2 threshold of S2>300 PE, and in order to exclude events originating at the very top and the very bottom of the TPC, such as electrode photo-ionization and gas events, we select only events with $-145\,\mathrm{cm} < Z < -18\,\mathrm{cm}$. This selection gives us 887 events which are a relatively clean sample of wall events.

To correctly model the spatial distribution of events in FLAMEDISX we require a spatial template that gives the probability of observing events at a given position. Since surface events have a specific spatial distribution around the edges of the detector, we need to create a 3D template in cylindrical coordinates [R, Z, θ]. For simplicity we assume the events are uniformly distributed in θ. The R distribution we choose to model according to a Skew-T distribution [97, 98], $R \sim \mathrm{SkewT}(\mu, \sigma, \nu, \tau)$, to account for the skewness of the events extending towards the inner part of the TPC. The parameters of the distribution were obtained through an unbinned likelihood fit of the events, maximizing the likelihood

$$\mathcal{L}(\mu, \sigma, \nu, \tau | \mathbf{R}) = \prod_{i}^{N} \mathrm{SkewT}(R_i; \mu, \sigma, \nu, \tau), \tag{5.19}$$

with the best fit obtained parameters being $\hat{\mu} = 65.5 \pm 0.5$, $\hat{\sigma} = 2.4 \pm 0.4$, $\hat{\nu} = 0.85 \pm 0.01$, $\hat{\tau} = 2.8 \pm 0.4$. For the distribution sampling and the evalu-

ation of the Skew-T distribution we used the Python package Sstudentt[1]. Finally, the Z distribution is modelled using an adaptive Kernel Density Estimation (AKDE) method [99], with Gaussian kernel, using the Python package Awkde[2].
The final template is obtained by sampling 3×10^7 events from the [R, Z, θ] distributions and constructing the 3D histogram using the Multihist[3] package. The template binning was chosen to be uniform in Z and θ, with respectively 100 and 60 bins, and 75 uniform bins in R^2. In Figure 5.4 we show the normalised R-Z projection of the constructed [R, Z, θ] spatial template, with an overlay of the ^{220}Rn data sample selected from the first calibration run of XENONnT.

5.3.3 Surface model likelihood fit with FLAMEDISX

As described in Sec. 5.3.1, the emission model is based on the ER source defined in FLAMEDISX, inheriting the all the model functions that we did not modify specifically to describe the wall events, namely the S1 branch, including the S1 gain ($\mu_1^{S1} = G_1$) which is kept as a parameter for the likelihood. In the S2 branch, besides the modified model functions mentioned, we maintain the electron recombination fluctuation function as defined in Eq. 3.6, with the free parameters q_2 and q_3, and the single electron gain mean μ_1^{S2} and the single electron standard deviation σ_1^{S2}, both dependent only on the constant parameter G_2.
Finally we construct the explicit multidimensional likelihood with FLAMEDISX for the wall emission source with the data set selected above, with 10 free shape parameters, and maximize the likelihood with respect to the parameters. In Table 5.1 we show the full set of parameters of the likelihood for the wall model, the best fit and where they occur in the model. In this parametrization C_e and q_3 are dimensionless, in units of n_q.
From the best-fit model we simulate $\mathcal{O}(10^5)$ events to compare the FLAMEDISX model to the data. In Figure 5.5 we show the 2D histogram of the simulated events in S1-S2 with the overlaid ^{220}Rn calibration data, and the S2 histogram for the simulation and the data. While the model seems to describe rather well the data in these dimensions, we compute two benchmark goodness of fit (GOF) tests in the crucial space of S1-S2 and in R-S2.
The GOF of choice in this case is the Poisson-likelihood χ^2 [100] for 2D equiprobable binned histograms. To construct the equiprobable binning, we used the simulated $\sim 10^5$ events as a reference sample, to compute the effec-

---

[1] https://github.com/berrij/sstudentt

[2] https://github.com/mennthor/awkde

[3] https://github.com/JelleAalbers/multihist

Parameter	Type	Best fit (Value)	Occurrence
W	fixed	13.7 eV	Eq. 5.1
C_e	free	$(1.74 \pm 0.12) \times 10^{-4}$	μ_{pe} Eq. 5.6, 5.7, 5.17
λ	free	(0.015 ± 0.010) keV^{-1}	μ_{pe} Eq. 5.6, 5.7, 5.17
q_2	free	$(97.8 \pm 0.5) \times 10^{-4}$	σ_{pe} Eq. 5.6 and 5.7, Eq. 3.6
q_3	free	145 ± 100	σ_{pe} Eq. 5.6 and 5.7, Eq. 3.6
ε_{el}^{ext}	free	0.89 ± 0.02	Eq. 5.10
τ_e	fixed	8.73 ms	Eq. 5.10
l_{max}	free	0.084 ± 0.007	Eq. 5.18
l_{min}	free	0.02 ± 0.02	Eq. 5.18
a	free	$(0.1 \pm 0.1) \times 10^{-3}$	Eq. 5.18
G_1	free	0.0931 ± 0.0009 PE/photon	μ_{S1}, Eq. 5.12
G_2	free	25.5 ± 0.3 PE/e$^-$	μ_{S2}, Eq. 5.13
p_{DPE}	fixed	0.219	Eq. 5.11

Table 5.1: The parameters of the wall emission model in FLAMEDISX. The parameters indicated as "fixed" were kept constant in the likelihood, while the "free" parameters were allowed to be fitted. The best fit values are reported for the free parameters with the uncertainty obtained from the second derivative of the likelihood curve at the best fit.

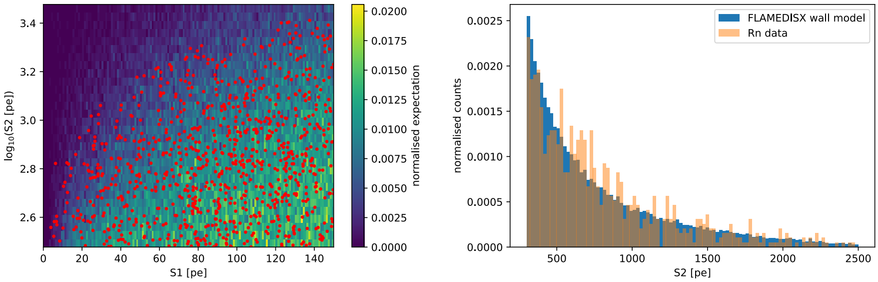

Figure 5.5: The left panel shows the 2D S1-S2 histogram of the $\sim 10^5$ simulated events from the best fit wall model with FLAMEDISX, with the ^{220}Rn calibration data of XENONnT (red dots) overlaid. The right panel shows the S2 histograms of the best fit FLAMEDISX wall model simulated data (blu) and the ^{220}Rn data (red).

tive Cumulative Density Function (CDF), $F(x,y)$, chose the ordering to first compute the x equiprobable bins and then y, and divided $F(x,y)$ according to the respective number of bins in each dimension. For these GOF tests we choose to divide the data set in 9 bins the x axis, which corresponds to S1 in the first test and R in the second test, and 13 bins for y, that corresponds to the S2 dimension. This way each bin has an expectation of $\lambda_{bin} = 7.6$ events when normalised to the number of events in the ^{220}Rn calibration data. To compute the equiprobable binning and perform the GOF test, we used the Python package GOFevaluation[1][101] developed by the XENON Collaboration.
The Poisson-likelihood χ^2 GOF p-value obtained for the S1-S2 distribution is $p = 0.091$, while for the R-S2 distribution the p-value is $p = 0.085$, in both cases the GOF tests indicate a good fit. In Figure 5.6 and 5.7 we show the equiprobable binning of the model with the calibration data overlaid and the deviation from the expectation value for each bin, for the S1-S2 and the R-S2 distributions respectively.
For the S1-S2 distribution it can be observed in the right panel of Figure 5.6 that the model slightly over-predicts events in the region of $S1 > 100\,\mathrm{PE}$ and $1000\,\mathrm{PE} > S2 > 2000\,\mathrm{PE}$, while it shows signs of under-prediction in the region where the calibration data was cut to eliminate the proper ER band. While the localised over-prediction in the high energy region could be a statistical under-fluctuation of the calibration data, the model under-prediction in the region of $S1 < 80\,\mathrm{PE}$ where the ER selection cut is placed, could indicate proper ER events that were not correctly cut and leaked in the wall selection. Furthermore at very low S1 and S2 the data can have also AC events that we were unable to exclude.

5.4 Outlook

While this study is not enough to properly characterise the surface background, it serves as a working example that FLAMEDISX could be used for modelling non-standard TPC backgrounds. For a proper wall background characterization, the study should be replicated with science run data, for a data-driven study. This model could be used to define a fiducial volume in the TPC where the surface background component is minimised and can be used for predictions if properly normalised to according to the exposure time, which cannot be properly done with calibration data with radioactive ^{220}Rn injected in the detector.
This model however could serve also as a stepping stone towards a physical interpretation of the surface events, however for that we need precise simulations

---

[1] https://github.com/XENONnT/GOFevaluation

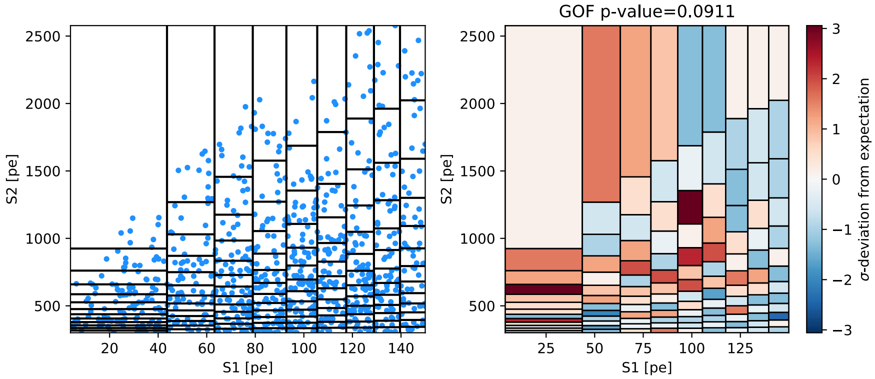

Figure 5.6: The left panel shows the S1-S2 equiprobable bins obtained from the FLAMEDISX wall model with the overlaid ^{220}Rn calibration data (blue dots). Each bin has an expectation value of $\lambda_{bin} = 7.6$ events. The right panel shows on the color map the deviation in numbers of σ of the ^{220}Rn data for each equiprobable bin in the S1-S2 space from the bin expectation value of the Poisson-likelihood. The computed GOF p-value obtained is $p = 0.091$.

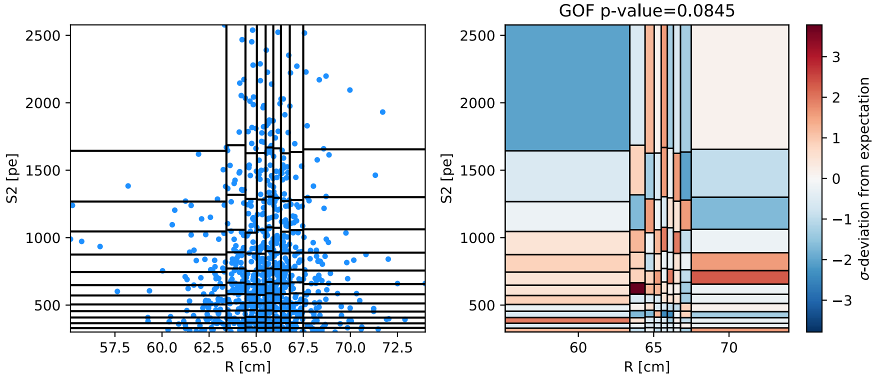

Figure 5.7: The left panel shows the R-S2 equiprobable bins obtained from the FLAMEDISX wall model with the overlaid ^{220}Rn calibration data (blue dots). Each bin has an expectation value of $\lambda_{bin} = 7.6$ events. The right panel shows on the color map the deviation in numbers of σ of the ^{220}Rn data for each equiprobable bin in the R-S2 space from the bin expectation value of the Poisson-likelihood. The computed GOF p-value obtained is $p = 0.085$.

of radioactive decays of possible impurities present on the TPC surfaces for the energy spectrum, and a full event detection chain simulation that correctly describes all the effects that might influence the signal production and detection, including electric field effects, charge loss, electron pile-up and photon reflection. At the moment these simulations work reasonably well for the inner parts of the detector, describing ER and NR events, but they do not capture fully the observations at the edges of the detector and studies are ongoing in this regard.

6. Conclusions and Outlook

This chapter provides the conclusions of the dissertation and the a final picture of future work using EFT in dark matter searches and improving the statistical inference and the background modelling for dual-phase TPC experiments.

6.1 Conclusions

The ChEFT framework can provide important information about how dark matter interacts within direct detection experiments. While dark matter remains elusive to direct detection, by constraining the coupling constants of fundamental interactions in a ChEFT framework, we can still obtain useful information about theoretical models that describe the possible channels of dark matter detection, as well as constraining the physics scale at which dark matter interacts with normal matter.

This dissertation has shown that ChEFT can be used to analyse nuclear recoil data, providing a ChEFT analysis of XENON1T data in an increased energy window. The data, while compatible with the background only hypothesis, provided constraints on the individual Wilson coefficients of 25 channels of interaction, and on the corresponding scale. The analysis has also shown that the effect of isospin breaking interactions could significantly affect the direct detection constraints, showing that isospin breaking for the Vector$\otimes$Vector channel, the leading term for Dirac fermion dark matter interactions, leads to limits worsening by more than 3 orders of magnitude with respect to the isospin conserving case. Another interesting result is that the same cancellation does not happen in the Axial-vector$\otimes$Vector channel, the leading term for Majorana fermion dark matter, when one correctly considers the interplay between Wilson coefficients from above weak scale contributions.

The dissertation shows also how EFT can provide information also about dark matter-electron interactions, and using single or few electron emission signals in the XENON1T detector we were able to constrain the magnetic and dipole, and the anapole couplings for light dark matter.

Lastly, the dissertation describes the FLAMEDISX framework, an inference framework based on the explicit calculation of a multidimensional likelihood, and presents an example of modelling the surface background of xenon dual-phase TPCs using FLAMEDISX. We propose an effective signal emission model for this background which shows good agreement with the calibration data from the XENONnT experiment and displays the potential of including such a background in the likelihood for future searches using the FLAMEDISX framework.

6.2 Outlook

The EFT analyses of this work rely on data from the XENON1T detector, but the next iteration of dual-phase TPC experiments are already operating and taking data, expecting to release the first results in the imminent future. In the hopeful case of dark matter detection, ChEFT could provide important information about the particle interaction in the detector, further restricting theoretical models.

At the same time, improvements in the statistical inference methods could accelerate possible dark matter discoveries, as shown in [PAPER III], however such method needs special treatment for uncommon backgrounds as the events originating from the TPC surfaces. The addition of such backgrounds, correctly modelled, could increase the effective volume of target mass in the detector. Furthermore the work described in the dissertation could serve as a stepping stone towards a more accurate physical description of such backgrounds. Currently multiple avenues are being explored to enhance the discovery power in dark matter searches, and more precise background modelling and estimation is just one of them.

Sammanfattning

Kosmologiska och astronomiska observationer visar att det mesta av materian i universum är mörk materia. Denna avhandling ger en översikt över bevisen för mörk materia och fokuserar på hypotesen om mörk materia som partiklar med fokus på Weakly Interactive Massive Particles (WIMPs). Den beskriver de viktigaste WIMP-detektionsstrategierna och tar upp ämnet WIMP-spridning i direktdetekteringsexperiment.

Detta arbete analyserar data från XENON1T-experimentet och undersöker kärnrekylerna från möjliga WIMP-interaktioner inom ramen för Chiral Effective Field Theory (ChEFT). Den presenterar XENON1T-detektorn, de viktigaste bakgrunderna, xenonsignalemissionsmodellen och bakgrundsstudierna, och beskriver den statistiska inferensen som används i analysen.

XENON1T-detektorn var en tvåfasig Time Projection Chamber (TPC) som använde ett 2t flytande xenonmål för att detektera spridande partiklar. WIMPs med massor över $\sim 10\,\mathrm{GeV/c^2}$ spridning mot xenonkärnorna skulle deponera tillräckligt med energi för att skapa en synlig händelse.

ChEFT-analysen utförs på XENON1T-data från 278,8 dagars datatagning för en total exponering på 1 ton×year, med en kombinerad likelihood-funktion för detektorns två datatagningsperioder. Området av intresse för denna analys utökades från $[4.9, 40.9]\,\mathrm{keV}_{nr}$, i Spin Independent-analysen, till $[4.9, 54.4]\,\mathrm{keV}_{nr}$, för att öka acceptansen för möjliga modeller med spektrum som toppar vid högre energier ($> 0\,\mathrm{keV}_{nr}$). Analysen visar att data överensstämmer med bakgrundshypotesen och ger gränser för interaktionskoefficienterna och skalan för 25 olika operatorer. Analysen kompletteras med gränser för tre benchmarkmodeller för interaktion inom ChEFT-ramverket. För dessa modeller undersöker vi effekten av isospinbrytande interaktioner, och rapporterar annulleringsregioner där gränsen förvärras upp till 6 storleksordningar med avseende på det isospinbevarande fallet.

Avhandlingen kompletteras med mörk materia-elektronspridningsstudien inom ett EFT-ramverk, som analyserar enstaka eller få elektronemissionssignaler i XENON1T. Analysen ger de första experimentella gränserna för mörk materia-elektron effektiva operatorer för den magnetiska och elektriska dipolen och anapolinteraktioner.

Slutligen beskriver avhandlingen ett exempel på att introducera en datadriven bakgrundsmodell i ett inferensramverk baserat på en explicit multidimensionell likelihood-funktion. Bakgrundsmodelleringen görs med hjälp av kalibreringsdata från XENONnT-detektorn, nästa iteration av en tvåfas xenon-TPC i XENON-detektorfamiljen, som för närvarande är i drift.

Rezumat

Observațiile cosmologice și astronomice arată că cea mai mare parte a materiei din Univers este materie întunecată. Această disertație oferă o privire de ansamblu asupra dovezilor materiei întunecate concentrându-se pe ipoteza particulelor de materie întunecată, descriind posibili candidați, și pe conceptul particulelor masive slab interactive (Weakly Interactive Massive Particles - WIMP). Studiul descrie principalele strategii de detectare de WIMP și abordează subiectul reculului provocat de WIMP în experimentele de tip detectare directă.

Această lucrare analizează datele din experimentul XENON1T, investigând într-un cadru de Chiral Effective Field Theory (ChEFT) reculul nuclear din posibilele interacții de WIMP. Prin acest intermediu sunt puse în evidentă detectorul XENON1T, fundalurile principale, modelul de emisie a semnalului în xenon și studiile fundalelor, și descrie inferența statistică adoptată în analiză.

Detectorul XENON1T a fost constituit dintr-un Time Projection Chamber (TPC) cu două faze cu o țintă de xenon lichid de circa 2 tone pentru a detecta particulele care interacționează în ea. WIMP-urile cu mase peste $\sim 10\,\mathrm{GeV/c^2}$ care se ciocnesc de nucleele de xenon ar depune suficientă energie pentru a crea un eveniment observabil.

Analiza de ChEFT este efectuată pe datele din experimentul XENON1T în unrmă a 278,8 zile de funcționare pentru o expunere totală de 1 tonă×an, cu o funcție de verosimilitate combinată a două etape de preluare a datelor ale detectorului. Regiunea de interes pentru această analiză a fost extinsă de la $[4.9, 40.9]\,\mathrm{keV}_{nr}$, în analiza Spin Independent, la $[4.9, 54.4]\,\mathrm{keV}_{nr}$, pentru a crește acceptarea posibilelor modele cu rate maxime de interacțiune la energii diferite de zero ($> 0\,\mathrm{keV}_{nr}$). Experimentul evidențiază că datele sunt în concordanță doar cu o ipoteză de fundal și oferă limite asupra coeficienților de interacțiune și scara fizică pentru 25 de operatori diferiți. Cercetarea este completată de limite pentru trei modele de referință de interacțiune folosind ChEFT. Pentru aceste modele investigăm efectul interacțiilor de rupere a isospinului, raportând regiunile de anulare în care limitele se înrăutățesc cu până la 6 ordine de mărime față de cazul de conservare a isospinului.

Teza este completată cu studiul de interacție a materiei întunecate cu electronii într-un cadru EFT, analizând semnalele de emisie de unici sau puțini electroni în XENON1T. Astfel sunt expuse primele limite experimentale ale operatori-

lor care descriu interacțiunile de materie întunecată-electron prin intermediul dipolilor magnetic și electric, și anapolului.

În cele din urmă, disertația descrie un exemplu de introducere a unui model de fundal data-driven, într-un cadru de inferență bazat pe calculul explicit a funcției de verosimilitate multidimensionale. Modelarea de fundal s-a facut folosind datele de calibrare ale detectorului XENONnT, următoarea iterație a unui TPC cu dublă fază de xenon din familia de detectoare XENON, care este în prezent în funcțiune.

Acknowledgements

First and foremost, I would like to acknowledge and thank J. Menéndez, M. Hoferichter, F. Bishara, J. Brod and J. Zupan for the discussions that lead to the ChEFT work discussed in the dissertation, for guidance in using the tools they made available, and Timon Emken for providing the software tools and assistance for the computation of the DM-electron interaction responses.
I would like now to thank and acknowledge everyone who in one way or another has helped me complete this work. I would start with my supervisors Jan Conrad and Alfredo Ferella, who guided me and taught me a lot about statistics, detectors and physics in general. I would like to thank the colleagues in the Stockholm group, Pueh Leng Tan, Jörn Mahlstedt, Andrea Gallo Rosso, Ashley Joy, for making work a bit more fun, and former colleagues, Jelle Aalbers, Boris Bauermeister, Bart Pelssers, Knut Morå, Andrea Chiappo and Ben Farmer who made it easy for me to settle in Stockholm. In particular, thanks to Jörn and Alfredo for introducing me to climbing and the lab work with SUXeSs, Boris for discussing music and enjoying the good musical scene of Stockholm, Pueh, Jelle and Bart for sharing the pains and frustration of software development, Knut for the guidance in everything stats related.
I would like to thank the XENON Collaboration for the opportunity to work with such an amazing group of people, for the nice discussions, workshops, shifts and meetings combining work with pleasant dinners and activities.
I would like to thank the friends I made along the way, Mika, Douglas, Alin, Roger and Arturo: you helped me keep sane! I would also like to thank my family and friends in Italy (and all over Europe) for the support, and a special thanks goes to my parents who always tried their best to understand and support me.
Lastly I want to thank my partner, Yiqi, for standing besides me through these times: truly, thank you!

References

[1] F. Zwicky. “Die Rotverschiebung von extragalaktischen Nebeln”. In: *Helvetica Physica Acta* 6 (Jan. 1933), pp. 110–127.

[2] Planck Collaboration, N Aghanim, et al. *Planck 2018 results. VI. Cosmological parameters*. 2018. arXiv: `1807.06209 [astro-ph.CO]`.

[3] Douglas Clowe et al. “A direct empirical proof of the existence of dark matter”. In: *The Astrophysical Journal Letters* 648.2 (2006), p. L109.

[4] D Paraficz et al. “The Bullet cluster at its best: weighing stars, gas, and dark matter”. In: *Astronomy & Astrophysics* 594 (2016), A121.

[5] Edvige Corbelli and Paolo Salucci. “The extended rotation curve and the dark matter halo of M33”. In: *Monthly Notices of the Royal Astronomical Society* 311.2 (Jan. 2000), pp. 441–447. ISSN: 0035-8711. DOI: `10.1046/j.1365-8711.2000.03075.x`.

[6] JR Brownstein and JW Moffat. “Galaxy rotation curves without nonbaryonic dark matter”. In: *The Astrophysical Journal* 636.2 (2006), p. 721.

[7] JR Brownstein and JW Moffat. “The Bullet Cluster 1E0657-558 evidence shows modified gravity in the absence of dark matter”. In: *Monthly Notices of the Royal Astronomical Society* 382.1 (2007), pp. 29–47.

[8] Edward L Wright. “Theoretical overview of cosmic microwave background anisotropy”. In: *arXiv preprint astro-ph/0305591* (2003).

[9] Volker Springel et al. “Simulations of the formation, evolution and clustering of galaxies and quasars”. In: *nature* 435.7042 (2005), pp. 629–636.

[10] Antonino Del Popolo. “Dark matter, density perturbations, and structure formation”. In: *Astronomy Reports* 51.3 (2007), pp. 169–196.

[11] Anne M Green. “Astrophysical uncertainties on the local dark matter distribution and direct detection experiments”. In: *Journal of Physics G: Nuclear and Particle Physics* 44.8 (2017), p. 084001.

[12] Bart Eduard Jan Pelssers. “Enhancing Direct Searches for Dark Matter: Spatial-Temporal Modeling and Explicit Likelihoods”. PhD thesis. Department of Physics, Stockholm University, 2020.

[13] Yao-Yuan Mao et al. “Halo-to-halo similarity and scatter in the velocity distribution of dark matter”. In: *The Astrophysical Journal* 764.1 (2013), p. 35.

[14] Mordehai Milgrom. “A modification of the Newtonian dynamics-Implications for galaxies”. In: *The Astrophysical Journal* 270 (1983), pp. 371–389.

[15] Carlos S Frenk and Simon DM White. “Dark matter and cosmic structure”. In: *Annalen der Physik* 524.9-10 (2012), pp. 507–534.

[16] Anatoly Klypin et al. “Structure formation with cold plus hot dark matter”. In: *Astrophys. J.* 416 (1993), pp. 1–16. DOI: `10.1086/173210`. arXiv: `astro-ph/9305011`.

[17] Gianfranco Bertone, Dan Hooper, and Joseph Silk. “Particle dark matter: evidence, candidates and constraints”. In: *Physics Reports* 405.5-6 (2005), 279–390. ISSN: 0370-1573. DOI: `10.1016/j.physrep.2004.08.031`. URL: `http://dx.doi.org/10.1016/j.physrep.2004.08.031`.

[18] Mikko Laine and Mikhail Shaposhnikov. “Sterile neutrino dark matter as a consequence of νMSM-induced lepton asymmetry”. In: *Journal of Cosmology and Astroparticle Physics* 2008.06 (2008), p. 031.

[19] A Dolgov. “Massive sterile neutrinos as warm dark matter”. In: *Astroparticle Physics* 16.3 (2002), 339–344. ISSN: 0927-6505. DOI: `10.1016/s0927-6505(01)00115-3`. URL: `http://dx.doi.org/10.1016/S0927-6505(01)00115-3`.

[20] Roberto D Peccei and Helen R Quinn. “CP conservation in the presence of pseudoparticles”. In: *Physical Review Letters* 38.25 (1977), p. 1440.

[21] G’t Hooft. “Symmetry breaking through Bell-Jackiw anomalies”. In: *Instantons In Gauge Theories*. World Scientific, 1994, pp. 226–229.

[22] Wayne Hu, Rennan Barkana, and Andrei Gruzinov. “Fuzzy cold dark matter: the wave properties of ultralight particles”. In: *Physical Review Letters* 85.6 (2000), p. 1158.

[23] Jonathan L Feng. “Dark matter candidates from particle physics and methods of detection”. In: *Annual Review of Astronomy and Astrophysics* 48 (2010), pp. 495–545.

[24] Jonathan L Feng, Konstantin T Matchev, and Frank Wilczek. "Neutralino dark matter in focus point supersymmetry". In: *Physics Letters B* 482.4 (2000), pp. 388–399.

[25] Chris Gordon and Oscar Macias. "Dark matter and pulsar model constraints from Galactic Center Fermi-LAT gamma-ray observations". In: *Physical Review D* 88.8 (2013), p. 083521.

[26] F Aharonian et al. "Observations of the Sagittarius Dwarf galaxy by the HESS experiment and search for a Dark Matter signal". In: *Astroparticle Physics* 29.1 (2008), pp. 55–62.

[27] M Doro et al. "Dark matter and fundamental physics with the Cherenkov Telescope Array". In: *Astroparticle Physics* 43 (2013), pp. 189–214.

[28] Julien Lavalle et al. "Antimatter cosmic rays from dark matter annihilation: First results from an N-body experiment". In: *Physical Review D* 78.10 (2008), p. 103526.

[29] O Adriani et al. "Cosmic-ray positron energy spectrum measured by PAMELA". In: *Physical review letters* 111.8 (2013), p. 081102.

[30] M Aguilar et al. "First result from the Alpha Magnetic Spectrometer on the International Space Station: precision measurement of the positron fraction in primary cosmic rays of 0.5–350 GeV". In: *Physical Review Letters* 110.14 (2013), p. 141102.

[31] Mathieu Boudaud et al. "A new look at the cosmic ray positron fraction". In: *Astronomy & Astrophysics* 575 (2015), A67.

[32] Silvia Adrián-Martínez et al. "Limits on dark matter annihilation in the sun using the ANTARES neutrino telescope". In: *Physics Letters B* 759 (2016), pp. 69–74.

[33] MG Aartsen et al. "Search for dark matter annihilation in the Galactic Center with IceCube-79". In: *The European Physical Journal C* 75.10 (2015), p. 492.

[34] MG Aartsen et al. "Search for annihilating dark matter in the Sun with 3 years of IceCube data". In: *The European Physical Journal C* 77.3 (2017), p. 146.

[35] Gianfranco Bertone. *Particle dark matter: observations, models and searches*. Cambridge University Press, 2010.

[36] Christopher McCabe. "The Earth's velocity for direct detection experiments". In: *Journal of Cosmology and Astroparticle Physics* 2014.02 (2014), p. 027.

[37] Jonathan Engel, Stuart Pittel, and Petr Vogel. “Nuclear physics of dark matter detection”. In: *International Journal of Modern Physics E* 1.01 (1992), pp. 1–37.

[38] L Vietze et al. “Nuclear structure aspects of spin-independent WIMP scattering off xenon”. In: *Physical Review D* 91.4 (2015), p. 043520.

[39] Spencer Chang, Aaron Pierce, and Neal Weiner. “Momentum dependent dark matter scattering”. In: *Journal of Cosmology and Astroparticle Physics* 2010.01 (2010), p. 006.

[40] Nikhil Anand, A Liam Fitzpatrick, and WC Haxton. “Weakly interacting massive particle-nucleus elastic scattering response”. In: *Physical Review C* 89.6 (2014), p. 065501.

[41] Elena Aprile et al. “Effective field theory search for high-energy nuclear recoils using the XENON100 dark matter detector”. In: *Physical Review D* 96.4 (2017), p. 042004.

[42] DS Akerib et al. “An Effective Field Theory Analysis of the First LUX Dark Matter Search”. In: (2020). arXiv: `2003.11141`.

[43] JiJi Fan, Matthew Reece, and Lian-Tao Wang. “Non-relativistic effective theory of dark matter direct detection”. In: *Journal of Cosmology and Astroparticle Physics* 2010.11 (2010), p. 042.

[44] Martin Hoferichter, Philipp Klos, and Achim Schwenk. “Chiral power counting of one-and two-body currents in direct detection of dark matter”. In: *Physics Letters B* 746 (2015), pp. 410–416.

[45] Martin Hoferichter et al. “Nuclear structure factors for general spin-independent WIMP-nucleus scattering”. In: *Physical Review D* 99.5 (2019), p. 055031.

[46] Fady Bishara et al. “From quarks to nucleons in dark matter direct detection”. In: *Journal of High Energy Physics* 2017.11 (2017), pp. 1–41.

[47] Fady Bishara et al. “Chiral effective theory of dark matter direct detection”. In: *Journal of Cosmology and Astroparticle Physics* 2017.02 (2017), p. 009.

[48] XENON Collaboration et al. “First results on the scalar WIMP-pion coupling, using the XENON1T experiment”. In: *Physical Review Letters* 122.7 (2019), p. 071301.

[49] Vernon Barger, Wai-Yee Keung, and Danny Marfatia. “Electromagnetic properties of dark matter: Dipole moments and charge form factor”. In: *Physics Letters B* 696.1-2 (2011), pp. 74–78.

[50] A Liam Fitzpatrick et al. “The effective field theory of dark matter direct detection”. In: *Journal of Cosmology and Astroparticle Physics* 2013.02 (2013), p. 004.

[51] Philipp Klos. “Few-neutron systems and WIMP-nucleus interactions from chiral effective field theory”. PhD thesis. Technische Universität, 2018.

[52] Fady Bishara et al. “DirectDM: a tool for dark matter direct detection”. In: *arXiv preprint arXiv:1708.02678* (2017).

[53] XENON Collaboration et al. “Dark matter search results from a one ton-year exposure of xenon1t”. In: *Physical review letters* 121.11 (2018), p. 111302.

[54] Elena Aprile et al. “The XENON1T dark matter experiment”. In: *The European Physical Journal C* 77.12 (2017), pp. 1–23.

[55] Konrad Kleinknecht. *Detectors for particle radiation*. Cambridge University Press, 1998.

[56] M Szydagis et al. “NEST: a comprehensive model for scintillation yield in liquid xenon”. In: *Journal of Instrumentation* 6.10 (2011), P10002.

[57] Brian Lenardo et al. “A global analysis of light and charge yields in liquid xenon”. In: *IEEE Transactions on Nuclear Science* 62.6 (2015), pp. 3387–3396.

[58] D-M Mei et al. “A model of nuclear recoil scintillation efficiency in noble liquids”. In: *Astroparticle Physics* 30.1 (2008), pp. 12–17.

[59] Peter Sorensen and Carl Eric Dahl. “Nuclear recoil energy scale in liquid xenon with application to the direct detection of dark matter”. In: *Physical Review D* 83.6 (2011), p. 063501.

[60] XENON Collaboration et al. “XENON1T dark matter data analysis: Signal and background models and statistical inference”. In: *Physical Review D* 99.11 (2019), p. 112009.

[61] J Thomas and DA Imel. “Recombination of electron-ion pairs in liquid argon and liquid xenon”. In: *Physical Review A* 36.2 (1987), p. 614.

[62] DS Akerib et al. “Tritium calibration of the LUX dark matter experiment”. In: *Physical Review D* 93.7 (2016), p. 072009.

[63] E Aprile et al. “The XENON1T data acquisition system”. In: *Journal of Instrumentation* 14.07 (2019), P07016.

[64] XENON Collaboration. “The pax data processor v6.8.0”. In: *Zenodo* (Version 6.8.0). DOI: `http://doi.org/10.5281/zenodo.1195785`.

[65] Bart Eduard Jan Pelssers. “Position reconstruction and data quality in xenon”. MA thesis. Utrecht University, 2015.

[66] E Aprile et al. “Observation of Excess Electronic Recoil Events in XENON1T”. In: (2020). eprint: `arXiv:2006.09721`.

[67] E Aprile et al. “Physics reach of the XENON1T dark matter experiment.” In: *Journal of Cosmology and Astroparticle Physics* 2016.04 (2016), p. 027.

[68] XENON Collaboration et al. “Constraining the spin-dependent WIMP-nucleon cross sections with XENON1T”. In: *Physical Review Letters* 122.14 (2019), p. 141301.

[69] Knut Dundas Morå. “Statistical Modelling and Inference for XENON1T”. PhD thesis. Department of Physics, Stockholm University, 2019.

[70] Nadav Priel et al. “A model independent safeguard against background mismodeling for statistical inference”. In: *Journal of Cosmology and Astroparticle Physics* 2017.05 (2017), p. 013.

[71] Elena Aprile et al. “First dark matter search results from the XENON1T experiment”. In: *Physical review letters* 119.18 (2017), p. 181301.

[72] Samuel S Wilks. “The large-sample distribution of the likelihood ratio for testing composite hypotheses”. In: *The annals of mathematical statistics* 9.1 (1938), pp. 60–62.

[73] Sara Algeri et al. “Searching for new physics with profile likelihoods: Wilks and beyond”. In: *arXiv preprint arXiv:1911.10237* (2019).

[74] Glen Cowan et al. “Power-constrained limits”. In: (2011). arXiv: `arXiv:1105.3166`.

[75] Gary J Feldman and Robert D Cousins. “Unified approach to the classical statistical analysis of small signals”. In: *Physical Review D* 57.7 (1998), p. 3873.

[76] Elena Aprile et al. “Excess electronic recoil events in XENON1T”. In: *Physical Review D* 102.7 (2020), p. 072004.

[77] Nikhil Anand, A Liam Fitzpatrick, and WC Haxton. “Model-independent WIMP scattering responses and event rates: A Mathematica package for experimental analysis”. In: *arXiv preprint arXiv:1308.6288* (2013).

[78] Fady Bishara et al. “Renormalization group effects in dark matter interactions”. In: *Journal of High Energy Physics* 2020.3 (2020), pp. 1–61.

[79] Marco Battaglieri et al. “US cosmic visions: new ideas in dark matter 2017: community report”. In: *arXiv preprint arXiv:1707.04591* (2017).

[80] Rouven Essig, Jeremy Mardon, and Tomer Volansky. “Direct detection of sub-GeV dark matter”. In: *Physical Review D* 85.7 (2012), p. 076007.

[81] Riccardo Catena et al. “Atomic responses to general dark matter-electron interactions”. In: *Physical Review Research* 2.3 (2020), p. 033195.

[82] Joachim Kopp et al. “DAMA/LIBRA data and leptonically interacting dark matter”. In: *Physical Review D* 80.8 (2009), p. 083502.

[83] Rouven Essig et al. “Direct detection of sub-GeV dark matter with semiconductor targets”. In: *Journal of High Energy Physics* 2016.5 (2016), pp. 1–54.

[84] Rouven Essig et al. “First direct detection limits on sub-GeV dark matter from XENON10”. In: *Physical review letters* 109.2 (2012), p. 021301.

[85] Peter W Graham et al. “Semiconductor probes of light dark matter”. In: *Physics of the Dark Universe* 1.1-2 (2012), pp. 32–49.

[86] Jae Hyeok Chang, Rouven Essig, and Annika Reinert. “Light (ly)-coupled dark matter in the keV range: freeze-in and constraints”. In: *arXiv preprint arXiv:1911.03389* (2019).

[87] Steven Yellin. “Finding an upper limit in the presence of an unknown background”. In: *Physical Review D* 66.3 (2002), p. 032005.

[88] J Angle et al. “Search for light dark matter in XENON10 data”. In: *Physical Review Letters* 107.5 (2011), p. 051301.

[89] Elena Aprile et al. “Light dark matter search with ionization signals in XENON1T”. In: *Physical Review Letters* 123.25 (2019), p. 251801.

[90] P Agnes et al. “Constraints on sub-GeV dark-matter–electron scattering from the DarkSide-50 experiment”. In: *Physical review letters* 121.11 (2018), p. 111303.

[91] Jelle Aalbers et al. *FlamTeam/flamedisx: v1.5.0*. Version v1.5.0. June 2021. DOI: `10.5281/zenodo.5042263`. URL: `https://doi.org/10.5281/zenodo.5042263`.

[92] Martín Abadi et al. *TensorFlow: Large-Scale Machine Learning on Heterogeneous Systems*. Software available from tensorflow.org. 2015. URL: `https://www.tensorflow.org/`.

[93] DS Akerib et al. “Signal yields, energy resolution, and recombination fluctuations in liquid xenon”. In: *Physical Review D* 95.1 (2017), p. 012008.

[94] V. C. Antochi et al. "Improved quality tests of R11410-21 photomultiplier tubes for the XENONnT experiment". In: *JINST* 16.08 (2021), P08033. DOI: `10.1088/1748-0221/16/08/P08033`. arXiv: `2104.15051 [physics.ins-det]`.

[95] Guido Van Rossum and Fred L. Drake. *Python 3 Reference Manual*. Scotts Valley, CA: CreateSpace, 2009. ISBN: 1441412697.

[96] E Aprile et al. "Projected WIMP Sensitivity of the XENONnT Dark Matter Experiment". In: (2020). eprint: `arXiv:2007.08796`.

[97] Panayiotis Theodossiou. "Financial data and the skewed generalized t distribution". In: *Management Science* 44.12-part-1 (1998), pp. 1650–1661.

[98] Diethelm Wurtz, Yohan Chalabi, and Ladislav Luksan. "Parameter estimation of ARMA models with GARCH/APARCH errors an R and SPlus software implementation". In: *Journal of Statistical Software* 55.2 (2006), pp. 28–33.

[99] Stephan R Sain. "Adaptive kernel density estimation". PhD thesis. Rice University, 1994.

[100] Steve Baker and Robert D Cousins. "Clarification of the use of chi-square and likelihood functions in fits to histograms". In: *Nuclear Instruments and Methods in Physics Research* 221.2 (1984), pp. 437–442.

[101] Robert Hammann et al. *XENONnT/GOFevaluation: v0.1.0-zenodo-init*. Version v0.1.0-zenodo-init. Oct. 2021. DOI: `10.5281/zenodo.5626909`. URL: `https://doi.org/10.5281/zenodo.5626909`.